Opterećenje vjetrom na visokim zgradama s poroznim dvostrukim pročeljima

Melnjak, Petar

Master's thesis / Diplomski rad

2022

Degree Grantor / Ustanova koja je dodijelila akademski / stručni stupanj: **University of Zagreb, Faculty of Mechanical Engineering and Naval Architecture / Sveučilište u Zagrebu, Fakultet strojarstva i brodogradnje**

Permanent link / Trajna poveznica: https://urn.nsk.hr/urn:nbn:hr:235:126568

UNIVERSITY OF ZAGREB
FACULTY OF MECHANICAL ENGINEERING AND NAVAL ARCHITECTURE

MASTER THESIS

Petar Melnjak

Zagreb, 2022.

UNIVERSITY OF ZAGREB
FACULTY OF MECHANICAL ENGINEERING AND NAVAL ARCHITECTURE

Wind loads on tall buildings with porous double-skin façades

Mentors:

Prof. Hrvoje Kozmar, PhD
Prof. Gianni Bartoli, PhD

Student:

Petar Melnjak

Zagreb, 2022.

I declare that I have made this thesis on my own using the knowledge acquired during my studies and the cited references.

Petar Melnjak

ACKNOWLEDGMENTS

On this occasion, I would like to sincerely thank Prof. Hrvoje Kozmar and Prof. Gianni Bartoli for the indicated trust, support and mentoring throughout the entire process of research and writing this thesis.

I would also like to express gratitude to all my colleagues from the CRIACIV research centre, especially Claudio Mannini, Tommaso Massai, Michael Macháček and Niccolo Barni, who generously accepted me and passed on their knowledge and skills of working in the wind tunnel.

This research would be much more difficult without a PhD student Petar Škvorc who was always ready to help and share his knowledge with me.

At last but not in least, I would like to thank the Agency for Mobility and EU Programmes, which financially supported my stay abroad.

SVEUČILIŠTE U ZAGREBU
FAKULTET STROJARSTVA I BRODOGRADNJE
Središnje povjerenstvo za završne i diplomske ispite
Povjerenstvo za diplomske ispite studija strojarstva za smjerove:
Procesno-energetski, konstrukcijski, inženjersko modeliranje i računalne simulacije i brodostrojarski

Sveučilište u Zagrebu Fakultet strojarstva i brodogradnje	
Datum	Prilog
Klasa: **602 - 04 / 22 - 6 / 1**	
Ur.broj: **15 - 1703 - 22 -**	

DIPLOMSKI ZADATAK

Student: **Petar Melnjak** JMBAG: 0035211570

Naslov rada na hrvatskom jeziku: **Opterećenje vjetrom na visokim zgradama s poroznim dvostrukim pročeljima**

Naslov rada na engleskom jeziku: **Wind loads on tall buildings with porous double-skin façades**

Opis zadatka:

Wind load is one of the key factors in design of tall buildings because these complex engineering structures are particularly sensitive to wind actions. On the other hand, double-skin façade systems have been increasingly implemented on buildings with the goal of improving building energy efficiency, natural ventilation and visual appearance. At this point, the aerodynamic characteristics of tall buildings equipped with porous double-skin façade systems are still relatively unknown, although it may be expected that the addition of porous outer skins will substantially affect the overall building aerodynamics.

The scope of the present work is to analyze the effect of porous double-skin façades on the tall building aerodynamics. This will be performed experimentally on a small scale in a boundary layer wind tunnel of the Inter-University Research Centre on Building Aerodynamics and Wind Engineering at the University of Florence, Italy. A tall building model with two different sets of porous double-skin façade systems will be studied in the urban environment conditions, i.e. the sheltered (urban) environment will consist of an arrangement of nine buildings models. The effects of spacing density between building models and double-skin façade porosity will be studied. The analysis will encompass aerodynamic forces and moments and surface pressures of the studied building model. The measurements will be carried out using a high-frequency force balance as well as flow velocity and surface pressure transducers.

In this thesis it is necessary to provide:
1) Introduction,
2) Experimental setup,
3) Results and discussion,
4) Conclusions.

It is advised to properly address all references and acknowledge help and support received during this work.

Zadatak zadan:	Datum predaje rada:	Predviđeni datumi obrane:
20. siječnja 2022.	24. ožujka 2022.	28. ožujka 2022. – 1. travnja 2022.

Zadatak zadali:

Prof. dr. sc. Hrvoje Kozmar

Prof. dr. sc. Gianni Bartoli

Predsjednik Povjerenstva:

Prof. dr. sc. Tanja Jurčević Lulić

TABLE OF CONTENTS

TABLE OF FIGURES

LIST OF TABLES

LIST OF SYMBOLS

A	Reference area
a	Width of the building model
C_D	Along-wind force coefficient
C_F	General force coefficient
C_L	Across-wind force coefficient
C_p	Pressure coefficient
$\overline{C_p}$	Mean pressure coefficient
C_{MD}	Along-wind moment coefficient
C_{ML}	Across-wind moment coefficient
c_W	Specific heat of the hot-wire sensor
D	Along-wind force
d	Distance between the building models
d_h	Displacement height
F	Aerodynamic force
F_c	Coriolis force
f	Coriolis parameter
I_u, I_v, I_w	Turbulence intensity in the *x*, *y*, *z*-directions, respectively
I_W	Current intensity
k_w	Eddy wave number
L	Across-wind force
L_u^x	Longitudinal integral length scale of turbulence in the *x*-direction
m	Mass
n	Normal unit vector
p	Pressure
R_u^x	Correlation coefficient
R_W	Resistance of the hot-wire sensor
S_{MD}	Along-wind moment power spectrum

S_{ML}	Across-wind moment power spectrum
$S_u(f)$	Power spectral density of wind velocity fluctuations
T	Acquisition time
T_a	Unheated wire temperature
T_W	Heated wire temperature
t	Time
U_0	Free stream velocity
U_{ref}	Reference velocity
u, v, w	Absolute velocity component in the *x*-, *y*- and *z*- directions, respectively
u', v', w'	Fluctuating velocity components in the *x*-, *y*- and *z*-directions, respectively
$\bar{u}, \bar{v}, \overline{w}$	Mean velocity in the *x*-, *y*-, and *z*-directions, respectively
u_τ	Friction velocity
u_δ	Gradient velocity
z	Vertical distance
z_0	Aerodynamic surface roughness length
z_{ref}	Reference height
z_{tip}	Height of the building model

Greek symbols

α	Power-law exponent
β	Flow incidence angle
δ	Boundary layer thickness
κ	von Kármán constant
λ	Wavelength
μ	Dynamic viscosity
ν	Kinematic viscosity
ω	Angular velocity
ϕ	Latitude angle
ϕ_{conv}	Convective heat flux

ρ_a	Air density
σ	Standard deviation
σ_u	Standard velocity deviation
τ	Turbulent shear stress

Summary

Porous double-skin façade (PDSF) systems have become common in high-performance buildings. A PDSF system consists of an inner impermeable façade and an outer permeable façade. A small gap between the two skins enables the wind flow. The aerodynamic characteristics of buildings equipped with PDSF systems of various porosities were studied in an urban environment. Experiments were conducted in a boundary layer wind tunnel (BLWT) at the Inter-University Research Centre on Building Aerodynamics and Wind Engineering (CRIACIV) at the University of Florence, Italy. Flow characteristics were determined using Pitot tubes and hot-wire anemometry system. Aerodynamic loads and surface pressures acting on the building model were measured using a high-frequency force balance (HFFB) and pressure taps on the inner skin of the building model, respectively. The results indicate that the PDSF system on a building in an urban environment does not affect the across-wind and along-wind moment coefficients, while the PDSF system exhibits a slightly negative effect on the power spectral density of the across-wind moment because the peak values are greater. Furthermore, the PDSF system proved to diminish the mean pressure coefficient peak and mean values on all building surfaces as well as the standard deviation of surface pressure fluctuations.

Sažetak

Primjena sustava poroznog dvostrukog pročelja (PDP) je česta u izgradnji zgrada s visokom energetskom učikovitosti. PDP sustav se sastoji od unutarnjeg nepropusnog pročelja i vanjskog propusnog pročelja. Mali razmak između dvaju pročelja omogućuje vjetru da struji između njih. U sklopu ovog rada su proučavana aerodinamička svojstva zgrada opremljenih PDP sustavima različitih poroznosti, pri čemu su zgrade smještene u urbanom okruženju. Eksperimenti su provedeni u zračnom tunelu za generiranje modela atmosferskog graničnog sloja u istraživačkom centru za aerodinamiku zgrada i inženjerstvo vjetra (CRIACIV) na Sveučilištu u Firenci, Italija. Značajke strujanja su određene korištenjem Pitotovih cijevi i užarene žice. Aerodionamička opterećenja i površinski tlak na modelu zgrade su izmjereni visokofrekventnom vagom i osjetnicima tlaka na unutarnjem nepropusnom pročelju modela zgrade. Pokazano je da PDP sustav na zgradi u urbanom okruženju ne utječe na aerodinamičke koeficijente momenta poprečno i uzduž smjera strujanja, dok s druge strane ima negativan učinak na spektralnu gustoću pulzacija aerodinamičkog momenta u poprečnom smjeru s obzirom na smjer strujanja vjetra, jer su vršne vrijednosti uvećane. PDP sustav uzorkuje smanjenje srednjih i vršnih vrijednosti koeficijenta tlaka na cijeloj površini zgrade kao i standardne devijacije pulzacija površinskog tlaka.

1 Introduction

Contemporary high-performance buildings have been commonly built with a double-skin façade (DSF) system. Such systems consist of an inner impermeable façade and an outer façade that can be either impermeable or permeable. The main motivation for this approach is to increase the energy efficiency of buildings and to protect them from sunlight, rain, snow, and hailstorms.

Computational Fluid Dynamics (CFD) simulations of buildings equipped with a DSF system with impermeable outer skin performed by the Zhu and He [1] showed that the heat transfer coefficient is reduced by 27% in the summer and 24% in the winter. Kosinski *et al*. [2] studied the effect of the DSF system with the impermeable outer skin on the wind washing, i.e., air penetration into thermal insulation of a building. It was concluded that the DSF system reduces the heat loss caused by wind washing.

In this thesis, a DSF system with a permeable (porous) outer façade was studied. In the porous DSF (PDSF) system, the outer façade is usually made of perforated aluminium sheets or stainless steel. Like in the standard DSF with the impermeable outer skin, the porous outer skin of the PDSF system also improves the energy efficiency and shelters the inner façade from atmospheric elements. The main difference between the DSF and PDSF systems is the dominant force that drives the flow between the façades. For the standard DSF systems, the buoyancy force is the force that drives the flow between façades. The temperature difference from the bottom to the top of the building creates the buoyancy force. On the other hand, the dominant force that drives the flow between the façades in the case of the PDSF system is the pressure force caused by the wind flow around the building.

In one of the first studies regarding the PDSF system carried out by Gerhardt and Janser [3], the net pressure coefficients on building models with various façade porosities and aspect ratios subjected to the atmospheric boundary layer (ABL) flow were measured. It was proven that the relevant parameter affecting the pressure coefficient difference was the gap width between the inner and outer façades.

Hu *et al.* [4] measured the pressure coefficient distribution on the windward surface of the CAARC (Commonwealth Advisory Aeronautical Council) building equipped with various

porosities of outer façades. It was concluded that the outer porous screens reduce the surface pressure on the inner façade, but they increase the vortex-shedding frequency. Furthermore, an impermeable DSF system increased the suction on the building's lateral sides, implying that the separation bubble is bigger when using an impermeable façade. On the other hand, a porous outer skin reduces the suction on the lateral surfaces of the building because the separation bubble is shifted downstream.

This thesis aims to investigate the effect of the PDSF system on the aerodynamic characteristics of tall buildings. The experimental investigation was performed in a boundary layer wind tunnel to determine integral wind loading acting on the building model and pressure distributions on its inner façade.

2 Background

Aerodynamics distinguishes several ranges of air velocity. The present thesis was performed at low subsonic speeds at Mach numbers lower than 0.3. In this range of flow velocities, the air is considered incompressible.

2.1 Wind characteristics

Radiation heat transfer from the Sun to the Earth is the major phenomenon that enhances the atmospheric movement of the air. However, the Sun transfers the heat unevenly to various parts of the Earth's surface. This trend causes characteristic heating of various parts of the world, thus leading to global-scale pressure differences. The pressure forces and forces generated by the Earth's rotation are two primary drivers of the horizontal atmospheric airflow -- the wind.

2.1.1 Pressure gradient

The major horizontal driving force acting on the air in the atmosphere is the pressure force. There is a pressure gradient $\partial p/\partial n$ on a fluid particle in the *n* direction with a force per unit mass provided as

$$-\left(\frac{1}{\rho_{\mathrm{a}}}\right)\frac{\partial p}{\partial n}, \tag{2.1}$$

where ρ_{a} is the air density.

The negative sign in equation (2.1) indicates that the pressure force acts from the high-pressure region to the low-pressure region.

2.1.2 Coriolis force

When the Earth is observed from a fixed point in space, the observer can see the rotation of the planet and the total motion of the atmospheric wind. On the other hand, the observer on the Earth's surface can only measure the relative motion of the atmospheric wind due to the rotation with the Earth. Therefore, the ground observer measures the wind with an additional

rotational component. Depending on the hemisphere, it acts to the right or left of the direction of motion. This force is the Coriolis force,

$$F_c = mf\vec{v}, \tag{2.2}$$

where m, v, and f are the mass of the air, velocity, and Coriolis parameter, respectively. Coriolis parameter is defined as

$$f = 2\omega\, sin(\phi), \tag{2.3}$$

where ω is the Earth's angular velocity, and ϕ is the latitude angle.

2.1.3 Thermal stratification

A vertical air motion in the atmosphere is exerted by the buoyancy force due to the thermal stratification of the atmosphere. Thermal stratification of the atmosphere can be neutral, unstable, and stable depending on the zero, upward, and downward effect of the buoyancy force. Figure 2.1, [5] shows the logarithmic velocity profile in the stratified atmosphere.

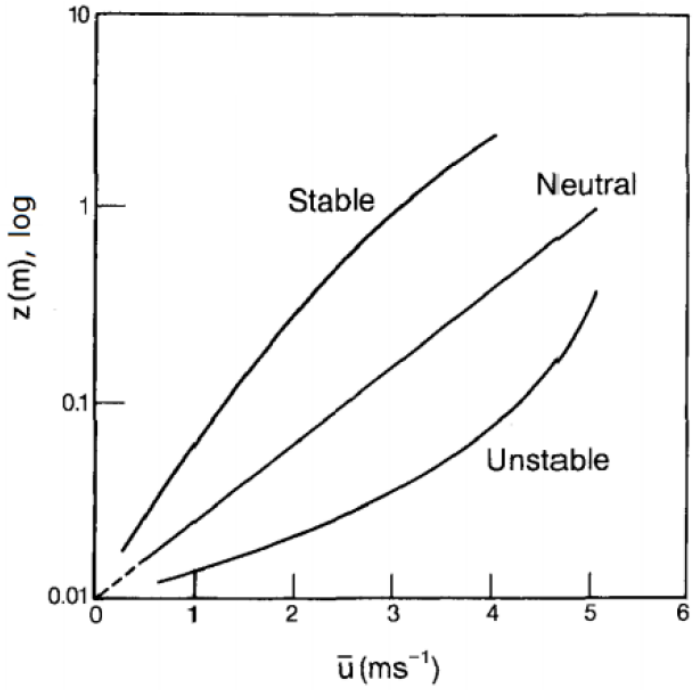

Figure 2.1 Wind velocity profile and the effect of thermal stratification, [5]

2.1.4 Viscous forces

The viscous (friction) force is the force that opposes the wind motion in the lower atmosphere. As approaching the Earth, the viscous forces between the layers of air in the ABL gradually start to play a more significant role. Figure 2.2 shows the equilibrium of forces in the part of the atmosphere where viscous forces cannot be neglected.

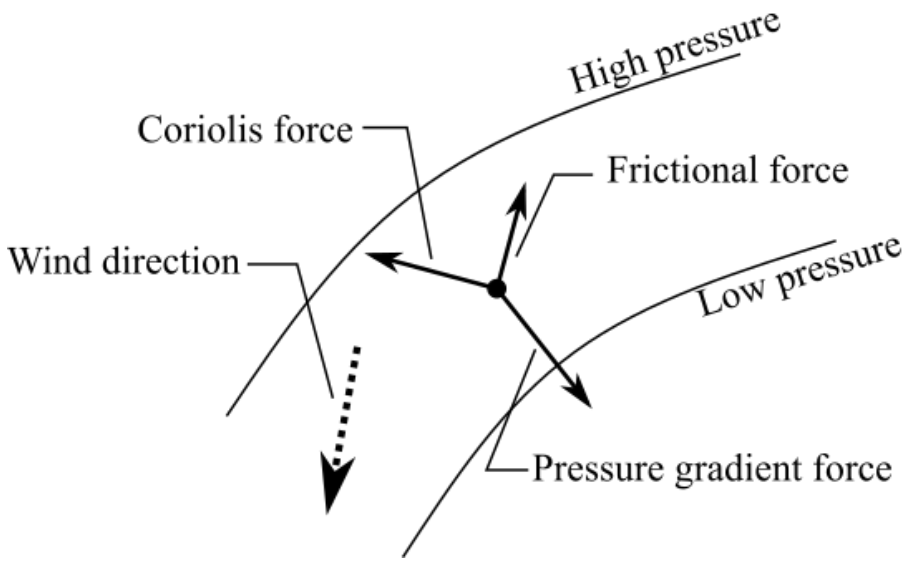

Figure 2.2 Equilibrium of forces in the atmospheric boundary layer

As the surface of the Earth is approached, the wind vector gradually turns towards the low pressure (pressure gradient) due to the rotational Coriolis force, the effect known as the Ekman spiral. The total twist of the ABL is ~30^{o}. However, the twist over the height of the building is usually too low to be considered in most engineering applications.

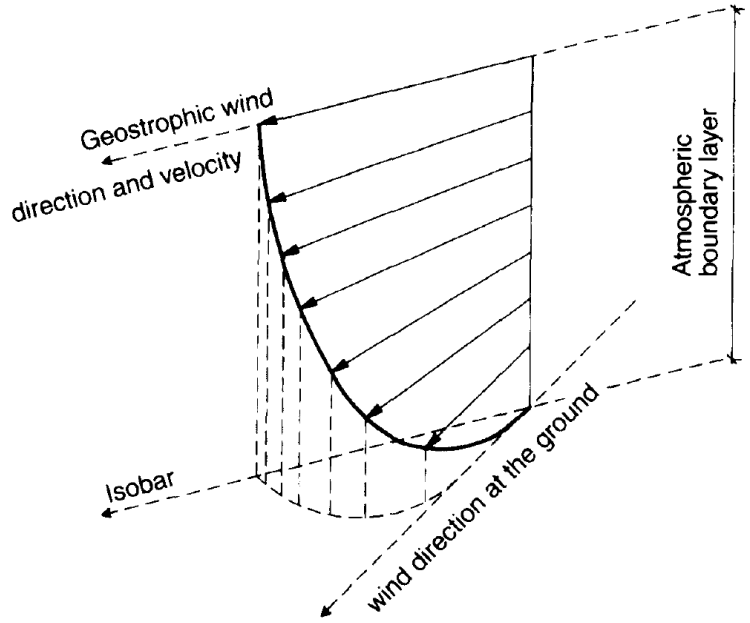

Figure 2.3 Velocity profile in the atmospheric boundary layer considering the Ekman spiral, [6]

2.2 Atmospheric boundary layer

The atmosphere can be divided into smaller layers. However, as part of this thesis, the only layer of the atmosphere further studied is the lowest part of the atmosphere, called the troposphere. More precisely, only the bottom part (about 10%) of the troposphere, i.e., the ABL. The characteristic thickness of the ABL is ~1 km.

In Figure 2.4, the ABL is divided into the outer (Ekman) and inner layers. The outer layer encompasses the most significant part (~90%) of the ABL, and the Coriolis force affects it the most. At the same time, the roughness of the ground surface does not influence the development of the Ekman layer.

The inner layer is characterized by the most significant gradients of physical quantities. It is further classified into inertial (logarithmic) and roughness sublayers. The logarithmic sublayer is characterized by the turbulent stress mechanisms of mass, momentum, and energy transfer. Below the inertial sublayer, there is an interfacial layer where the ground surface roughness dictates the shape of the wind velocity profile.

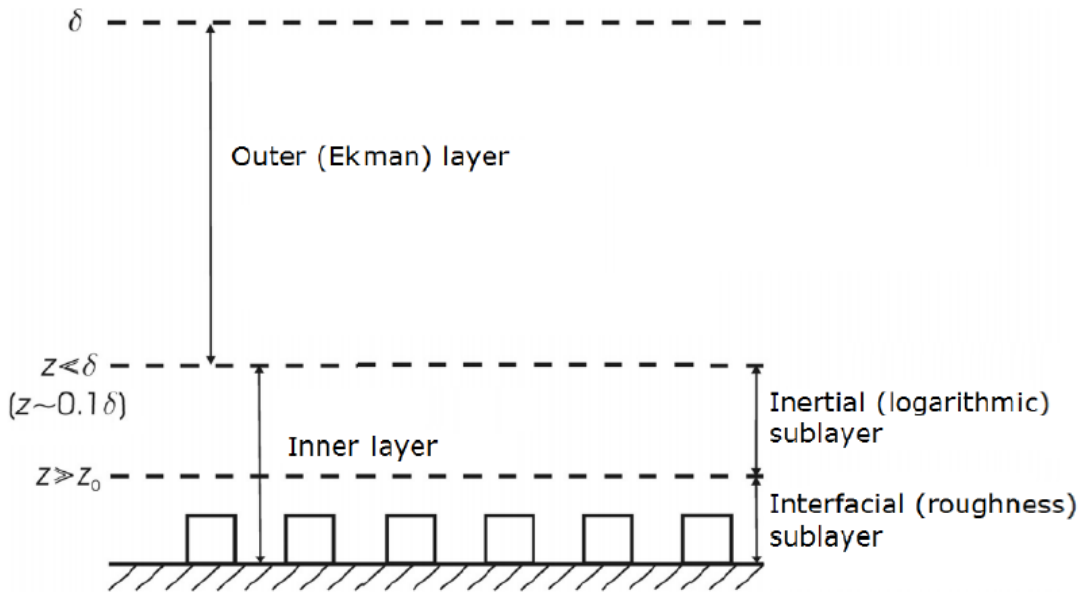

Figure 2.4 Sublayers of the atmospheric boundary layer, [7]

The main characteristics of the fully developed ABL:

- Flow velocity increases with the height increasing from the surface;
- Regardless of the height, the wind retains its turbulent nature;
- Wide range of wind gusting frequencies.

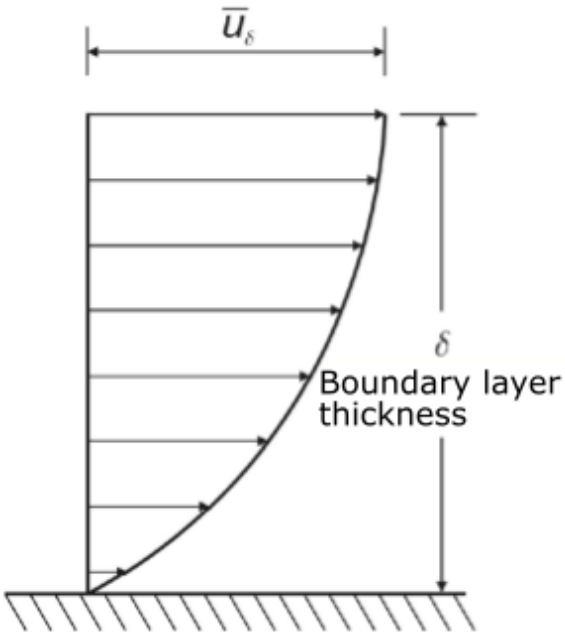

Figure 2.5 Atmospheric boundary layer, [7]

ABL thickness δ is the height where the velocity becomes nearly equal to the free stream velocity outside the ABL. Velocity at height δ is known as the gradient velocity $\overline{u_\delta}$ and δ is the gradient height.

Wind in the ABL is very turbulent. Chaotic motion and random fluctuations of all variables in time and space are generally the main characteristics of the turbulent flow. Turbulent flow occurs at high values of the Reynolds number, which represents the ratio of inertial and viscous forces,

$$Re = \frac{vx}{\nu}. \tag{2.4}$$

Characteristic parameters of atmospheric turbulence are turbulence intensity, integral turbulence length scale, power spectral density of velocity fluctuations, and Reynolds shear stress.

2.2.1.1 Mean wind velocity

Atmospheric turbulence is characterized by exhibited wind velocity fluctuations, Figure 2.6.

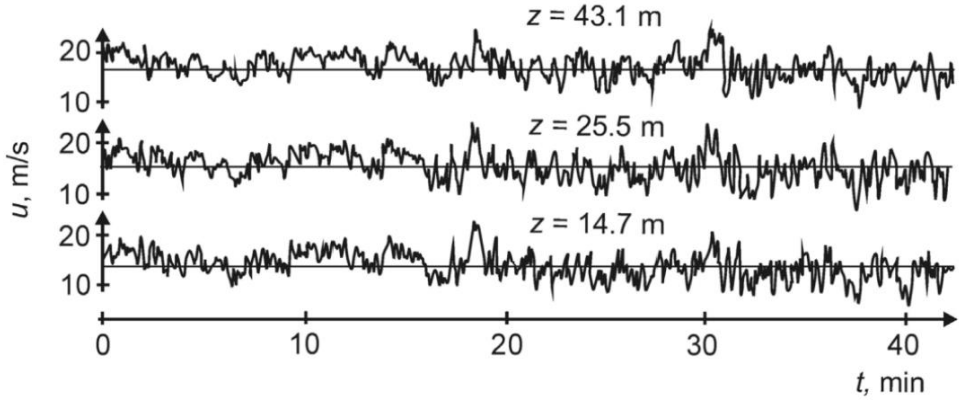

Figure 2.6 Time history of the wind velocity at various heights in the atmospheric boundary layer [6]

In order to describe characteristic wind velocity profiles, all three velocity components are presented as the sum of the mean wind velocity component and the fluctuating wind velocity component,

$$\begin{aligned} u(t) &= \overline{u} + u'(t), \\ v(t) &= \overline{v} + v'(t), \\ w(t) &= \overline{w} + w'(t). \end{aligned} \tag{2.5}$$

This approach is known as Reynolds averaging, and the mean wind velocity is calculated as

$$\overline{u} = \frac{1}{T}\int_{-T/2}^{T/2} u(t)dt. \tag{2.6}$$

Two wind velocity profiles in the ABL are shown in Figure 2.7. The solid line shows the mean wind velocity profile, while the dashed line refers to the turbulent wind velocity component.

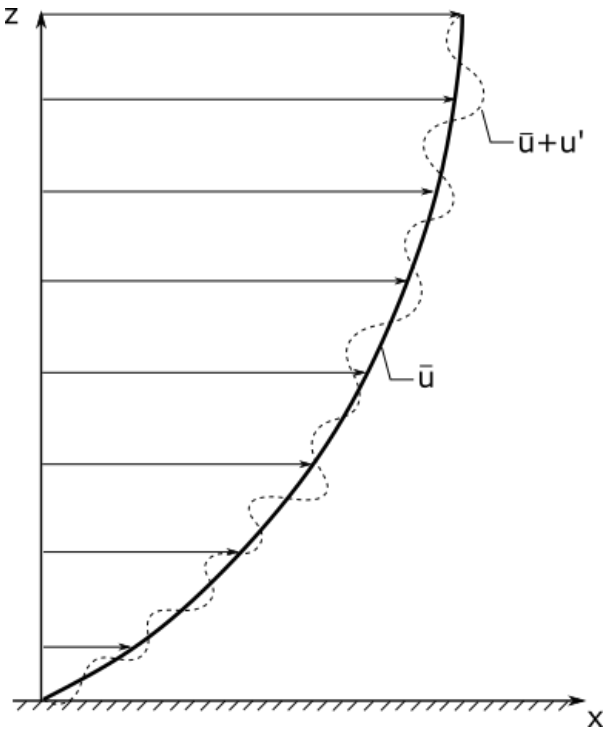

Figure 2.7 Velocity profiles in the atmospheric boundary layer

The ABL flow is three-dimensional, where longitudinal velocity (u) is at least one order of magnitude larger than its lateral (v) and vertical (w) components.

The mean velocity profile in the ABL is commonly described using the power law,

$$\frac{\overline{u_z}}{\overline{u_{\mathrm{ref}}}} = \left(\frac{z - d_h}{z_{\mathrm{ref}} - d_h}\right)^{\alpha} = \left(\frac{\tilde{z}}{\widetilde{z_{\mathrm{ref}}}}\right)^{\alpha}, \tag{2.7}$$

where $\overline{u_z}$ and $\overline{u_{\mathrm{ref}}}$ are the mean velocity and the reference velocity at the reference height z_{ref}. Displacement height d_h is a parameter used to account for the effect of buildings and other engineering structures situated on the ground surface. When displacement height is larger than zero, the velocity profile starts above the height *d*. Since the displacement height can not be determined precisely, it is commonly taken as 75% or 100% of the height of the engineering structures situated on the ground surface. α is the power-law exponent that depends on the aerodynamic surface roughness length z_0, Figure 2.8.

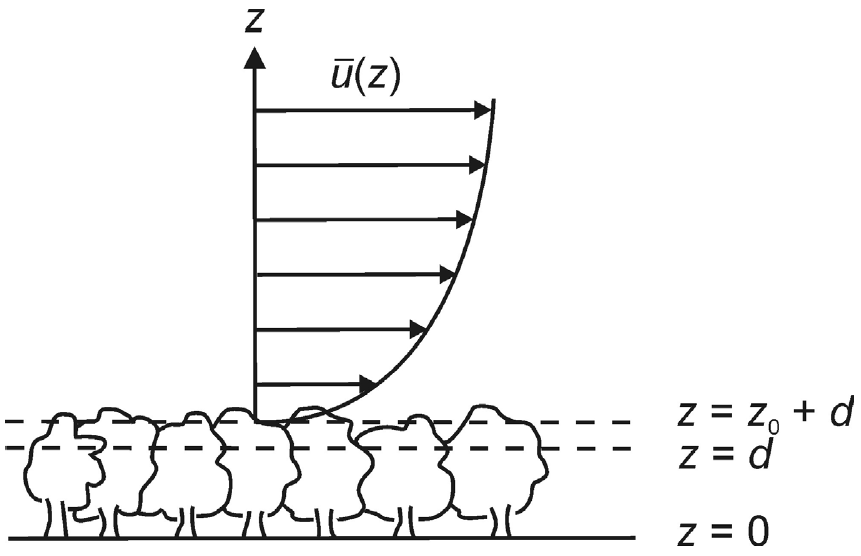

Figure 2.8 The power-law mean velocity profile above dense forest [6]

Table 2.1 provides the aerodynamic surface roughness length for various terrain types.

Table 2.1 Terrain types and aerodynamic surface roughness length [8]

Terrain type	**Aerodynamic surface roughness length, m**
Very flat terrain (snow, desert)	0.001 - 0.005
Open terrain (grassland, few trees)	0.01 - 0.05
Suburban terrain (3 - 5 m high buildings)	0.1 - 0.5
Dense urban (10 - 30 m high buildings)	1 - 5

In the vicinity of the ground surface (up to 100 m), the mean wind velocity profile can also be described using the logarithmic law:

$$\frac{\overline{u_z}}{u_\tau} = \frac{1}{\kappa} \ln \frac{z - d_h}{z_0}, \tag{2.8}$$

where κ is von Kármán constant equal to 0.4, and u_τ is the friction velocity calculated as

$$u_t = \sqrt{\frac{\tau}{\rho}}. \tag{2.9}$$

τ is the shear stress, and ρ is the air density.

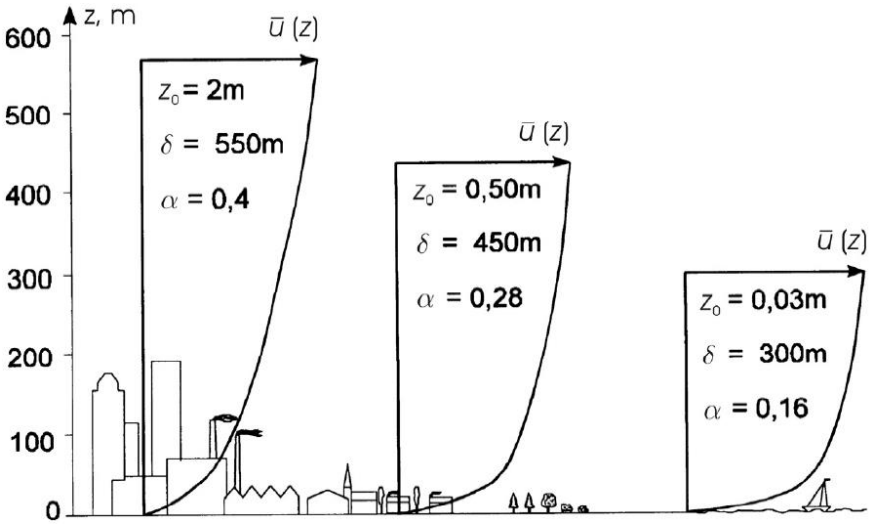

Figure 2.9 Mean wind velocity profiles in the atmospheric boundary layer developing above various types of surface roughness, [9]

2.2.1.2 Turbulence intensity

Turbulence intensity is defined as

$$I_u(z) = \frac{\sqrt{\overline{u'^2}(z)}}{\overline{u_{\text{ref}}}}, \quad I_v(z) = \frac{\sqrt{\overline{v'^2}(z)}}{\overline{u_{\text{ref}}}}, \quad I_w(z) = \frac{\sqrt{\overline{w'^2}(z)}}{\overline{u_{\text{ref}}}}. \tag{2.10}$$

Velocity components with the prime ($u'(z), v'(z), w'(z)$) are fluctuating wind velocity components at the height *z*, while the overbar represents the mean wind velocity components. Various studies have found that turbulence intensity in the longitudinal direction is greater than in the lateral and vertical directions. This ratio is provided in [10],

$$\frac{I_v}{I_u} = 0.75, \quad \frac{I_w}{I_u} = 0.5. \tag{2.11}$$

Turbulence intensity gradually increases as the height above the surface decreases.

2.2.1.3 Integral turbulence length scales

Integral turbulence length scales represent the mean eddy size. Since there are three main directions (*x*, *y*, *z*), in each direction there are three components of velocity (longitudinal, lateral, and vertical). This gives in total nine components of the integral turbulence length scales. The L_u^x integral length scale, which represents the size of the eddies in the *x*-direction caused by the longitudinal velocity pulsations, is predominant,

$$L_u^x = \int_0^\infty R_u^x(\Delta x)\mathrm{d}\,\Delta x, \tag{2.12}$$

where R_u^x is the correlation factor defined as

$$R_u^x(\Delta x) = \frac{\overline{u_1'(t) \cdot u_2'(t)}}{\sqrt{\overline{u_1'^2}} \cdot \sqrt{\overline{u_2'^2}}}. \tag{2.13}$$

When Taylor's frozen turbulence hypothesis is used, the correlation factor can also be written as a function of time, which leads to an integral turbulence length scale in the time domain,

$$L_u^x = \int_0^\infty R_u^x(\Delta t)\mathrm{d}\,\Delta t. \tag{2.14}$$

2.2.1.4 Power spectral density of wind velocity fluctuations

Various sizes of eddies that are causing wind velocity fluctuations characterize the turbulent flow. The power spectral density of wind velocity fluctuations presents velocity fluctuations in the frequency domain. It displays the kinetic energy of turbulent eddies in the flow. Wind velocity fluctuations can be observed in the longitudinal, lateral, and vertical directions. However, in practice, only the longitudinal (along-wind) wind velocity fluctuations in the frequency domain have been commonly studied since they are the major source of wind loads on structures,

$$\sigma_u^2 = \int_0^\infty S_u(f)\mathrm{d}\,f. \tag{2.15}$$

σ_u^2 is the variance of the wind velocity u, $S_u(f)$ is the power spectral density of wind velocity fluctuations in the main wind direction.

The wind flow over a rough surface creates large eddies with low frequencies. These large eddies progressively dissipate into smaller ones. In this process, turbulence kinetic energy is transferred from larger to smaller eddies until it dissipates into the heat. This procedure is known as the energy cascade, Figure 2.10.

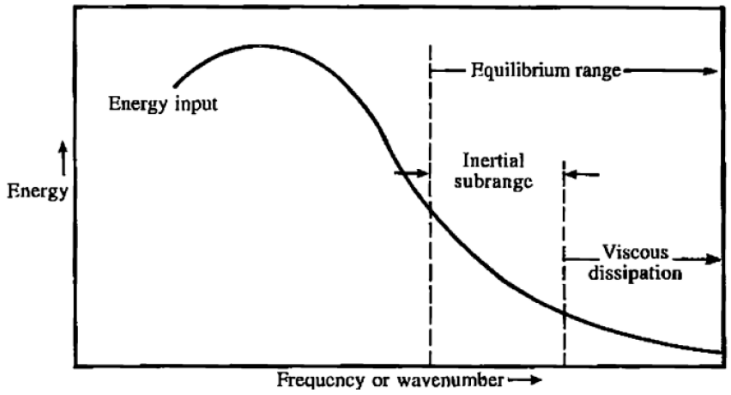

Figure 2.10 Energy cascade scheme, [11]

It can be observed that the highest energy is not contained within the largest eddies but in slightly smaller vortices. In the inertial subrange, inertial forces play a major role and the curve is in agreement with the Kolmogorov model,

$$S_u(f) \approx k_w^{-2/3}, \tag{2.16}$$

where k_w is the wave number. In the inertial subrange, turbulence kinetic energy gradually decreases with decreasing size of the eddies. While small eddies at high frequencies dissipate into the heat.

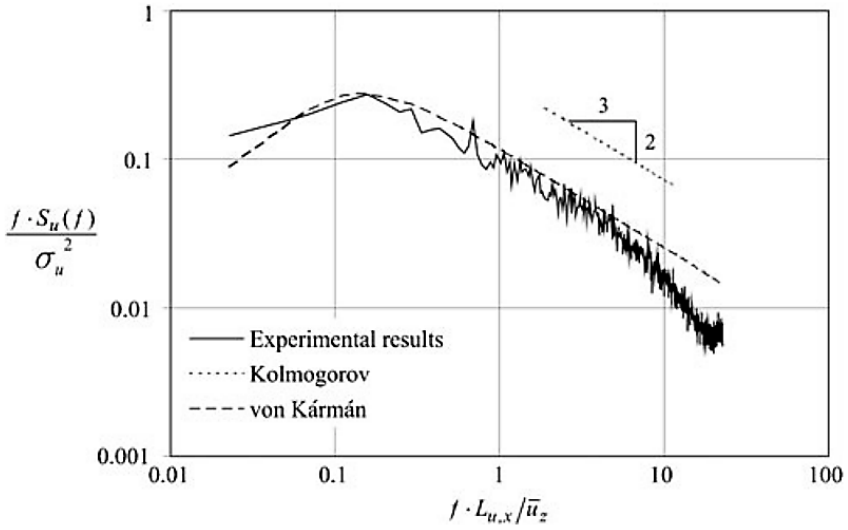

Figure 2.11 Comparison of design curves with experimental results for the power spectral density of wind velocity fluctuations, [12]

2.2.1.5 Reynolds shear stress

The friction forces between the ground surface and the air are transferred through the layers of the ABL by means of the shear stress. Shear stress is calculated as the sum of viscous and turbulent (Reynolds) stress,

$$\tau = \mu \frac{\partial \bar{u}}{\partial z} - \rho \overline{u'w'}. \tag{2.17}$$

Viscous stress $\mu\frac{\partial\bar{u}}{\partial z}$ has a maximum value on the surface and decreases strongly with an increase in height from the surface. In the inertial sublayer, viscous forces are negligibly small, Figure 2.12.

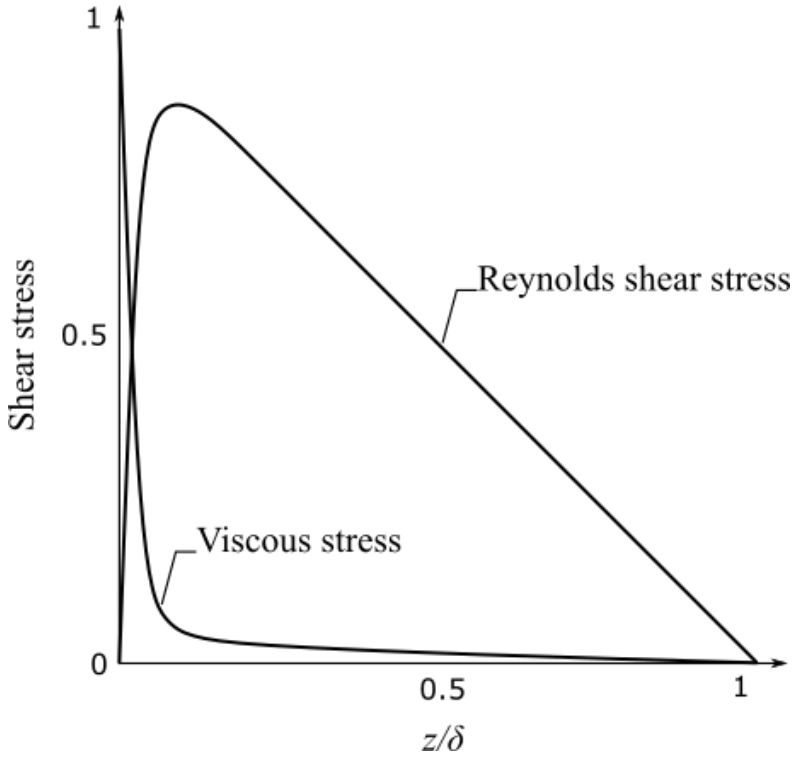

Figure 2.12 Shear stress in the boundary layer

Reynolds shear stress $\rho\overline{u'w'}$ is zero on the ground, and it increases rapidly up to the inertial sublayer. Through the inertial sublayer, the turbulent shear stress remains nearly constant (Prandtl constant-flux layer). With further increasing the height, Reynolds shear stress decreases to zero. Reynolds shear stress components $\rho\overline{u'v'}$, and $\rho\overline{v'w'}$ are substantially smaller compared to $\rho\overline{u'w'}$, so they are commonly neglected. Turbulent shear is defined as

$$\tau = -\rho\overline{u'w'} = \rho u_\tau^2(1 - z/\delta)^2, \tag{2.18}$$

where u_τ is friction velocity, and z/δ is a non-dimensional height in the ABL.

2.3 Bluff body aerodynamics

The scope of this thesis is in building aerodynamics. Buildings are generally classified as bluff bodies. Wide separation regions characterize the flow around bluff bodies in contrast to the streamlined bodies defined by close contours of streamlines around the body. Figure 2.13 shows streamlines around an airfoil (streamlined body) and a rectangle (bluff body).

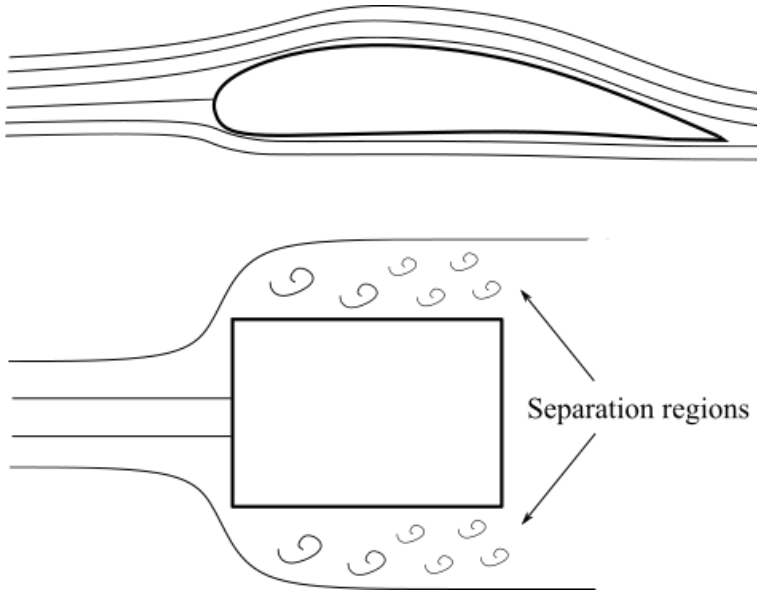

Figure 2.13 Airflow around streamlined and bluff bodies

It can be observed that around the airfoil there are no separation regions as the flow is attached to the body surface in the form of a turbulent boundary layer. In the flow around the bluff body, the free stream flow is separated from the body surface, the range commonly known as the separated shear layer.

2.3.1 Pressure coefficient

The pressure at the body surface is commonly expressed in a non-dimensional form as

$$C_p = \frac{p - p_0}{\frac{1}{2}\rho_a U_0^2}, \tag{2.19}$$

where p is the total pressure at the measuring point, p_0 is the static pressure in the free stream (undisturbed) flow, and $\frac{1}{2}\rho_a U_0^2$ is the dynamic pressure. In theory, the largest value of the positive pressure coefficient is 1.0, and it is achieved in the stagnation point on the windward body surface. The pressure coefficient on all other surfaces is negative, and its magnitude may be larger than 1.0.

2.3.2 Force coefficients

The non-dimensional force coefficient is defined as

$$C_F = \frac{F}{\frac{1}{2}\rho_a U_0^2 A}, \tag{2.20}$$

where F is the aerodynamic force, and A is the reference area commonly defined as the projected frontal area of the body.

Aerodynamic forces are analyzed in two directions, i.e. parallel and perpendicular to the main wind direction. The force parallel to the main wind direction is the along-wind force component, while the perpendicular force is the cross-wind force component.

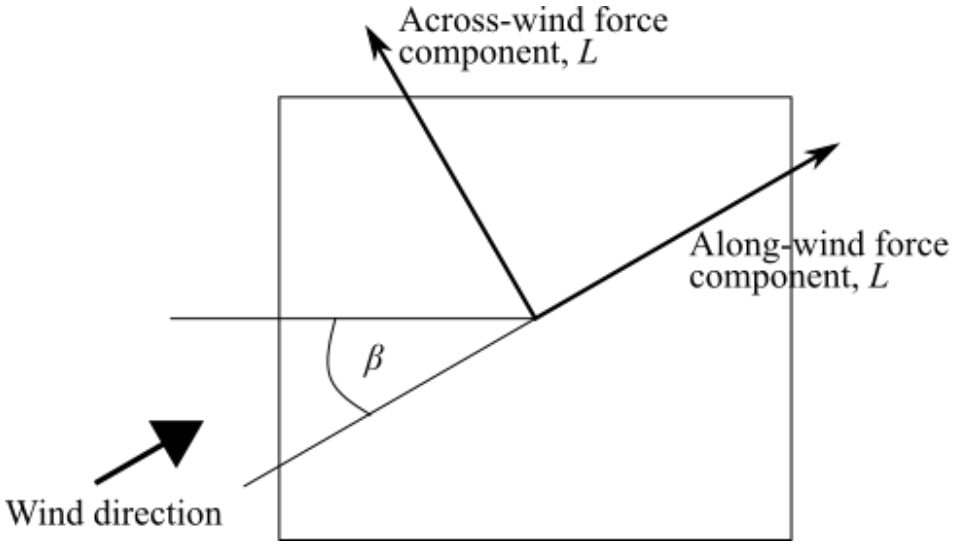

Figure 2.14 Coordinate axes of the forces acting on the building model, [8]

The force coefficients are defined as

$$C_D = \frac{D}{\frac{1}{2}\rho_a U_0^2 A}, \qquad C_L = \frac{L}{\frac{1}{2}\rho_a U_0^2 A}. \tag{2.21}$$

2.4 Wind effects on tall buildings

Tall buildings are generally considered bluff bodies. A medium or high height to width ratio (aspect ratio) is the main characteristic of tall buildings. Wind flow around tall buildings is schematically shown in Figure 2.15.

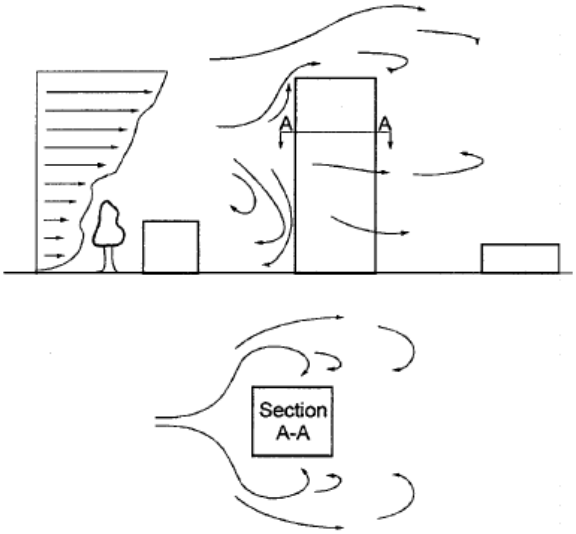

Figure 2.15 Wind flow around a tall building, [8]

The stagnation point of the flow is at 70% to 80% of the total building height [8]. Below the stagnation point, a strong downward flow adversely affects pedestrian comfort. The flow separates from each windward corner of a building, generating strong vortices associated with the suction regions on the underlying surfaces. The characteristics of this downward flow depend on wind flow conditions and building dimensions, where the re-attachment of the flow may occur. The leeward building surface is characterized by negative pressure with a magnitude of around 50% of the pressure magnitude on the windward building surface. On the windward building surface, Figure 2.16, the largest value of the pressure coefficient is

commonly 0.9, which is lower than in theory, which is due to the wind flow around the building. In the presented case, there is no re-attachment of the flow on the lateral and top building surfaces, a phenomenon directly influenced by the turbulence in the wind flow.

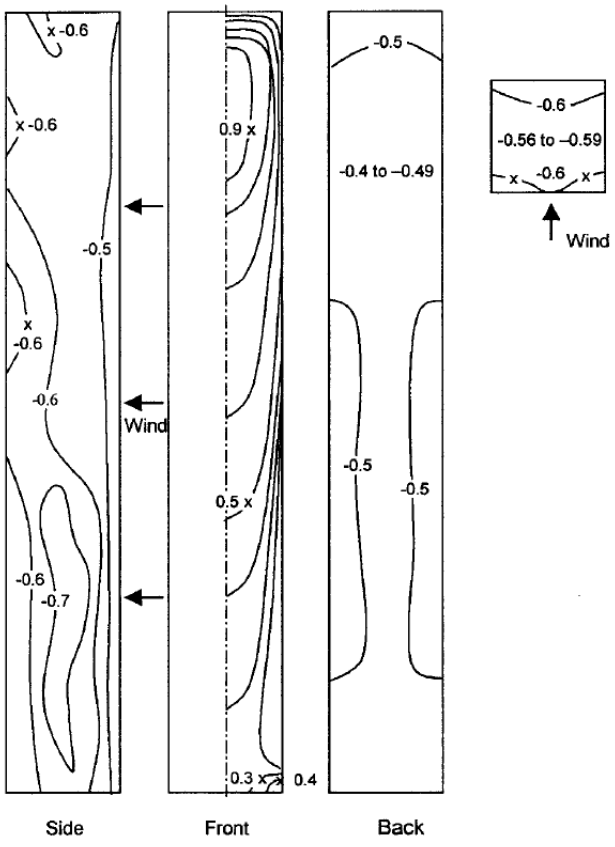

Figure 2.16 Mean pressure coefficients on a tall building subjected to the atmospheric boundary layer, [8]

2.5 Porous materials in building engineering

Porous two-phase materials generally enable the flow through its surface. The first phase is solid, where there is no fluid flow, while the other phase consists of pores, and there is a flow through these pores. Porous materials generally have a wide range of applications, from various air filters to materials designed to increase the energy efficiency of buildings and human comfort.

In the present thesis, the focus is on the application of PDSF systems on tall buildings. Louvres are a common type of porous building façades. They are horizontally or vertically oriented metal panels with a possibility of adjusting the wind incidence angle.

Figure 2.17 Louver façade

Louvres control the natural lighting and natural ventilation in buildings. Perforated plates are also used as DSF systems. The advantage of using perforated plates is in various patterns that can be designed and thus enhance the visual appearance of buildings. It was previously reported that the implementation of DSF systems can reduce the effective heat transfer coefficient by up to 27% [13]. On the other hand, perforated plates are fixed and can not be controlled to influence the natural lighting, as is the case with louvres. In this thesis, the DSF system consists of an inner impermeable façade and an outer porous façade made of perforated aluminium plates.

Figure 2.18 DSF system with perforated plates

3 Methodology

3.1 CRIACIV boundary layer wind tunnel

Experiments were performed in a boundary layer wind tunnel (BLWT) of the Inter-University Research Centre on Building Aerodynamics and Wind Engineering (CRIACIV) at the University of Florence, Italy. This is an open-return wind tunnel with a closed test section, Figure 3.1.

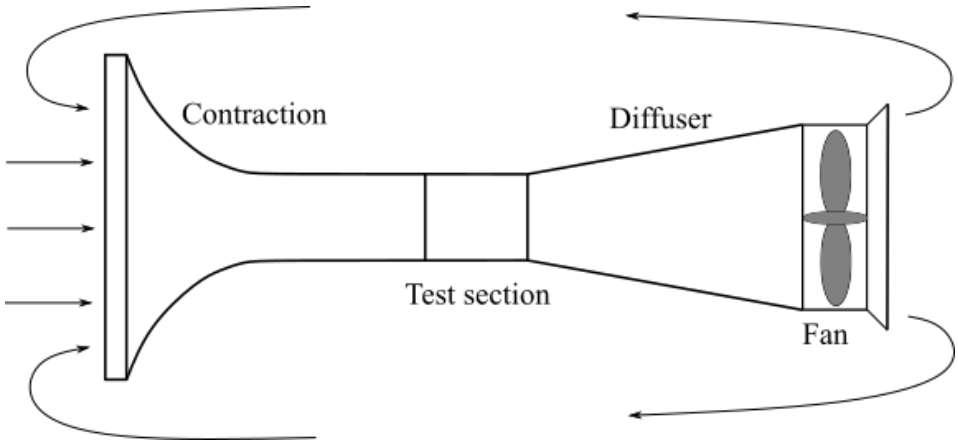

Figure 3.1 Schematic view of an open-return wind tunnel with a closed test section

Air flow in the CRIACIV BLWT was generated using a 1.9 m diameter fan located at the end of the wind-tunnel test section. 160 kW fan power can generate a speed of up to 30 m/s in the 2.2 m wide and 1.6 m height test section. The total length of the wind tunnel is 22 m.

3.2 Building models

Nine building models with the same dimensions are designed to study the aerodynamic characteristics of the building model equipped with a PDSF system. The studied building model is situated in the model urban environment (3x3 in-line pattern). The aspect ratio of the building models is 1:1:5 with dimensions of 100 mm x 100 mm x 500 mm. Eight building models were used as dummies, thus without a PDSF system, as they have a smooth, single façade without porosities. On the other hand, the studied model building is equipped with the PDSF system. The PDSF system consists of an outer porous façade made of perforated

aluminium plates, which are offset from the smooth inner façade by 5 mm. Figure 3.2 shows the example of an arrangement of model buildings situated in the model urban environment.

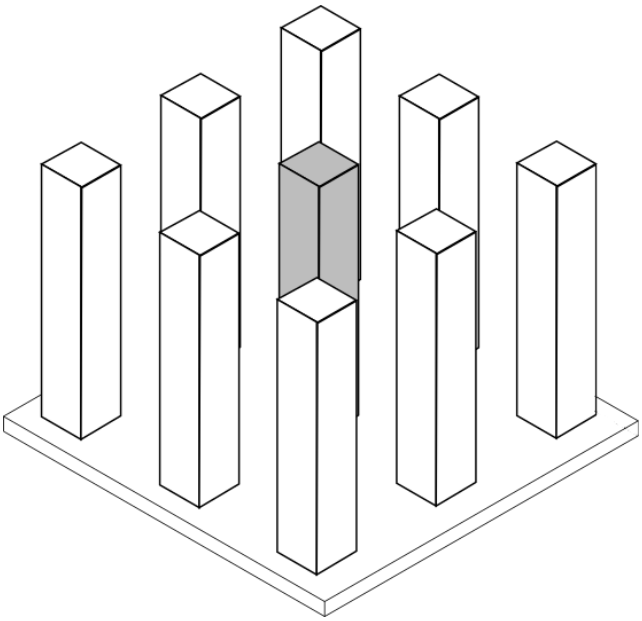

Figure 3.2 Arrangement of model buildings situated in the model urban environment (3x3 in-line pattern); the studied model building is presented with a grey surface, while the surface of dummy model buildings is shown in white colour

The building model equipped with the DSF system is shown in Figure 3.3.

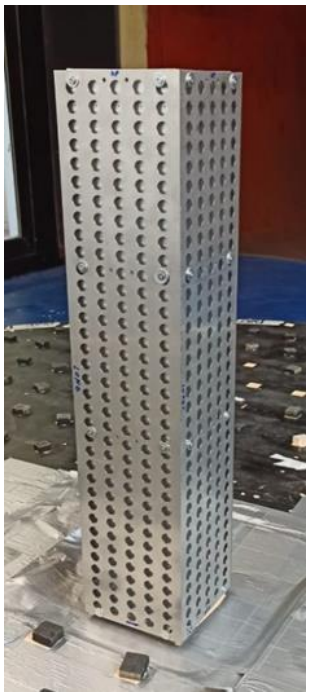

Figure 3.3 Studied model building equipped with a DSF system

Two different porosities were studied in the experiments, i.e. 25% and 50%, Figure 3.4. The porosity was calculated as the ratio between the outer façade openings area and the total area of the façade.

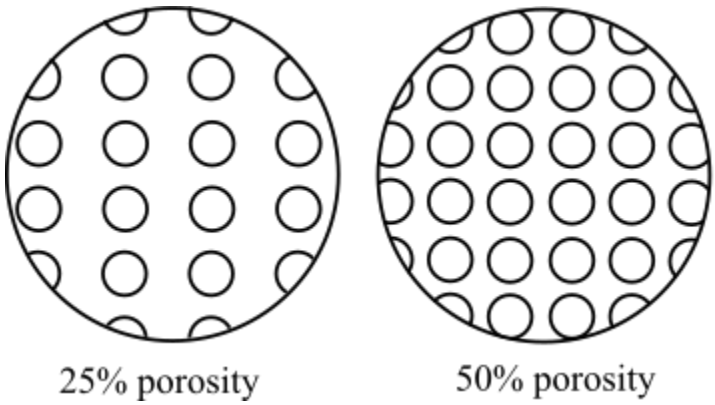

Figure 3.4 Schematic view of the 25% and 50% porosity surfaces

The building model was mounted on the high-frequency force balance (HFFB) to measure integral aerodynamic loading of the studied model building in three directions. In order to equip the model building with a pressure measuring system, the inner façade of the model building was drilled in an array of 0.8 mm diameter openings connected to the tubing system. On each surface of the porous model façade, eight rows and five columns of openings are distributed in an in-line pattern. Figure 3.5 and Figure 3.6 show the tubing system in the model building and an arrangement of pressure taps on its inner façade, respectively.

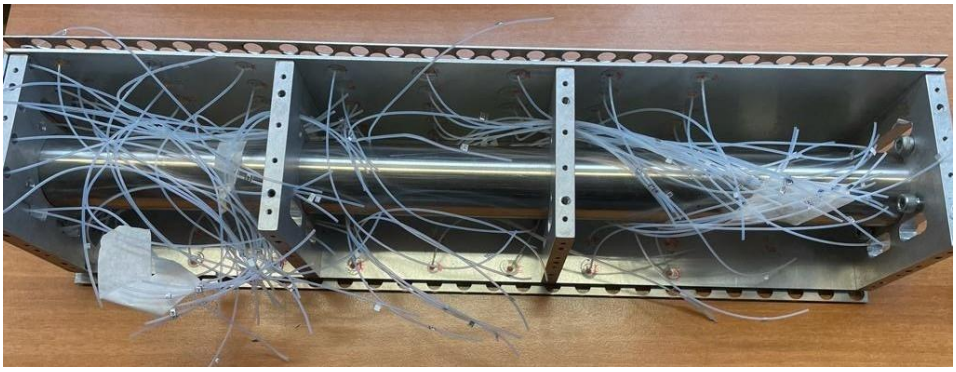

Figure 3.5 Tubing system in the model building

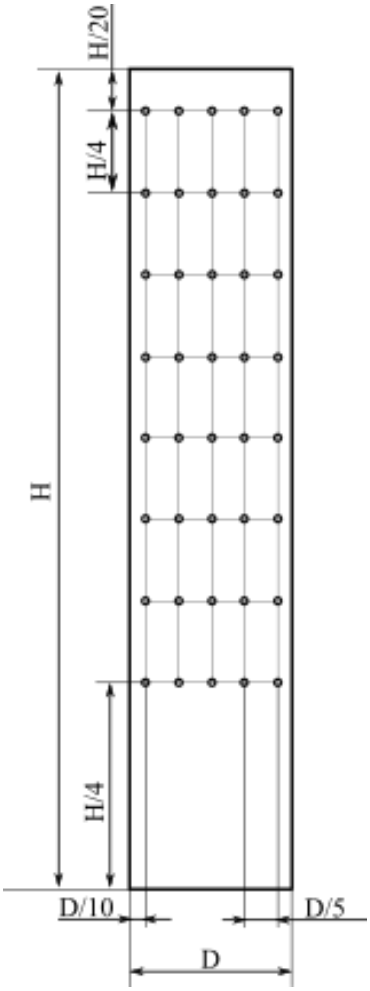

Figure 3.6 Pressure tap arrangement on the inner façade of the model building

3.3 Atmospheric boundary layer simulation

Vortex generators, barrier walls and surface roughness have been commonly used to create the ABL simulations. The height and distribution of surface roughness elements largely determine the mean velocity and turbulence intensity profiles. At the same time, the barrier wall contributes to the loss of momentum in the lower part of the ABL simulation. In the present thesis, only the barrier wall and surface roughness elements were used, thus without an application of vortex generators, Figure 3.7 and Figure 3.8.

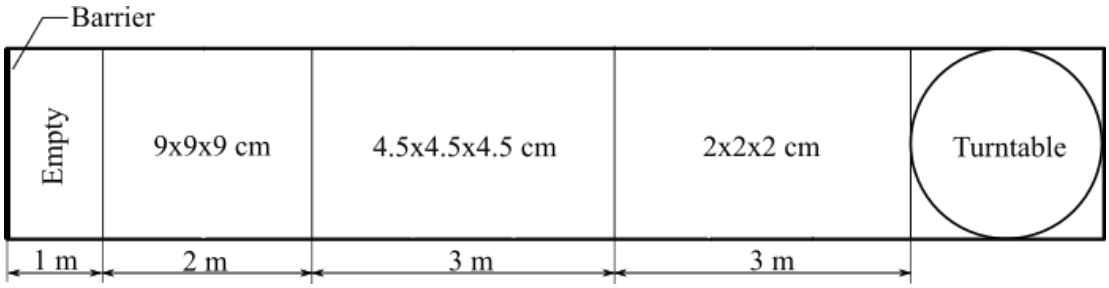

Figure 3.7 Schematic view of the wind-tunnel test section with indicated dimensions of surface roughness elements

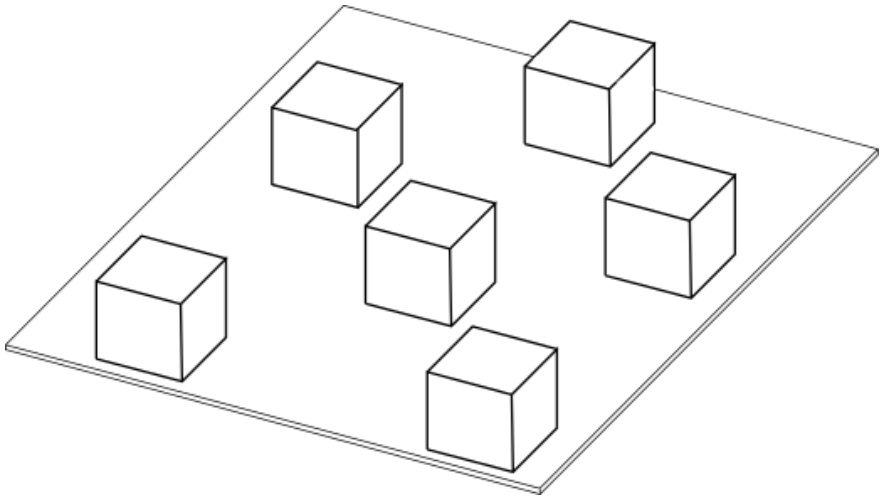

Figure 3.8 Staggered arrangement of surface roughness elements

A proper arrangement of surface roughness elements was determined by the trial and error approach. The goal was to create the ABL simulation comparable to the wind category 3 recommended in the Eurocode standard (EN1991-1-4:2005) [14].

The dimensions of the castellated barrier wall used in the experiments are shown in Figure 3.9.

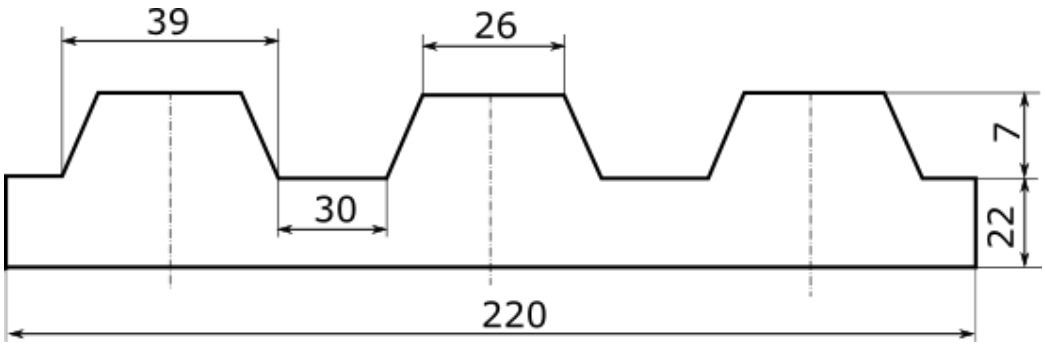

Figure 3.9 Schematic view of the castellated barrier wall

3.4 Hot-wire anemometry

Velocity measurements in wind tunnels have been commonly carried out using the Prandtl-Pitot tubes and hot-wire anemometry systems. Both transducers are small enough not to cause a significant pressure drop and flow disturbance. The working principle of the Prandtl-Pitot tube is in determining the flow velocity based on the difference between the total and static pressures in the flow. It is commonly used to determine the mean flow velocity, while it is inadequate for measuring flow velocity fluctuations.

On the other hand, hot-wire anemometers may be used to measure both the mean flow velocity and flow fluctuations. This approach is based on the analysis of the heat transfer between the heated hot-wire and the airflow. The anemometer probe is usually shaped like a small cylinder wire or a stretched thin film. Each wire or film is used to measure one flow velocity component. However, to measure two or three flow velocity components concurrently, the probes may be equipped with more wires, Figure 3.10.

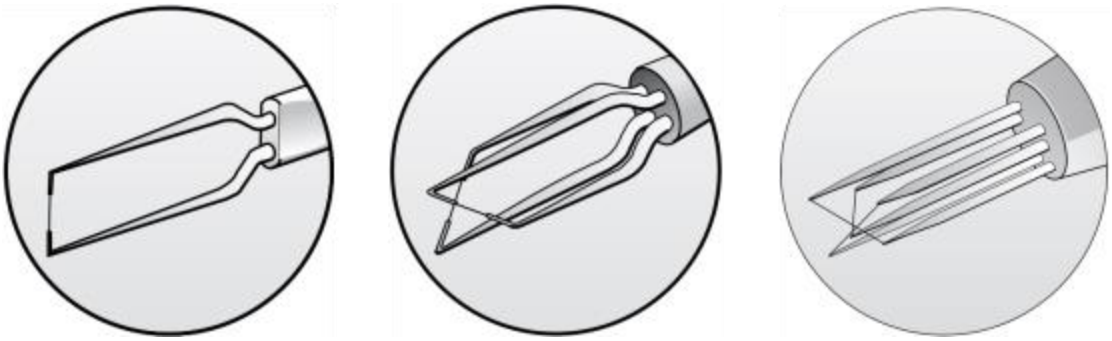

Figure 3.10 1D, 2D, and 3D hot-wire anemometer probes, [15]

There are four types of sensors, i.e. gold-plated wires, miniature wires, fiber-film, and film sensors. Gold-plated wires are suitable for high-turbulence one-dimensional flows. Miniature wires are recommended for low-turbulence flows, while they are also rigid and suitable for high-velocity measurements because of their small dimensions. Film sensors are quartz fibers covered by a thin nickel film. These sensors are primarily used in liquids where more rugged sensors are needed.

A current passing through the wire generates heat (Joule heating), and a part of the generated heat is dissipated by the forced convection from the airflow. The basic heat balance for the steady flow is defined as

$$R_{\mathrm{W}} I_{\mathrm{W}}^2 = (T_W - T_{\mathrm{a}}) \Phi_{\mathrm{conv}}(U). \tag{3.1}$$

The left-hand side of the equation represents the heat generated with the current intensity I_{W} through the sensor with resistance R_{W}. The right-hand side of the equation represents the heat transferred by the convection. T_{W} represents the wire temperature while operating, T_{a} is the wire temperature while it is not operating and $\Phi_{\mathrm{conv}}(U)$ is the convection function, which depends on the velocity in the direction normal to the wire.

In the turbulent flow, some heat remains in the sensor, and the heat balance is expressed as

$$m_{\mathrm{W}} c_{\mathrm{W}} = R_{\mathrm{W}} I_{\mathrm{W}}^2 - (T_{\mathrm{W}} - T_{\mathrm{a}}) \Phi_{\mathrm{conv}}(U). \tag{3.2}$$

The first term on the right-hand side of the equation is the heat stored in the sensor, where m_{W} is the sensor mass, and c_{W} is specific heat coefficient of the sensor.

Hot-wire anemometers may be Constant Voltage Anemometer (CVA), Constant Temperature Anemometer (CTA), and Constant Current Anemometer (CCA). For each of these anemometer types, one variable in term $R_W I_W^2$ of the equation (3.2) remains constant to measure only one physical quantity. Since the $R_W I_W$ represents the voltage, in the case of a CVA system, that term remains constant while the current intensity I_W is measured. In the CTA system, the temperature of the wire remains constant, which implies that the resistance of the wire is also constant. The only variable that can be measured in that case is the current intensity I_W. The CCA system maintains the current intensity constant and the change of resistance R_W is measured. In the present study, a CTA was used, Figure 3.11.

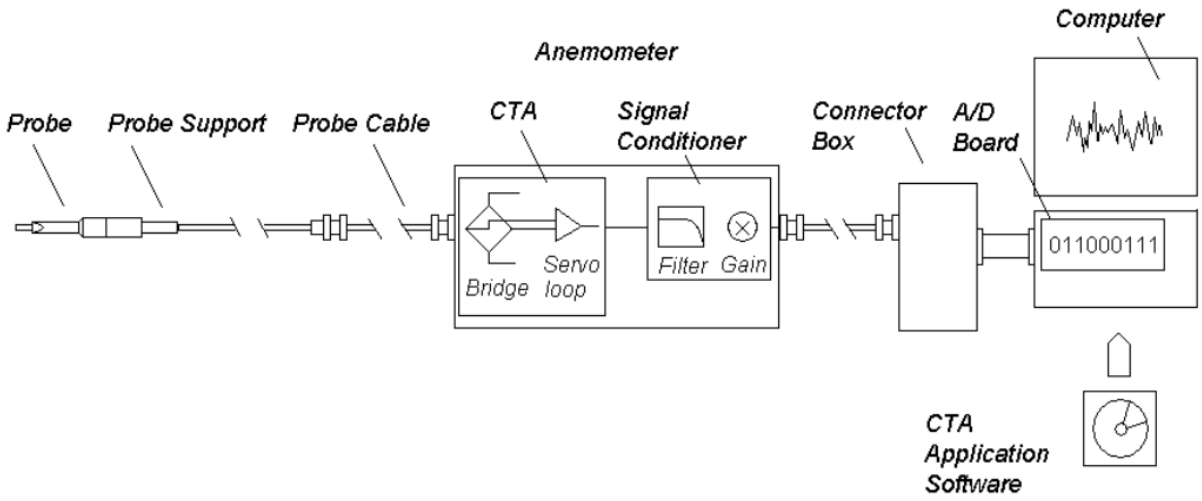

Figure 3.11 CTA measurement system, [16]

It consists of a probe mounted on its support, a probe cable that connects the anemometer with the probe sensor, an anemometer with the Wheatstone bridge and a conditioner for high- and low-pass filtering, A/D board for analog-to-digital signal conversion, and a personal computer for signal control, postprocessing and the analysis.

3.5 High-frequency force balance

High-frequency force balance (HFFB) is a commonly used approach to measure integral aerodynamic loads on structural models in wind-tunnel experiments. The loads measured on structural models are not the actual aerodynamic loads as they also account for the natural

frequency of the model-balance system. Therefore, to assess the actual aerodynamic forces and moments on the studied model building, the loads measured at the base of the model building need to be corrected and the amplification effects discarded. Hence, an impulse loading test was carried out first to determine the natural frequency of the model-balance system. This test involves exciting the model building with a plastic hammer and analyzing the free-vibration signal. After the natural frequencies are obtained, various filters are applied to cut off the frequencies near the natural frequency of the system. Figure 3.12 shows the power spectral density of the force fluctuations in this experiment. Two natural frequencies were observed at 28 Hz and 37 Hz. A low-pass filter was subsequently used to cut off these frequencies.

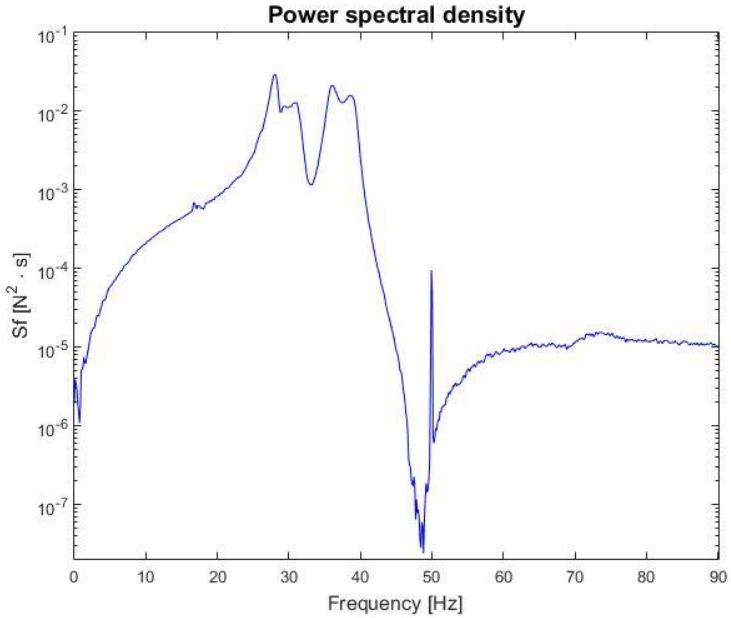

Figure 3.12 Power spectral density of force fluctuations in the preliminary experiments

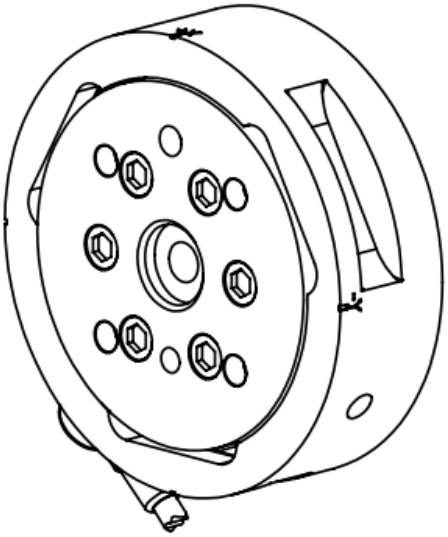

Figure 3.13 FT-Delta SI-165-15 by ATI Industrial Automation, [17]

Measurements were performed with FT-Delta SI-165-15 system by ATI Industrial Automation, Figure 3.13. It is a strain-gage multi-axis force and torque system that concurrently measures forces and moments in three directions. HFFB was calibrated at the smallest possible loading, Table 3.1.

Table 3.1 Calibration of the FT-Delta SI-165-15

Calibration	F_x, F_y	F_z	M_x, M_y	M_z
Range	165 N	495 N	15 Nm	15 Nm
Resolution	1/32 N	1/16 N	1/528 Nm	1/528 Nm
Accuracy	± 0.06%	± 0.06%	± 0.01%	± 0.01%

3.6 Surface pressure measurement system

Surface pressure measurements on the inner façade of the model building were carried out using a PSI-DTC Initium pressure measurement system together with four miniature 32 port DTC scanners. DTC Initium is a data acquisition system that supports eight miniature 32 or 64 port DTC scanners capable of measuring 512 pressure points. DTC pressure scanners are differential pressure measurement units. Each of 32 or 64 ports consists of a silicon piezoresistive pressure sensor that transfers the analog signal to the A/D converter. The sampling frequency in the experiments was 500 Hz at 100 s time record length, Figure 3.14.

Figure 3.14 DTC pressure scanner

The tubing connects the measuring points with the port in the pressure scanner and the DTC initium system, Figure 3.15.

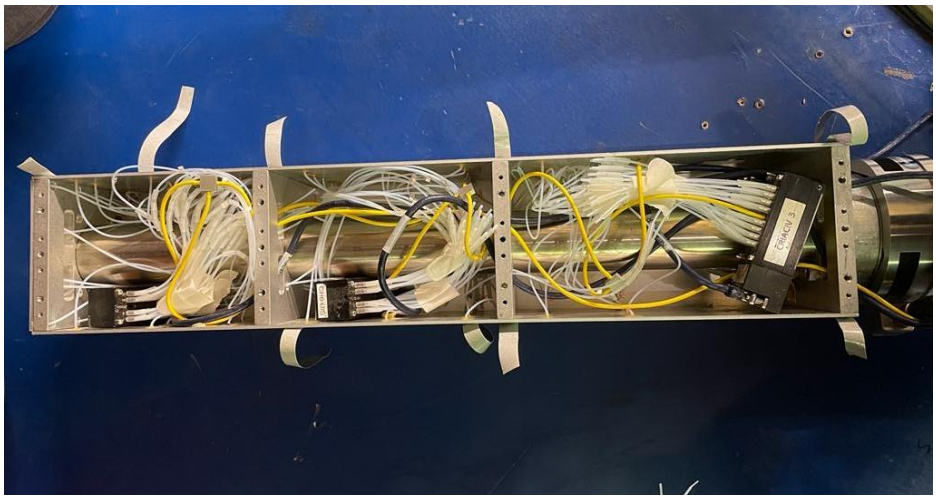

Figure 3.15 Pressure system in the model building

3.7 Experimental setup and overview

Before the main experimental campaign on the model building equipped with the PDSF system situated in a model urban neighbourhood, a single model building with a single-skin non-porous façade was studied as a reference case. The goal of these measurements was to validate the results with the data from the Aerodynamic Database of High-rise Buildings of Tokyo Polytechnic University [18]. While the ABL profiles in the present experiments were

not the same as in [18], these two ABL simulations were similar enough to be used for validation purposes.

The experiments were arranged in two sets. The first set of experiments focused on the effect of the porosity of the PDSF system (25% and 50% porosities) for one arrangement of a model urban neighbourhood. In the second set, the effect of the spacing between model buildings in the model urban environment was analyzed at 25% porosity of the PDSF system.

In all experiments, surface pressures and aerodynamic loads on the base of the model building were assessed. The wind velocity was at maximum to allow for a proper recording of the highest loads on the HFFB, but also to achieve the vortex-induced vibration frequency lower than the natural frequency of the model building, thus avoiding the model building resonance. As a result, a wind flow velocity of ~16 m/s was determined and applied in all experiments. Since the model building cross-section is a square with four axes of symmetry, for each set of the HFFB experiments, it was sufficient to rotate the model from 0° to 45° with a step of 5°. The pressure taps were connected on surfaces A and B. The model building was accordingly rotated in the range of the wind incidence angles from 0° to 45° and from 180° to 225° with a step of 15°, Figure 3.16.

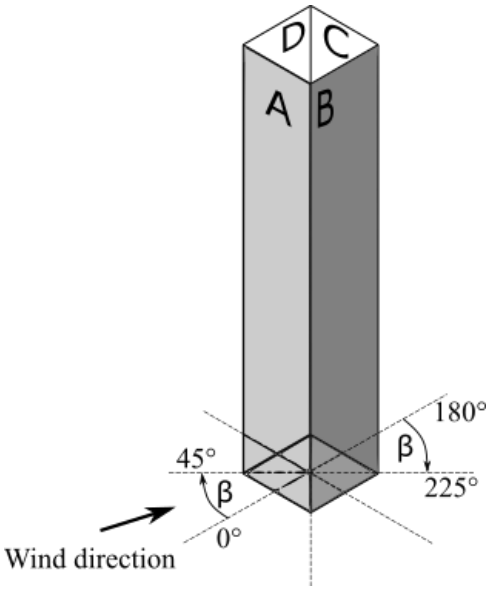

Figure 3.16 Studied wind incidence angles β on the model building

3.7.1 First set of experiments

The spacing between the models was $d = 5a$, where a is the width of the building (a = 100 mm). While the distance between the model buildings was constant, the studied model building was tested for various PDSF system porosities:

1) Studied model building without a PDSF system (single-skin non-porous façade),
2) Studied model building with a PDSF system of 25% porosity on the outer façade,
3) Studied model building with a PDSF system of 50% porosity on the outer façade.

Configurations studied in the pressure measurements are outlined in Figure 3.17.

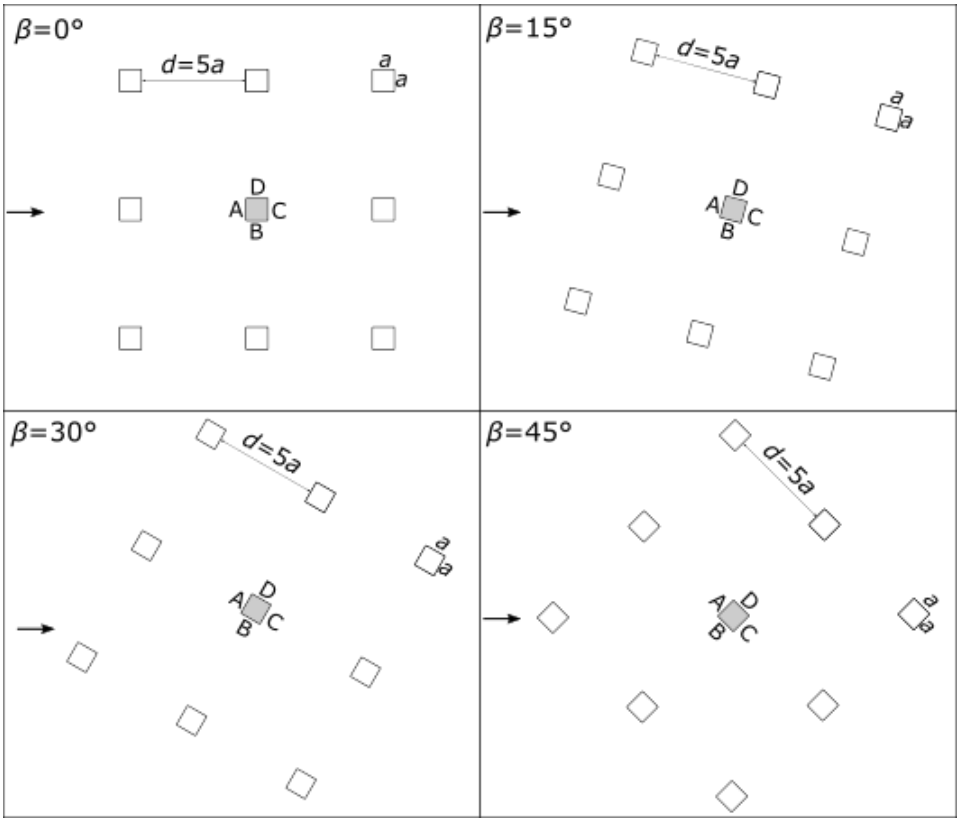

Figure 3.17 Wind incidence angles β in pressure measurements in the first set of experiments

3.7.2 Second set of experiments

The second set of experiments addressed the effect of spacing between model buildings in a model urban environment. Therefore, measurements were done for three different spacings:

1) Small spacing between model buildings, i.e., $d = a = 100$ mm,
2) Medium spacing between model buildings, i.e., $d = 3a = 300$ mm,
3) Large spacing between model buildings, i.e., $d = 5a = 500$ mm.

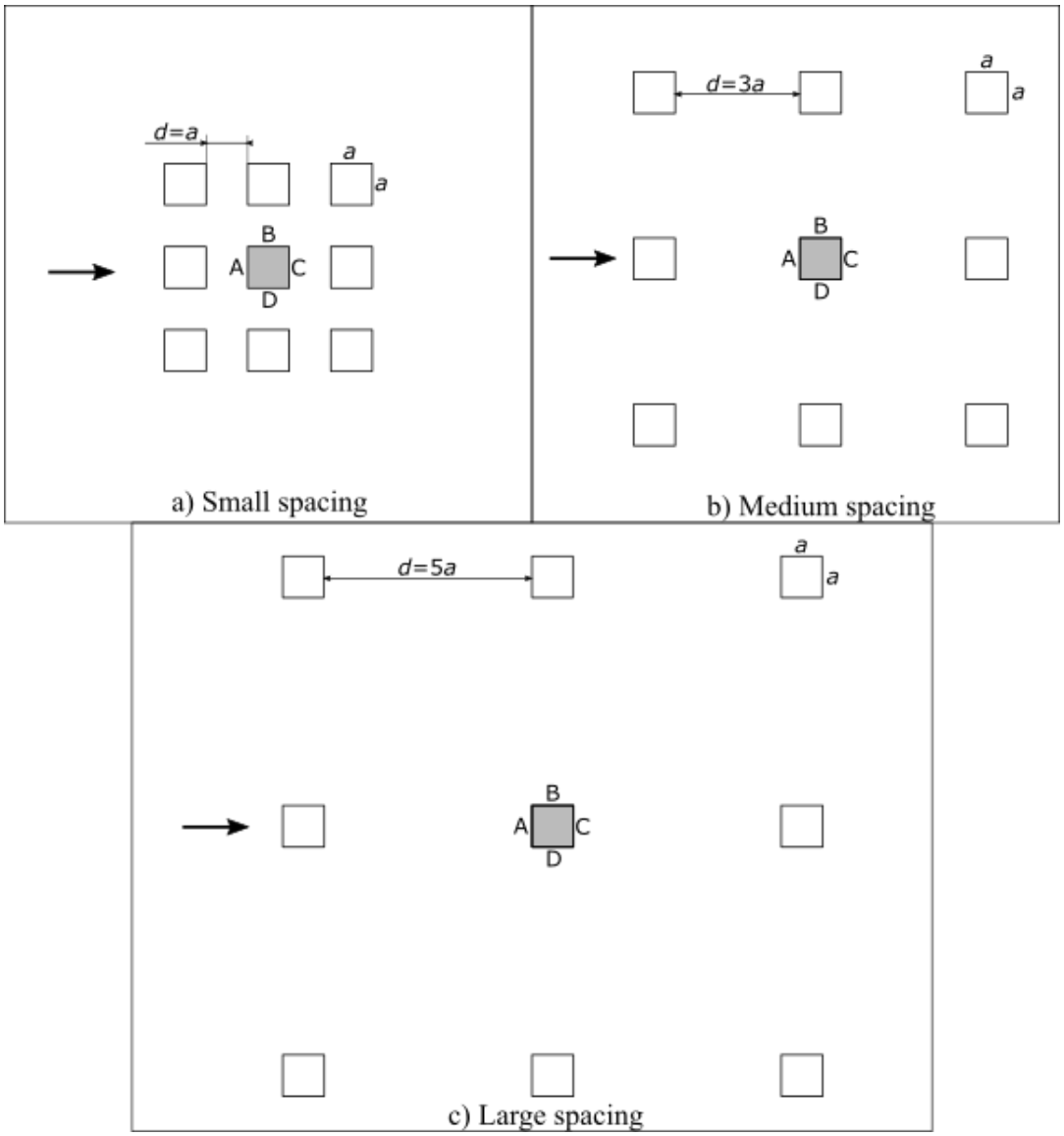

Figure 3.18 Studied spacing between model buildings

Two configurations of the studied model building were analyzed. The studied model building was without a PDSF system first, while in subsequent experiments, the model building was equipped with a PDSF system characterized by 25% porosity of the outer model façade.

4 Results and discussion

4.1 Atmospheric boundary layer simulation

The created ABL simulation attempted to model the ABL characteristics recommended in the EN1991-1-4:2005 [14] standard. In this standard, there are in total five terrain categories characterized by their respective surface roughnesses, while in the present thesis, wind conditions for the category three were simulated, Table 4.1.

Table 4.1 Terrain categories recommended in the EN1991-1-4:2005 [14] standard

Terrain category	z_0, m	z_{min}, m
0 Sea or coastal area exposed to the open sea	0.003	1
I Lakes or flat and horizontal area with negligible vegetation and without obstacles	0.01	1
II Area with low vegetation such as grass and isolated obstacles (trees, buildings) with separations of at least 20 obstacle heights	0.05	2
III Area with regular cover of vegetation or buildings or with isolated obstacles with separations of maximum 20 obstacle heights (such 0,3 5 as villages, suburban terrain, permanent forest)	0.3	5
IV Area in which at least 15 % of the surface is covered with buildings and their average height exceeds 15 m	1.0	10

4.1.1 Mean velocity profile

Mean wind velocity profiles are shown in Figure 4.1. The non-dimensional form of the height z is achieved by dividing it with the reference height z_{ref} that represents the model building height. The mean wind velocity was normalized using the reference velocity U_{ref}, which is the velocity measured at the top of the model building. The obtained results agree with the mean wind velocity profile of the EN1991-1-4:2005 [14] category three type of terrain.

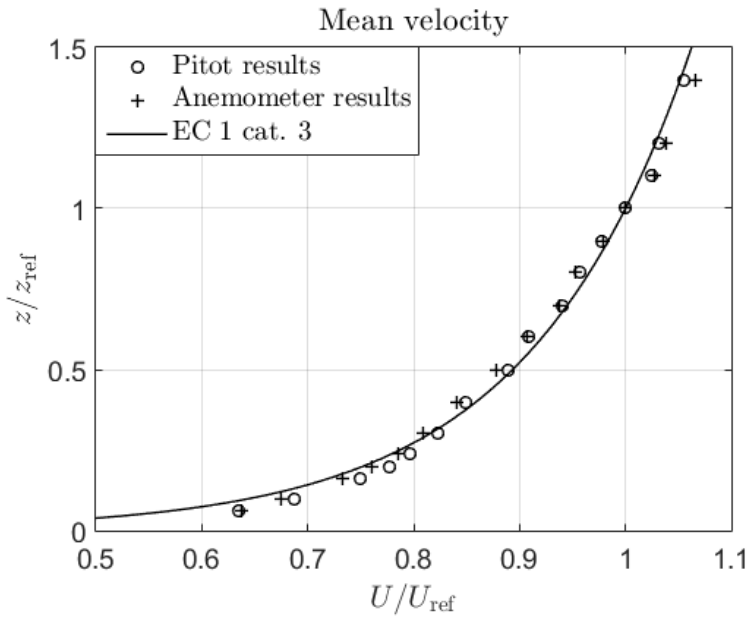

Figure 4.1 Measured mean wind velocity profile in comparison with the EN1991-1-4:2005 [14] standard category 3

In order to analyze flow uniformity in the main flow direction, the mean wind velocity profiles were measured in three different longitudinal planes, i.e. the model building position, 30 cm upwind of the model building position, and 30 cm downwind of the model building position, Figure 4.2.

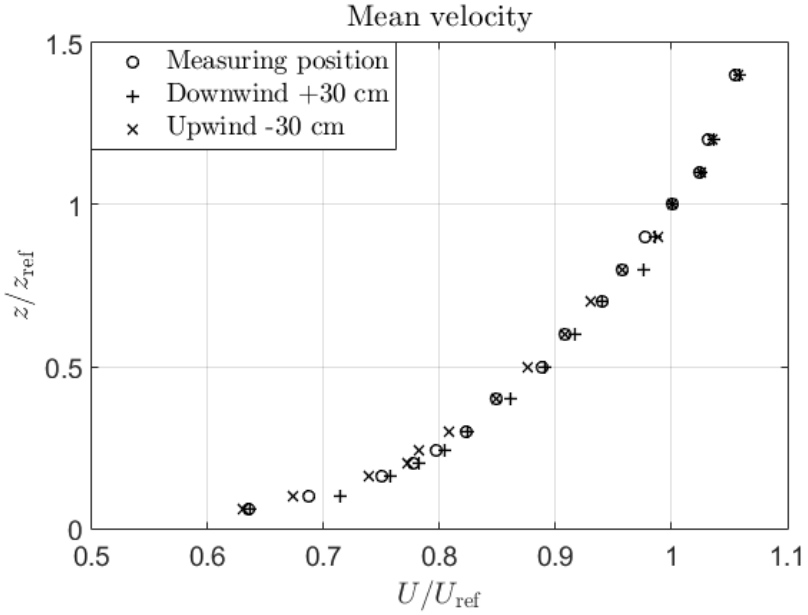

Figure 4.2 Mean velocity profiles measured in three different longitudinal planes

There are slight discrepancies in the mean wind velocity profiles along the main wind direction. These effects may be observed in the lower parts of the ABL simulation and are to be attributed to local phenomena that affect the measurement, e.g., probe position relative to surface roughness elements. In general, these results may be adopted to prove the flow uniformity in the main flow direction.

The experimental results regarding surface pressure on a model building were validated using the Aerodynamic Database of High-rise Buildings of Tokyo Polytechnic University [18]. In order to allow for using these [18] results as a benchmark, it was essential to compare the created ABL simulation with the ABL simulation reported in [18] first, Figure 4.3. These two mean wind velocity profiles differ to some extent closer to the ground surface, while their agreement is better in the upper portions of the ABL simulations. Although these two mean wind velocity profiles do not match perfectly, their agreement is good enough to allow for the validation of the results obtained in the framework of the present thesis.

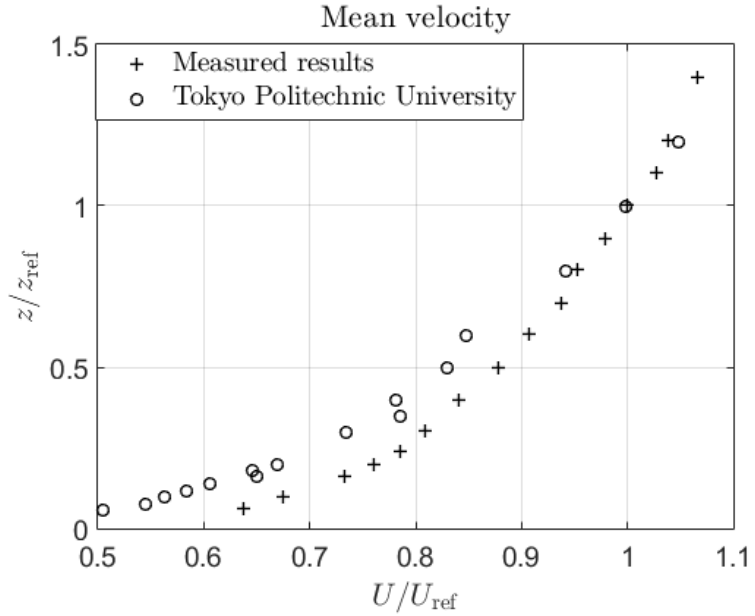

Figure 4.3 Comparison of the Tokyo Polytechnic University and measured velocity profiles

4.1.2 Turbulence intensity

Turbulence intensity profiles in the longitudinal wind direction are shown in Figure 4.4. The experimental data agree reasonably well with the EN1991-1-4:2005 [14] recommendations. Uniformity of the turbulence intensity in the longitudinal (main) wind directions was achieved, Figure 4.5.

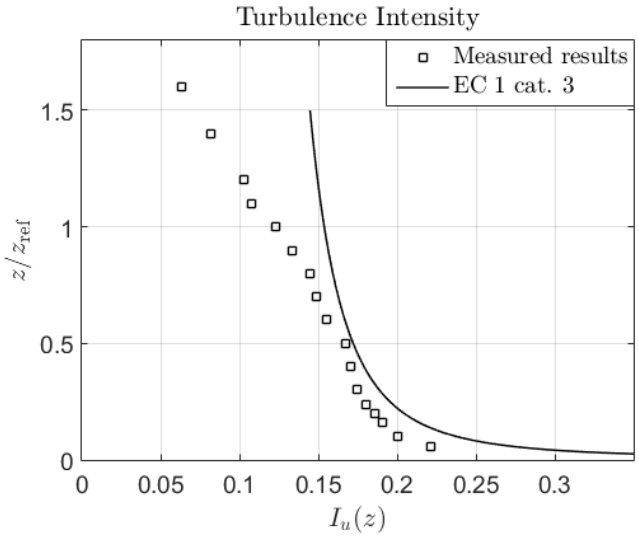

Figure 4.4 Turbulence intensity profile in comparison with the EN1991-1-4:2005 [14] category 3 standard recommendations

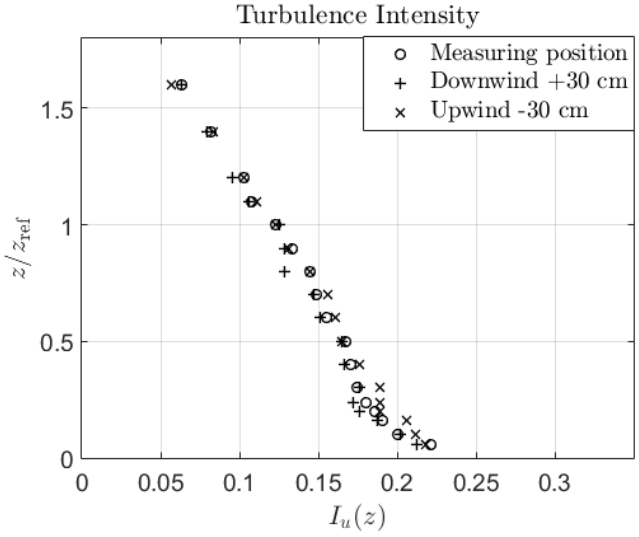

Figure 4.5 Turbulence intensity profiles at three various positions in the main wind direction

Integral turbulence length scales in the created ABL simulation increased with increasing the height from the ground surface up to z/z_{ref}~0.5, Figure 4.6. Higher from z/z_{ref}~0.5, integral turbulence length scales remain nearly constant. This phenomenon occurs because of the geometrical limitations of the wind-tunnel test section, which do not allow turbulent eddies fully to develop. In nature, large eddies develop without constraints, a fact that explains a poor correlation of the model and full-scale profiles of turbulent eddies in the higher portion of the created ABL simulation.

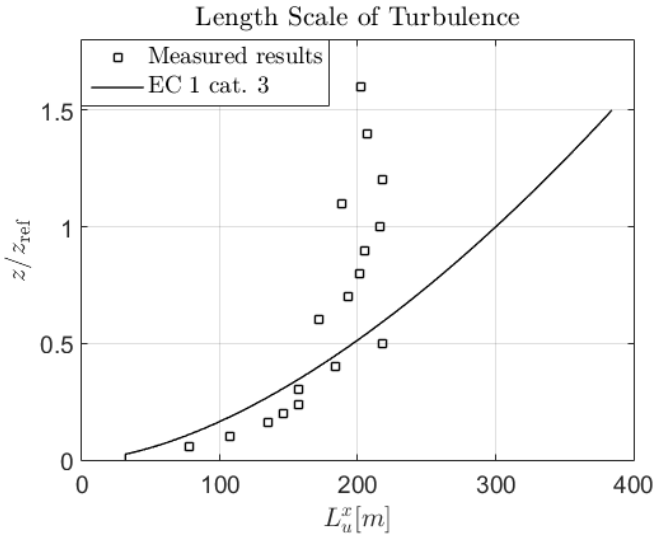

Figure 4.6 Measured length scale of turbulence in comparison with the standard EN1991-1-4:2005 [14] category 3

4.2 Validation case

A stand-alone building with a single-skin façade was employed in the validation experiment. The Tokyo Polytechnic University data were compared with measured experimental regarding the surface pressure for this purpose. Figure 4.7 and Figure 4.8 show the pressure fields for the 0° wind incidence angle. Two surfaces of the model building were analyzed, i.e. windward and right-hand side (surface A and B), Figure 3.16. The trends of pressure fields are entirely the same, while the values in the performed experiments are slightly lower concerning the Tokyo Polytechnic University data. This discrepancy is due to the differences in the two compared ABL profiles. The performed validation exercise proved a good quality of the experimental setup used in the present thesis.

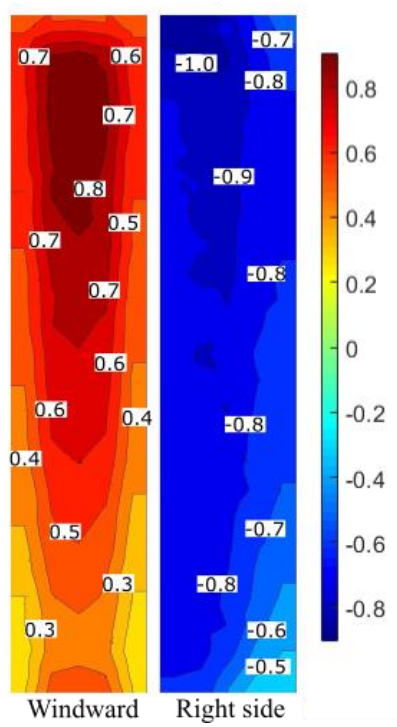

Figure 4.7 Tokyo Polytechnic University pressure field at the 0° wind incidence angle

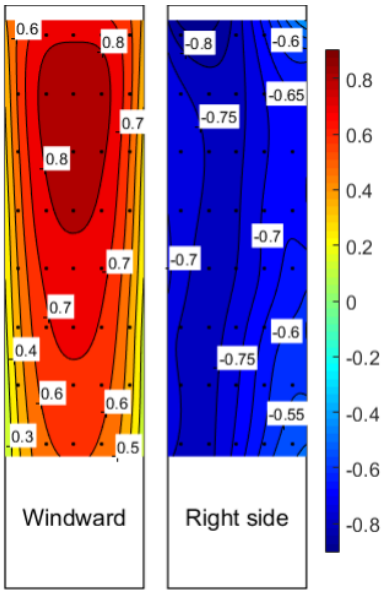

Figure 4.8 Stand-alone model building pressure field at the 0° wind incidence angle

In this experiment, the Tokyo Polytechnic University pressure data were integrated over the respective model building surface and compared with the results obtained using the own HFFB results, Table 4.2.

Table 4.2 Comparison of the Tokyo Polytechnic University data and the own HFFB along-wind moment coefficient results

	Tokyo Polytechnic University data	**HFFB**
C_{MD}	0.592	0.5302

The HFFB results proved to be nearly the same as the Tokyo Polytechnic University data, a fact that may be adopted as validation proof for the proper functioning of the HFFB system used in the present thesis.

4.3 Forces and moments on building models in an urban environment

The loads measured on the HFFB were not very large because of the surrounding dummies sheltering the studied model. The main focus of the present analysis was thus on measuring wind loads regarding along-wind and across-wind moment coefficients.

First set of experiments

Figure 4.9 shows the along-wind moment coefficient dependence on the wind incidence angle for a model building situated in the model urban environment (d = 5a). There is no noticeable difference regarding the along-wind moment coefficient when using a PDSF system. The maximum magnitude is achieved at a 25° wind incidence angle for each studied case.

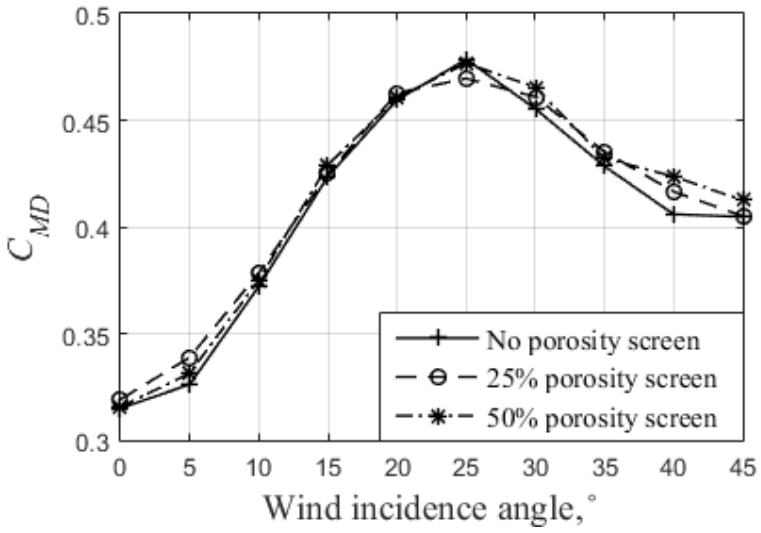

Figure 4.9 Along-wind moment coefficients for a building model as a part of the urban environment ($d = 5a$)

The reason for this phenomenon is the passage of the wind between the two dummy model buildings as the airflow directly impinges on the studied model building. At other angles, this passage space is smaller, or even fully closed at 0° and 45° wind incidence angles when the model building is entirely sheltered by the dummy model building upwind of the studied model building. Figure 4.10 shows the closed passage (left) and open passage (right) scheme.

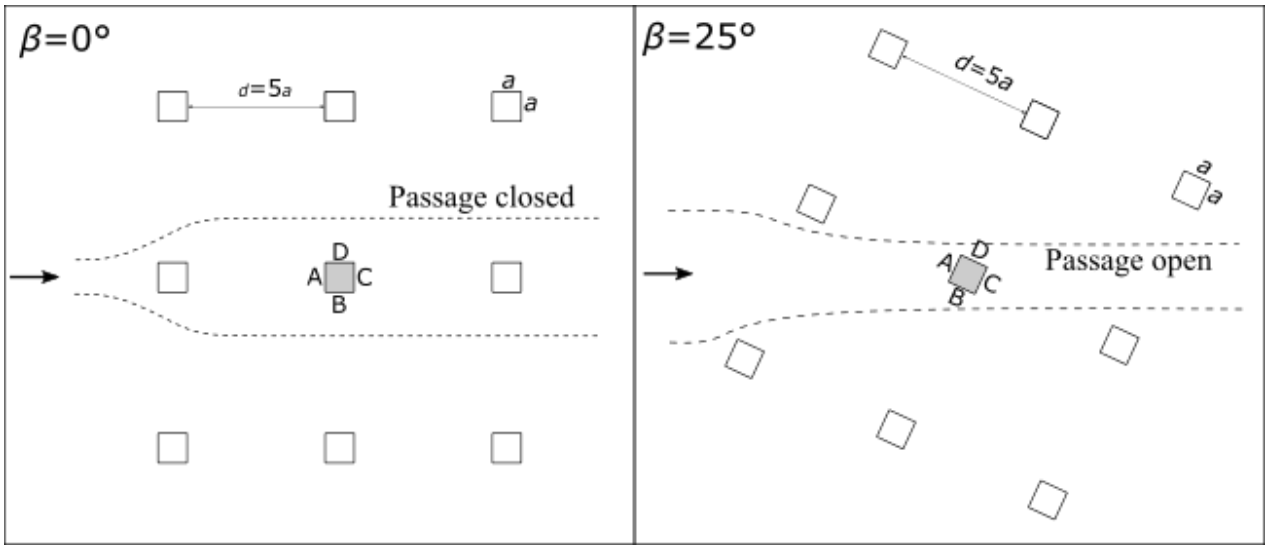

Figure 4.10 Open and closed passages between the dummies

Figure 4.11 shows across-wind moments of the model building situated in the model urban neighbourhood at various wind incidence angles. Due to the symmetry of the experimental setup, the across-wind moments at 0° and 45° were expected to be zero. However, in practice, even the slightest asymmetry in the setup leads to some small across-wind moments. Therefore, when a setup consists of 9 models, it is unrealistic to expect that the geometric symmetry of the setup will be perfectly achieved. The reason why the results for $\beta = 45°$ are higher than for the for $\beta = 0°$ is because $\beta = 45°$ is the most stream-lined configuration and an asymmetry has a more significant impact on the results than at $\beta = 0°$. The peak value of the across-wind moment coefficient is at 30° for case 1 (building model without porous screen), and between 30° and 35° for case 2 and case 3 (25% and 50% porosity screens). There is no apparent difference between the results at various porosities, but there is an effect of decreasing values when adding a porous screen. The largest difference in values is observed at angles with the most spacious airflow passage, i.e. between 15° and 30°, Figure

4.10. This phenomenon may be due to an increased surface roughness of buildings equipped with a DSF system.

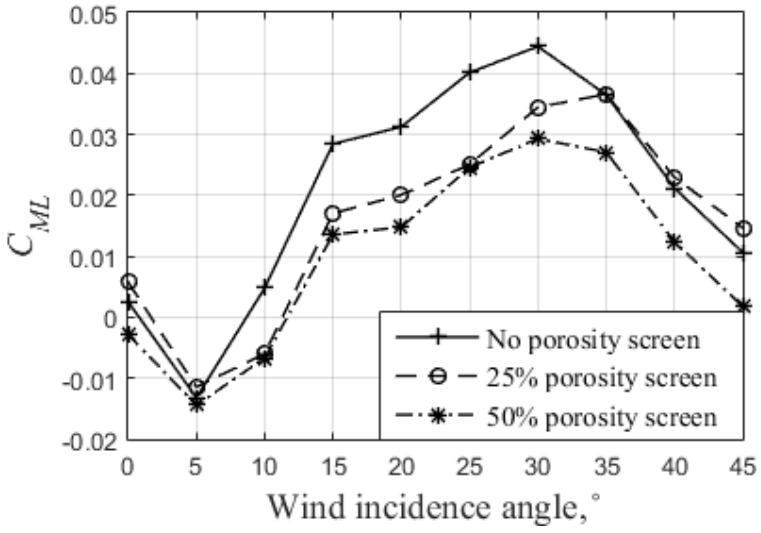

Figure 4.11 Across-wind moment coefficients for the model building situated in the model urban neighbourhood ($d = 5a$)

Figure 4.12 shows the non-dimensional power spectral density of along-wind moments. To normalize the power spectra, it was multiplied by the frequency and divided by the variance. At the same time, normalization of the frequency was conducted by multiplying it with the model building height and dividing it with the mean free-stream velocity. Since there is a constant overlap of the values at all wind incidence angles, there is no apparent effect of the PDSF application. The across-wind vibrations are concentrated around one particular frequency, which is observed as more pronounced peaks, Figure 4.13.

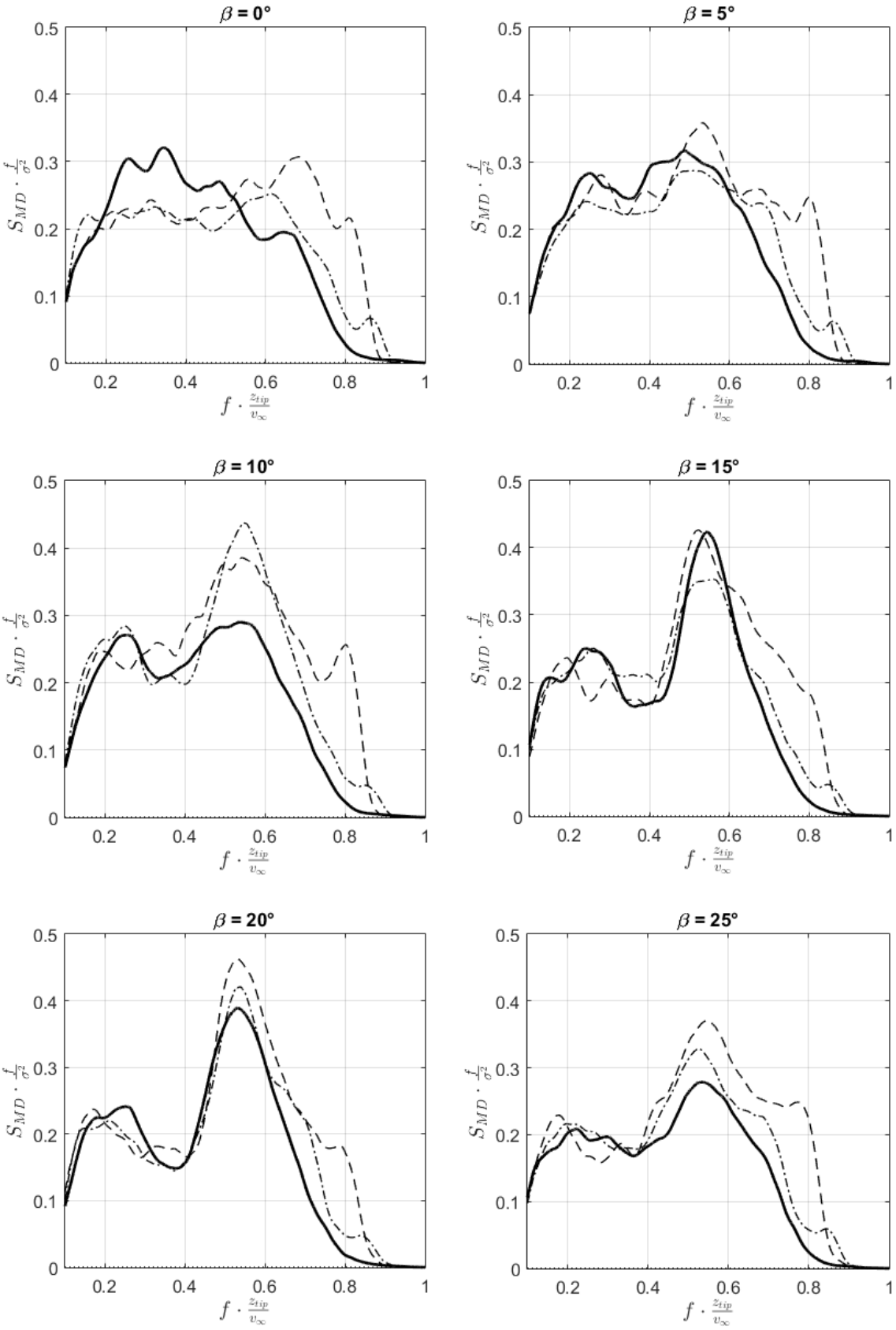
β = 0°
β = 5°
β = 10°
β = 15°
β = 20°
β = 25°
$S_{MD} \cdot \frac{f}{\sigma^2}$
$f \cdot \frac{z_{tip}}{v_\infty}$
0
0.1
0.2
0.3
0.4
0.5
0.6
0.8
1

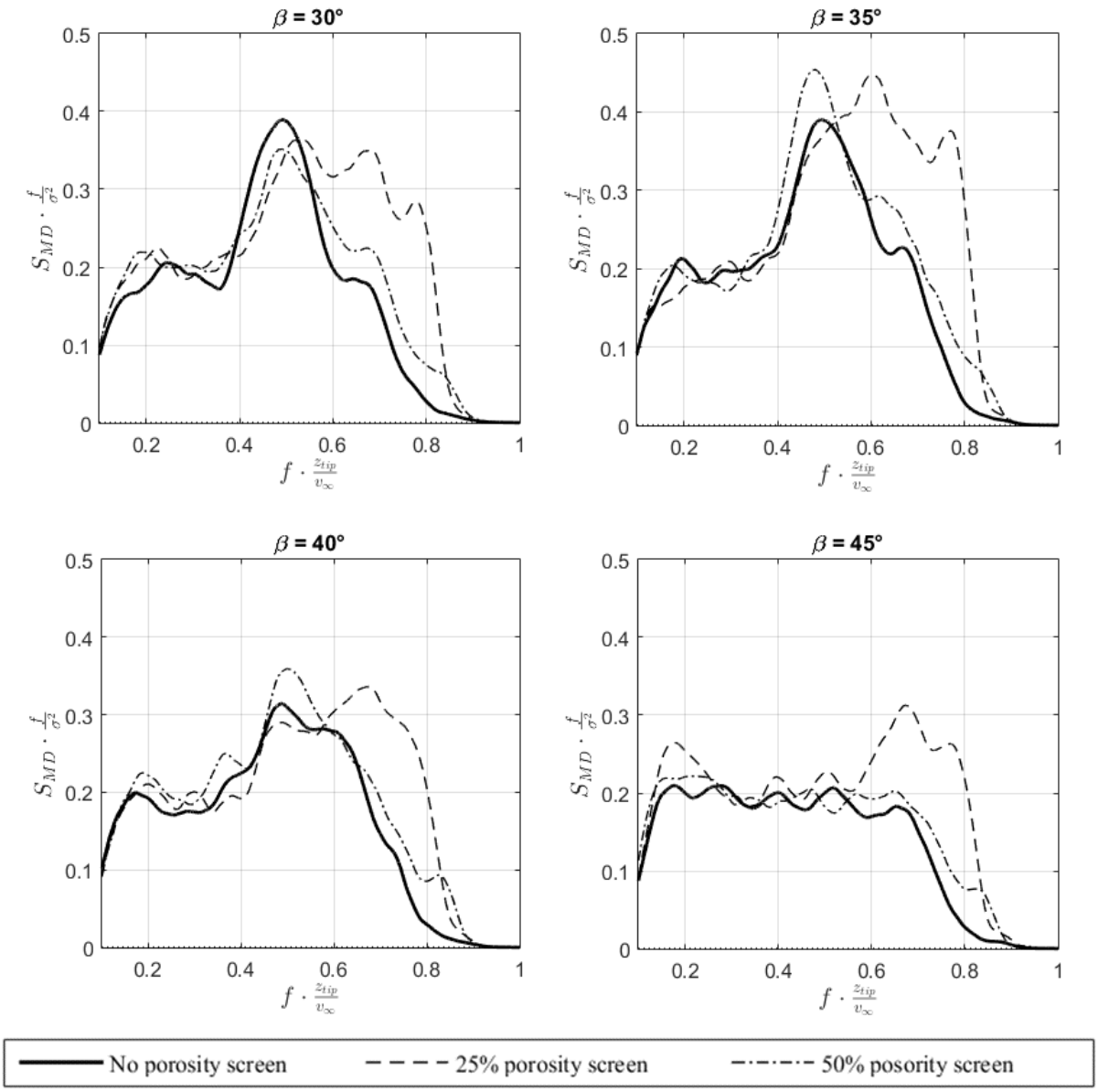

Figure 4.12 Along-wind moment power spectra for the studied model building situated in the model urban neighbourhood ($d = 5a$)

Across-wind moment power spectra are shown in Figure 4.13. The results at low wind incidence angles are slightly higher compared to the results obtained at larger wind incidence angles. The reason lies in the vortex-induced vibrations that are most pronounced at low wind incidence angles. It may be observed that the peak values of the power spectra change negligibly concerning the wind incidence angle variations. This phenomenon is attributed to dummy model buildings situated upwind of the studied model building, a setup that causes an increase in turbulence impinging on the studied model building. Thus, the studied model building is already in the wake of the dummy building models, a flow range characterized by

strong vortices causing lateral vibrations. Higher peak values are observed for the studied model building equipped with the PDSF system, a trend observed at almost all wind incidence angles. Based on this analysis, it can be concluded that the use of the PDSF systems in an urban environment yields larger vibrations of the studied model building.

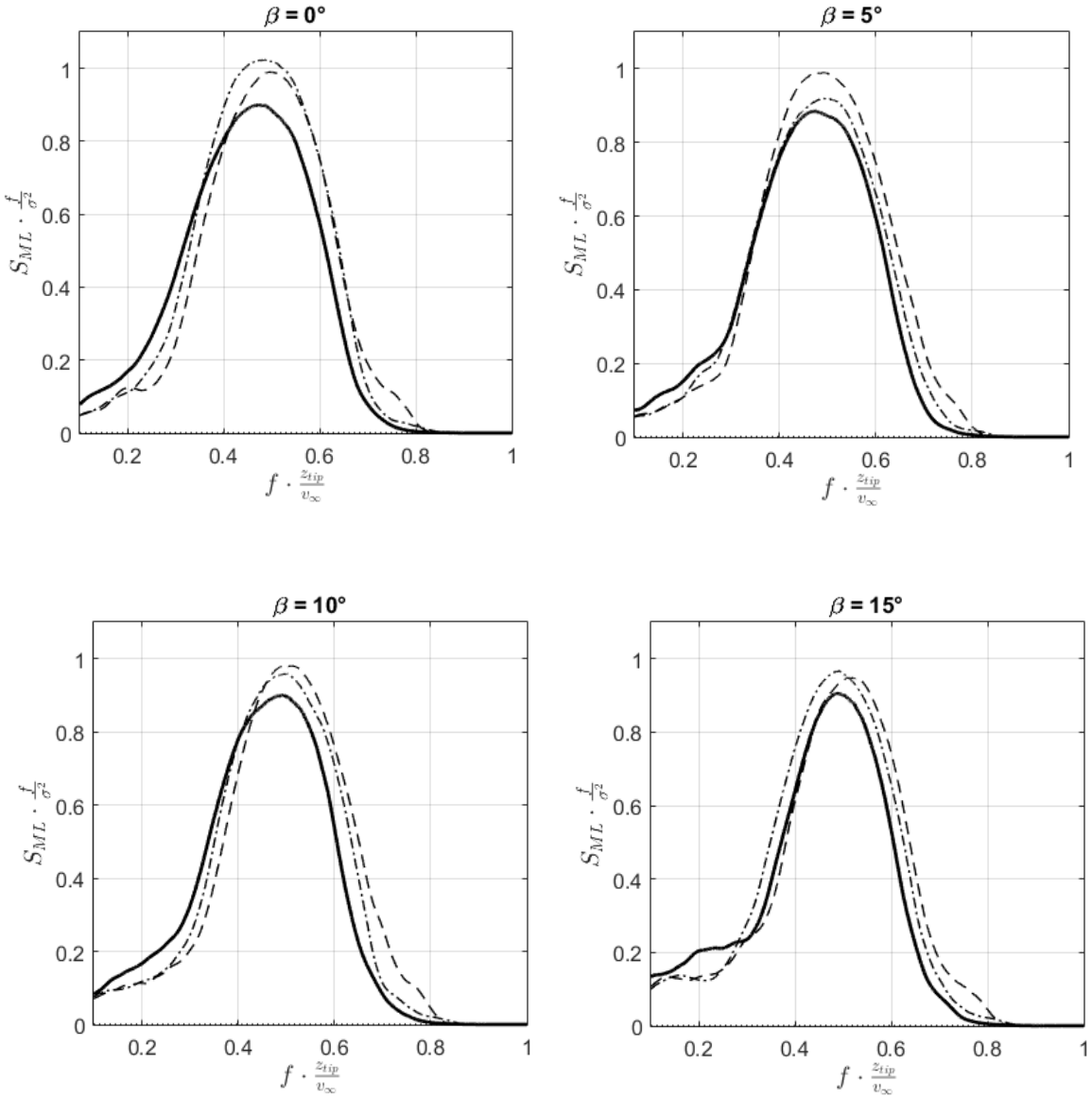

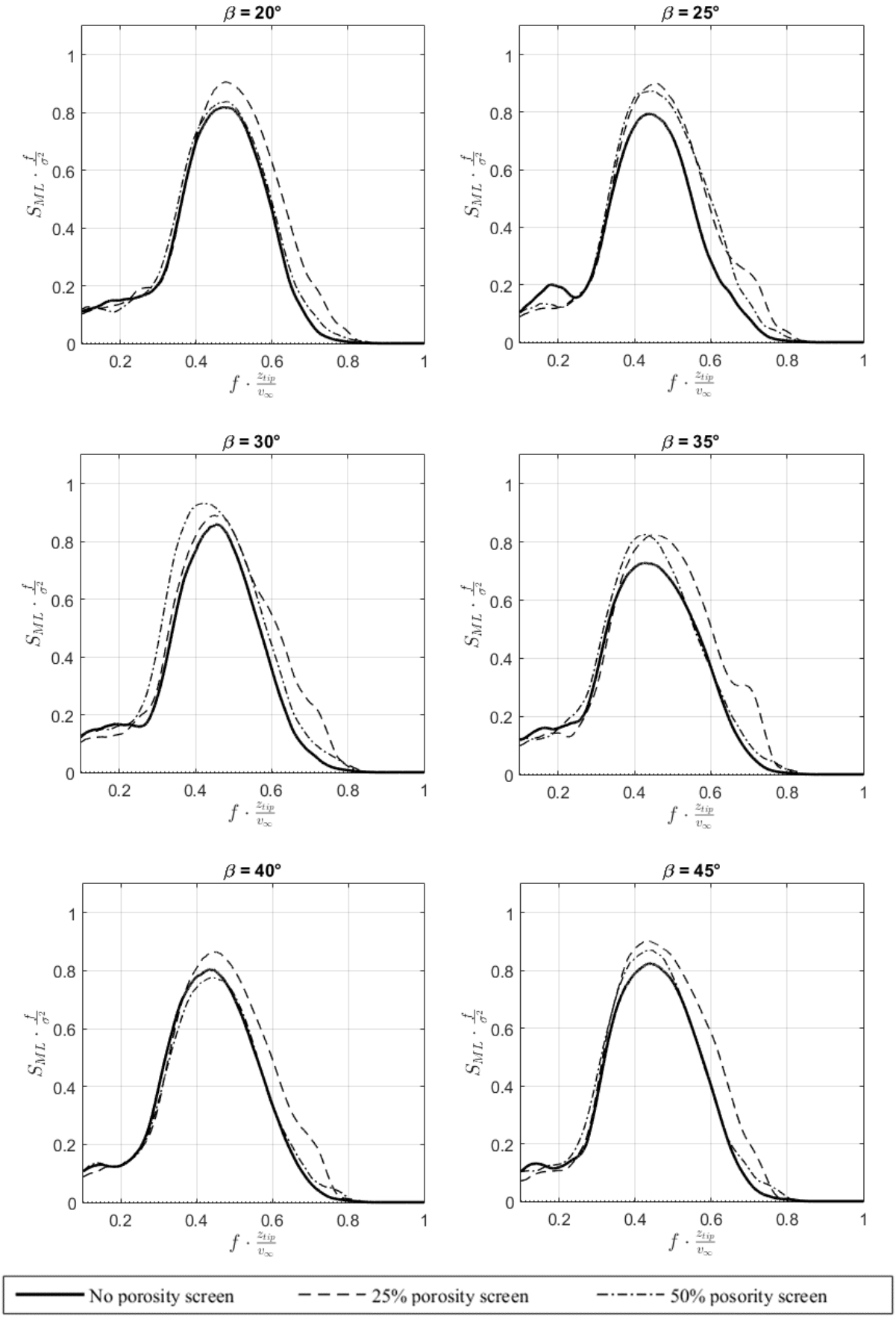
β = 20°
β = 25°
β = 30°
β = 35°
β = 40°
β = 45°
$S_{ML} \cdot \frac{f}{\sigma^2}$
$f \cdot \frac{z_{tip}}{v_\infty}$
No porosity screen
25% porosity screen
50% posority screen

Figure 4.13 Across-wind moment power spectra for the studied model building situated in the model urban neighbourhood ($d = 5a$)

Second set of experiments

This set of experiments focuses on the effects of various spacings between the model buildings in the model urban environment. Two configurations of the studied model building were analyzed, i.e., a) a single-skin façade model building and b) a double-skin façade model building equipped with an outer porous façade of 25% porosity. Only at the small spacing of model buildings, the DSF system was not tested because it was estimated that the studied model building was entirely sheltered, and it was anticipated that the installation of a porous façade would not have any impact on the results. As a matter of fact, the large sheltering of the studied model building causes a decreased wind load on the studied model building, so at some point, the experimental equipment is no longer reliable.

Figure 4.14 shows the along-wind moment coefficient dependence on the wind incidence angle for the studied model building situated in the model urban neighbourhood. There is an apparent offset in results considering various spacing of model buildings. Increasing the distance between model buildings yields an increase in the along-wind moment coefficient. On the other hand, overlapping of the single-skin façade and PDSF results indicates a negligible difference in the along-wind moment coefficient when using a PDSF system. From the results for a small spacing density ($d = a$), it can be observed that at $0°$ the along-wind moment coefficient is $C_{MD} \approx 0$ which indicates the fact that the studied model building was completely sheltered from the wind. For the medium ($d = 3a$) and large ($d = 5a$) spacing, the maximum along-wind moment coefficient was achieved at $\beta = 25°$, which is attributed to the characteristic wind flow between model buildings, Figure 4.10. The consequence is that the maximum value of C_{MD} is achieved for $\beta = 45°$ when the models are in the most streamlined configuration, and some flow enters the passages between model buildings.

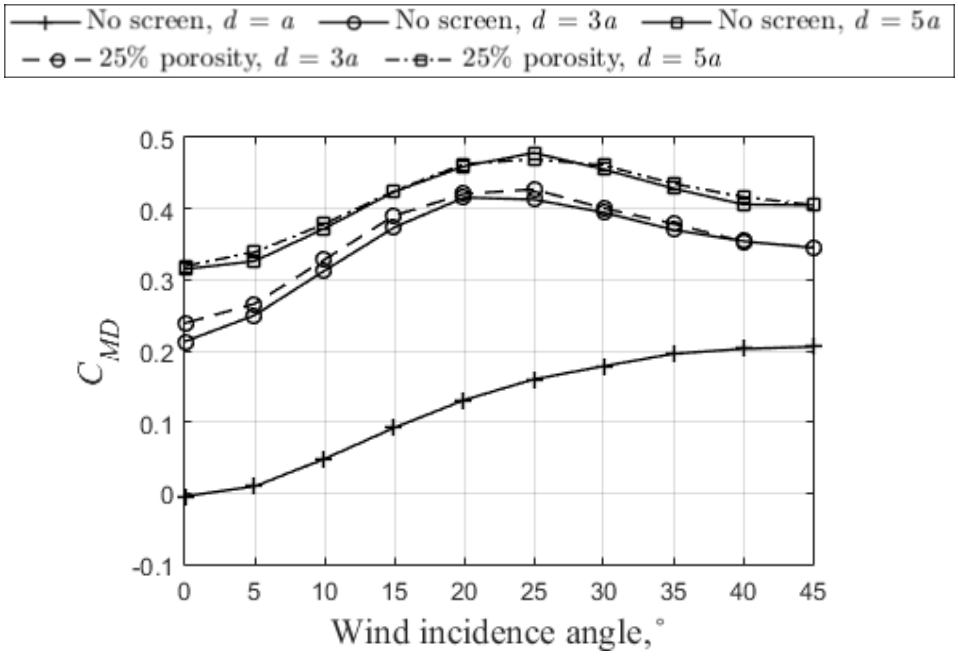

Figure 4.14 Along-wind moment coefficients for the studied model building situated in the model urban neighbourhood ($d = a$, $d = 3a$, $d = 5a$)

The across-wind moment coefficients of the studied model building situated in various model urban neighbourhoods are shown in Figure 4.15. The maximum absolute result is observed at the small spacing ($d = a$) at $\beta = 20°$, while the second largest value is at the large spacing ($d = 5a$) at $\beta = 30°$, the result that indicates that the spacing between model buildings has a negligible effect on the across-wind moment coefficients. There is no clear trend in the results values when using the DSF system at the medium spacing ($d = 3a$). Given these results, there is no improvement in the studied model building aerodynamics when using DSFs on buildings in urban environments, but there are also no adverse effects.

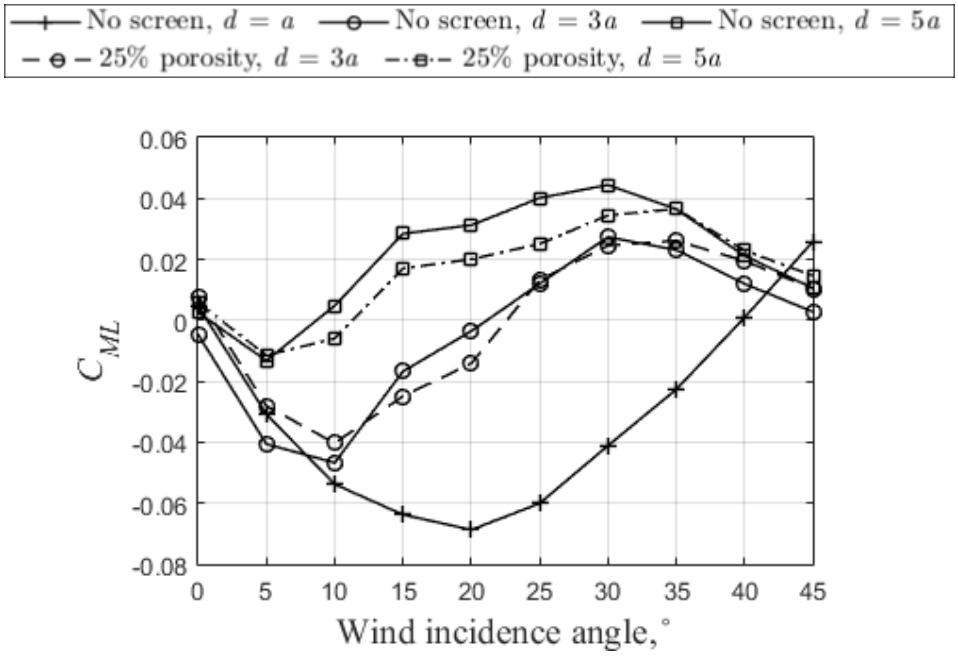

Figure 4.15 Across-wind moment coefficients for the studied model building situated in the model urban neighbourhood ($d = a$, $d = 3a$, $d = 5a$)

Figure 4.16 shows the along-wind moment power spectra coefficients for various spacings between model buildings. The peaks at the medium spacing of model buildings are from 30° to 40°. Almost the same peak is observed at 45° for small and medium spacing of model buildings. Given these ambiguous results, it is impossible to make clear conclusions about the effect of spacing of model buildings on the along-wind power spectra on the studied model building.

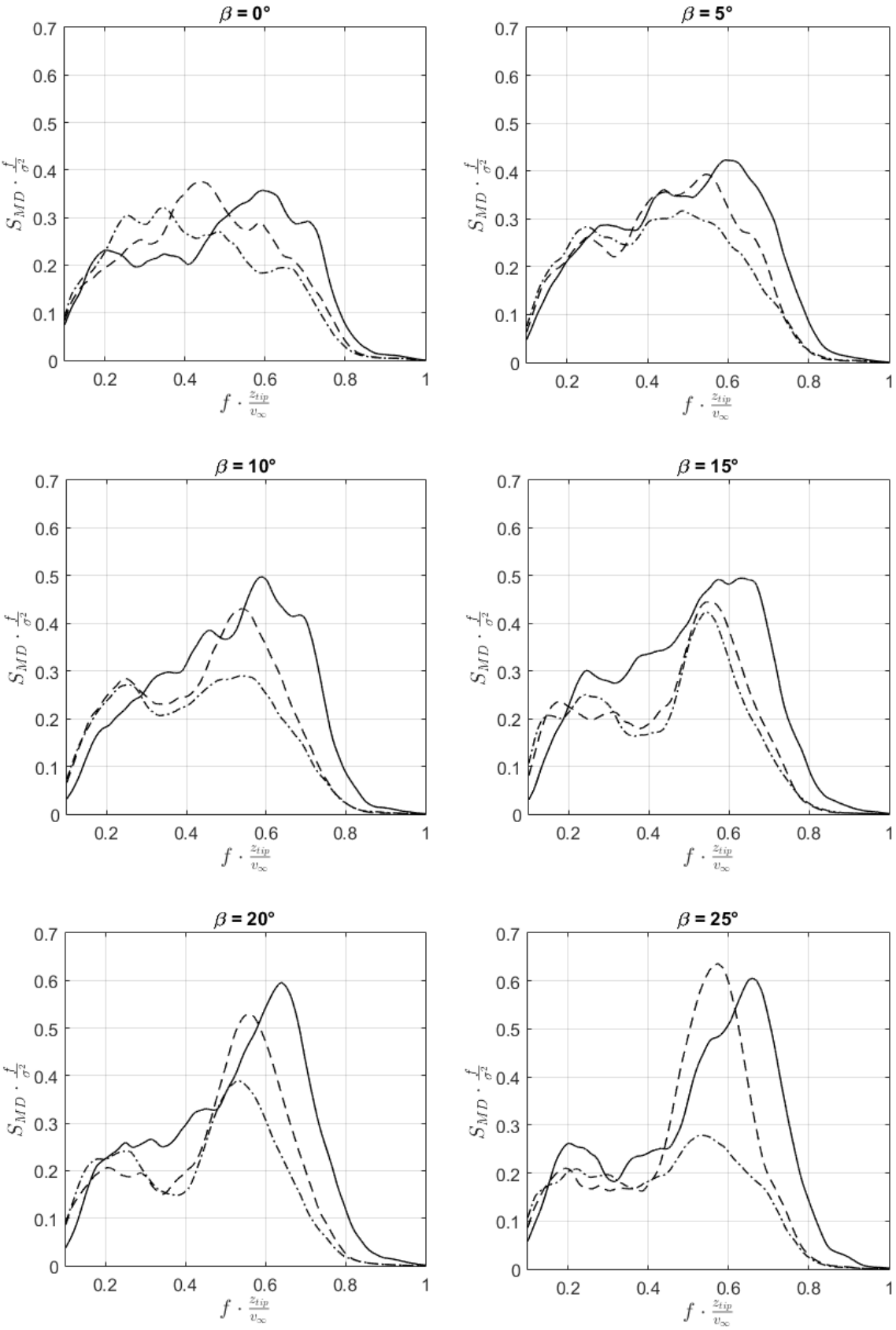
β = 0°
β = 5°
β = 10°
β = 15°
β = 20°
β = 25°
$S_{MD} \cdot \frac{f}{\sigma^2}$
$f \cdot \frac{z_{tip}}{v_\infty}$

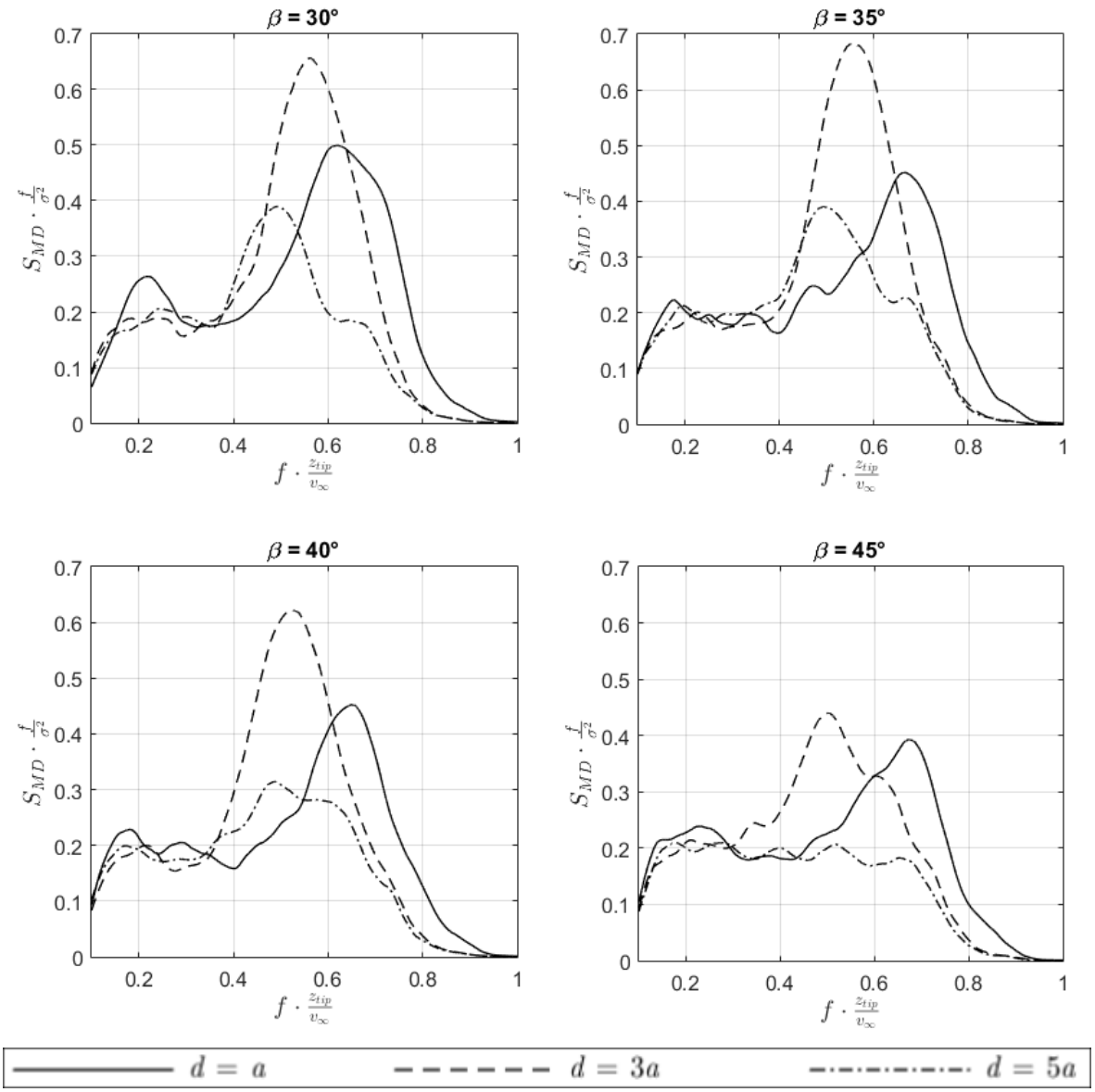

Figure 4.16 Along-wind moment power spectra for the studied model building situated in the model urban neighbourhood ($d = a$, $d = 3a$, $d = 5a$)

Figure 4.17 shows the across-wind moment power spectra of the studied model building situated in various model urban neighbourhoods. The maximum peaks for all spacings of model buildings are observed at wind incidence angles between 15° and 25°. In that range of wind incidence angles, the smaller spacing between model buildings, the larger peak magnitude, while the peaks and the shape of the curves for the medium and large spacings are similar. In general, the spacing between model buildings does not appear to substantially affect the across-wind moment power spectra.

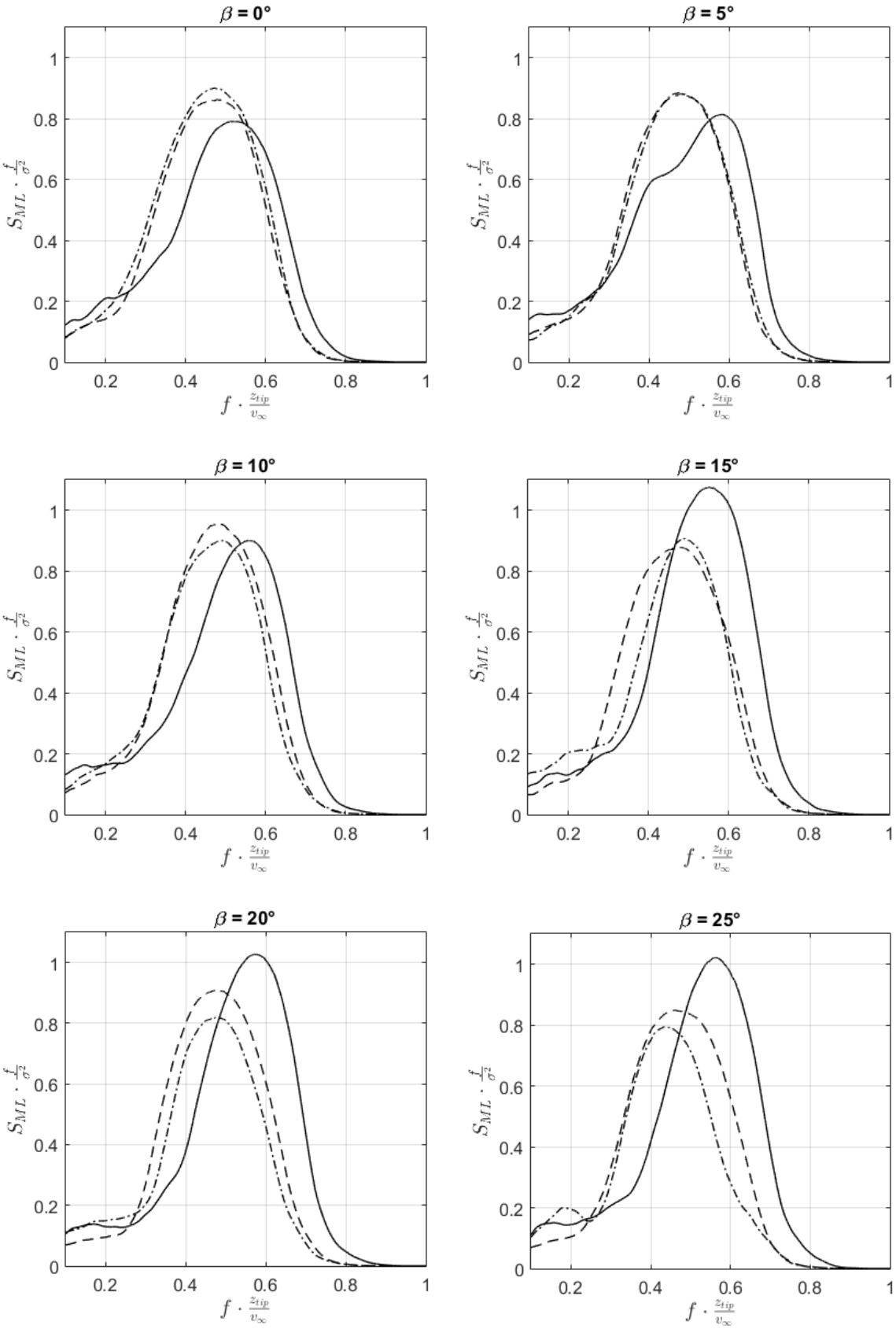
β = 0°
β = 5°
β = 10°
β = 15°
β = 20°
β = 25°
$S_{ML} \cdot \frac{f}{\sigma^2}$
$f \cdot \frac{z_{tip}}{v_\infty}$
0
0.2
0.4
0.6
0.8
1

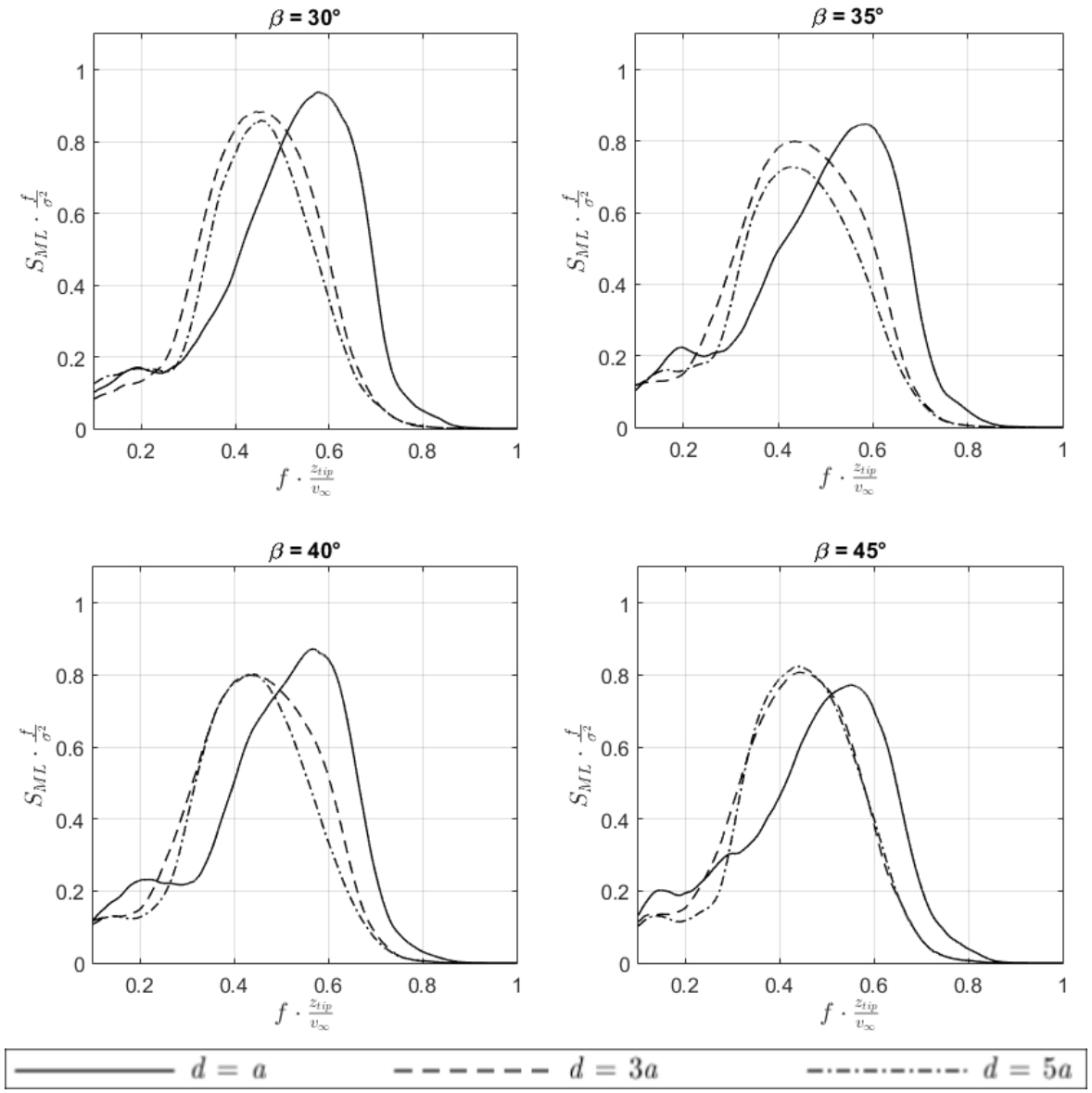

Figure 4.17 Across-wind moment power spectra for the studied model building situated in the model urban neighbourhood ($d = a$, $d = 3a$, $d = 5a$)

4.4 Surface pressure on the studied building model

Pressure distributions are created by two-dimensional linear interpolation of the data measured by pressure taps, Figure 3.6. There is an exact measured value of the mean pressure coefficient on each pressure tap location, while everywhere else on pressure maps, the data were interpolated. Since there are no pressure taps on the very edge of each model building surface, there are no exact values for interpolation in this surface range, causing the interpolation errors on the edges of the model. Orientation of the experimental setup concerning the wind incidence angle is shown in Figure 3.17.

First set of experiments

Mean pressure coefficient distribution $\overline{C_p}$ for the first set of experiments is shown in Figure 4.18. The configuration without the porous screen is on the left-hand side of each row. In the middle of each row is the configuration with the 50% porous DSF system, and on the right-hand side is the configuration with the 25% porous DSF system. The plots are arranged in that order, so the inner façade most exposed to the incoming flow is on the right- and the most sheltered on the left-hand side of the figure.

Observing the 0° flow incidence angle, it can be observed that the implementation of the PDSF system alters the shape of the mean pressure coefficient distribution. The change is most apparent for surface A where it can be seen that the contours for each screen configuration have a different shape. When observing the figure from the left- to the right-hand side, the mean pressure coefficients at the entire surface gradually decrease, indicating that the PDSF system decreases the mean pressure coefficient at the entire surface. The $\overline{C_p}$ values are decreased by 10% to 20% depending on the surface and the wind incidence angle.

The flow detaches from the edges of surface A, thus creating a large separation region around the model building. Surfaces B and D, which are inside this zone, are characterized by suction. The suction peak is on the surface edge closer to the detachment point and gradually decreases in the downwind direction. The implementation of the PDSF system causes a decrease in $\overline{C_p}$. The pressure distribution on surfaces B and D are symmetric at 0° flow incidence angle, which confirms the symmetry of the setup.

Surface C (leeward surface) is characterized by suction. Since the $\overline{C_p}$ values on these entire surface are low and do not vary much, there is no apparent effect of the PDSF system on the surface pressure distribution on the leeward surface.

The findings made at the 0° flow incidence angle can also be generally observed at 15°, 30°, and 45° wind incidence angles. This clearly indicates that the mean pressure coefficients at the entire model building surface decrease when a PDSF system is used.

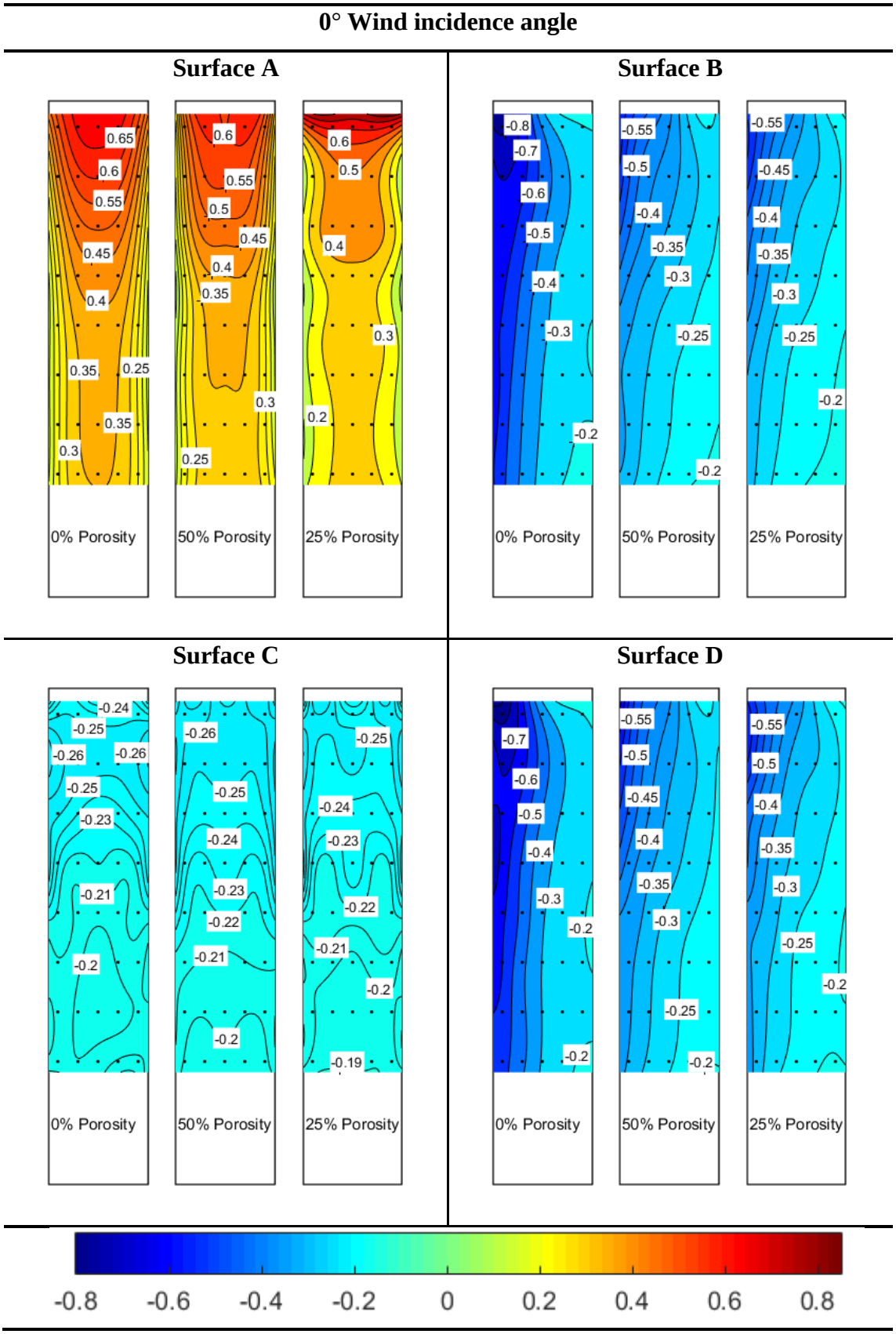
0° Wind incidence angle
Surface A
0.65
0.6
0.55
0.5
0.45
0.4
0.35
0.25
0.3
0% Porosity
50% Porosity
25% Porosity
Surface B
-0.8
-0.7
-0.6
-0.5
-0.4
-0.3
-0.2
-0.55
-0.45
-0.35
-0.25
0% Porosity
50% Porosity
25% Porosity
Surface C
-0.24
-0.25
-0.26
-0.23
-0.21
-0.22
-0.19
0% Porosity
50% Porosity
25% Porosity
Surface D
0% Porosity
50% Porosity
25% Porosity
-0.8 -0.6 -0.4 -0.2 0 0.2 0.4 0.6 0.8

15° Wind incidence angle

Surface A

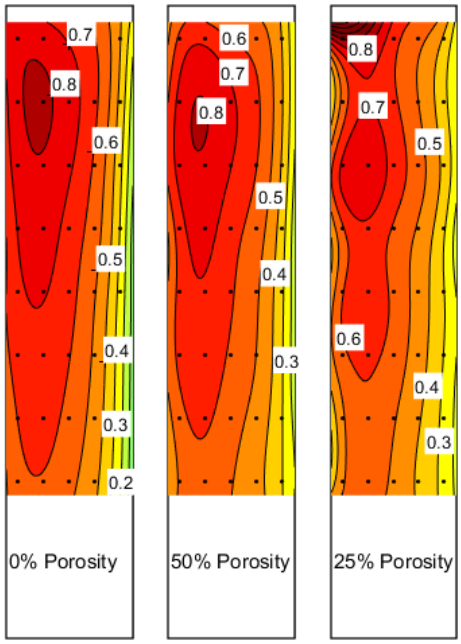

Surface B

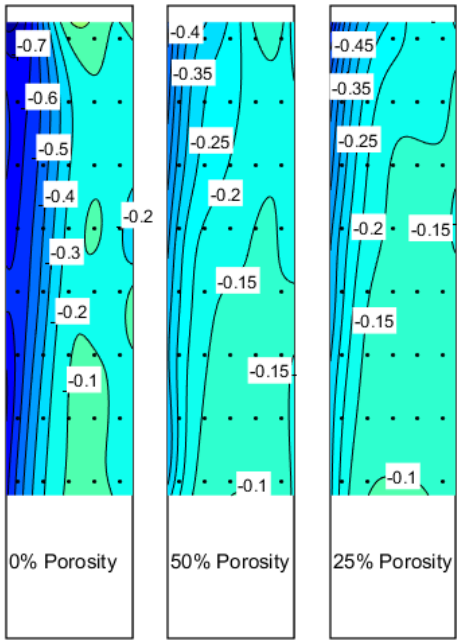

Surface C

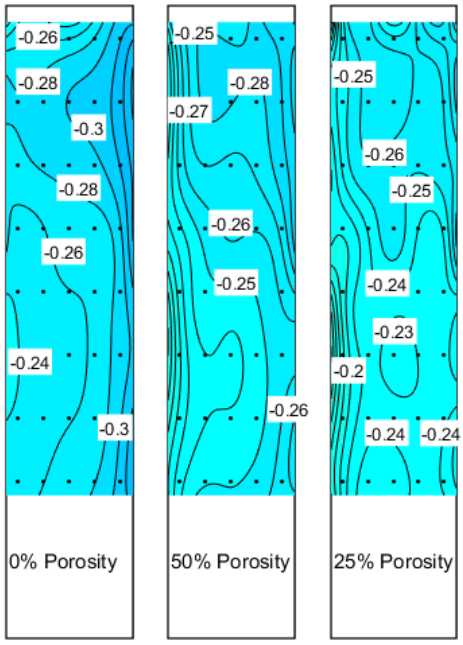

Surface D

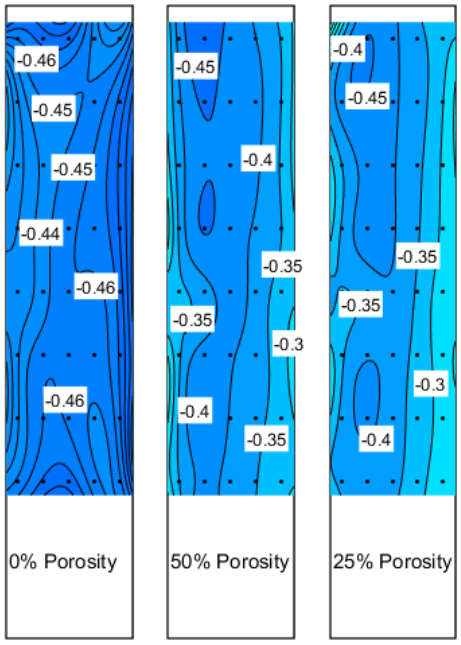

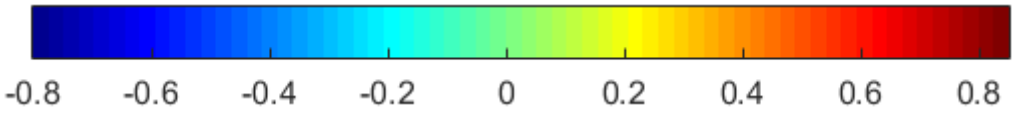

30° Wind incidence angle

Surface A

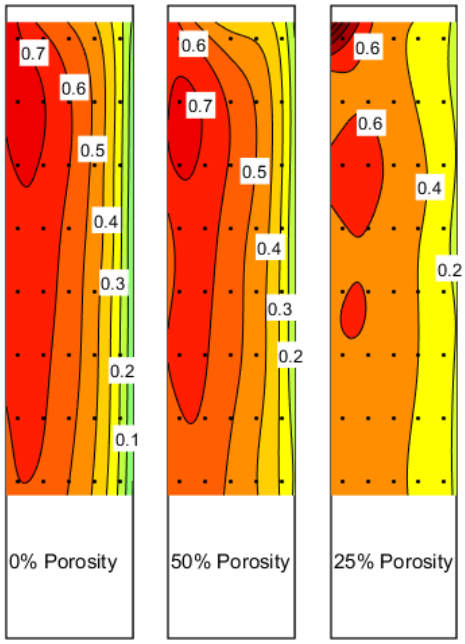

Surface B

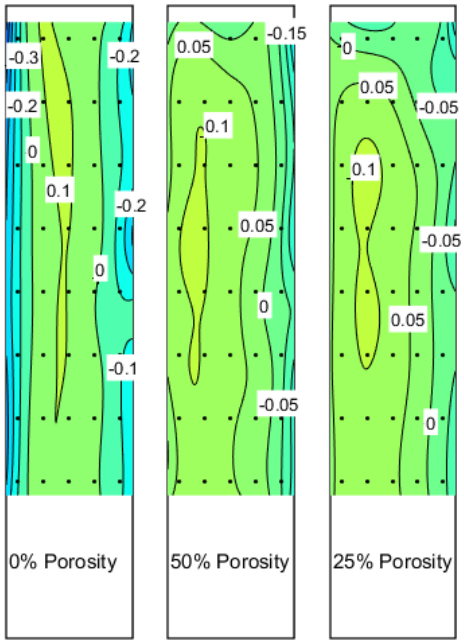

Surface C

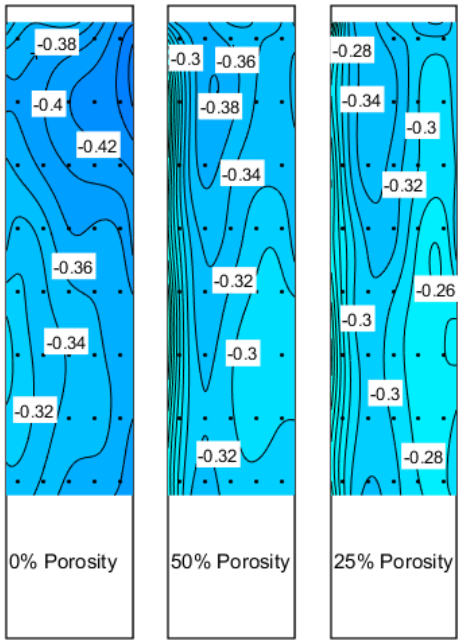

Surface D

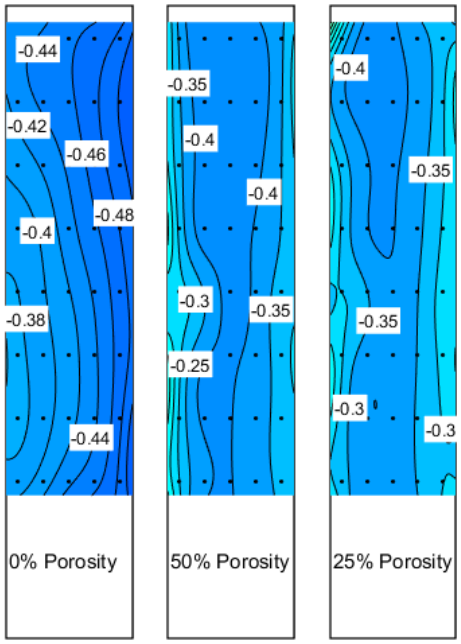

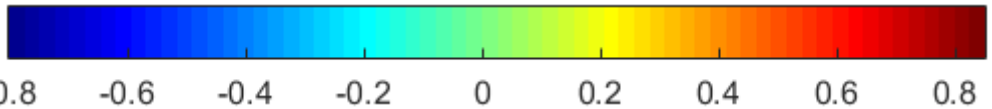

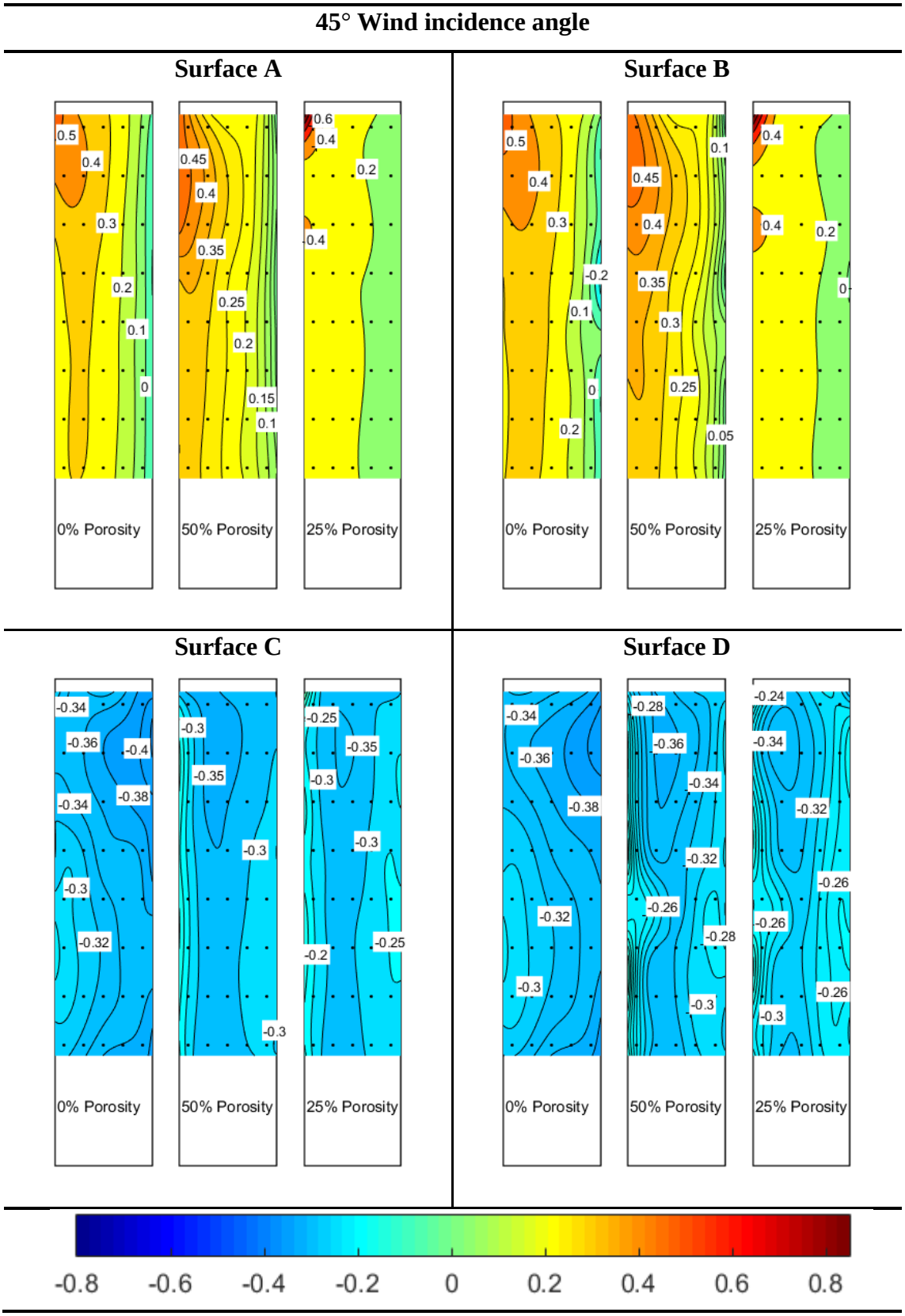

Figure 4.18 Mean pressure coefficient distribution ($\overline{C_p}$) in the first set of experiments

The standard deviation of the surface pressure coefficient is predominantly influenced by turbulence in the flow. Figure 4.19 shows the pressure distribution in the first set of experiments.

At the 0° wind incidence angle, on the lower 70% of the surface A, the standard deviation σ of the C_p remains nearly constant. With increasing height, σ increases towards the upper edge of the model building surface. The turbulence increase in the upper part of the surface is due to the interaction of the detached flow from the top edge of the building and the free-stream flow. The effect of the PDSF system on surface pressure distribution on surface A is negligible. On the other hand, the effect of the DSF system on surfaces B and D is substantial. In particular, the PDSF system creates the inner flow between two façades. The inner flow is sheltered from the outer, detached, highly turbulent flow. Thus, σ of C_p on the inner façade are considerably reduced. The most considerable difference is near the vertical edge closer to surface A. At that point, the flow separates, thus creating the highly turbulent recirculating bubble, which is observed on the single-skin façade configuration. In contrast, turbulence is substantially lower on the configurations equipped with the DSF system due to the sheltered inner flow. Surface C is entirely in the wake, thus characterized by low and nearly constant σ of C_p over the entire model building surface.

In general, the implementation of the PDSF system yields decreased turbulence in front of the inner model building surfaces. The inner façade is sheltered from the highly turbulent free-stream flow. This trend may be observed at all wind incidence angles.

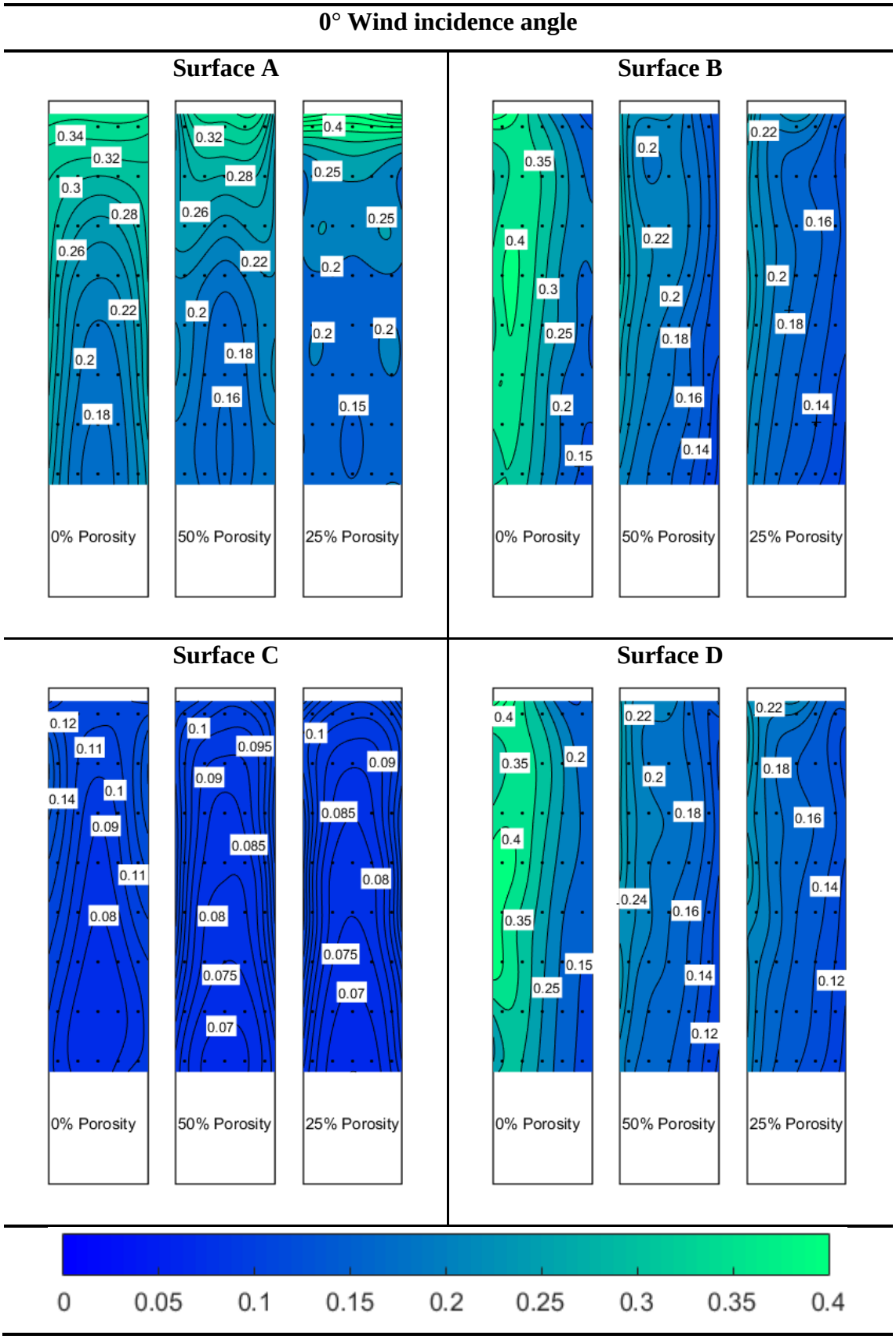
0° Wind incidence angle
Surface A
0.34
0.32
0.3
0.28
0.26
0.22
0.2
0.18
0% Porosity
0.32
0.28
0.26
0.22
0.2
0.18
0.16
50% Porosity
0.4
0.25
0.25
0.2
0.2
0.2
0.15
25% Porosity
Surface B
0.35
0.4
0.3
0.25
0.2
0.15
0% Porosity
0.2
0.22
0.2
0.18
0.16
0.14
50% Porosity
0.22
0.16
0.2
0.18
0.14
25% Porosity
Surface C
0.12
0.11
0.14
0.1
0.09
0.11
0.08
0% Porosity
0.1
0.095
0.09
0.085
0.08
0.075
0.07
50% Porosity
0.1
0.09
0.085
0.08
0.075
0.07
25% Porosity
Surface D
0.4
0.35
0.2
0.4
0.35
0.25
0.15
0% Porosity
0.22
0.2
0.18
0.24
0.16
0.14
0.12
50% Porosity
0.22
0.18
0.16
0.14
0.12
25% Porosity
0
0.05
0.1
0.15
0.2
0.25
0.3
0.35
0.4

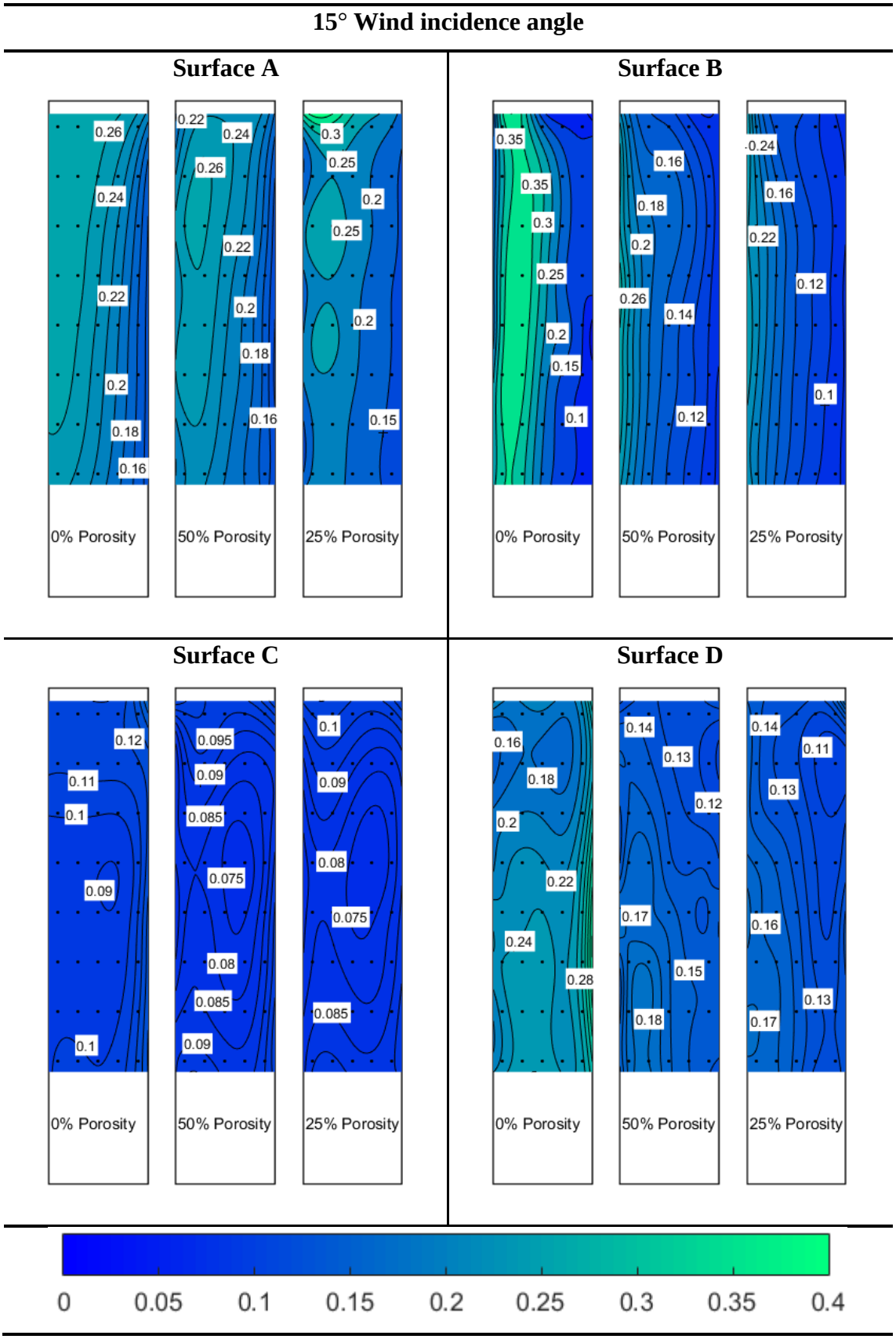
15° Wind incidence angle
Surface A
0.26
0.24
0.22
0.2
0.18
0.16
0% Porosity
0.22
0.24
0.26
0.22
0.2
0.18
0.16
50% Porosity
0.3
0.25
0.2
0.25
0.2
0.15
25% Porosity
Surface B
0.35
0.35
0.3
0.25
0.2
0.15
0.1
0% Porosity
0.16
0.18
0.2
0.26
0.14
0.12
50% Porosity
0.24
0.16
0.22
0.12
0.1
25% Porosity
Surface C
0.12
0.11
0.1
0.09
0.1
0% Porosity
0.095
0.09
0.085
0.075
0.08
0.085
0.09
50% Porosity
0.1
0.09
0.08
0.075
0.085
25% Porosity
Surface D
0.16
0.18
0.2
0.22
0.24
0.28
0% Porosity
0.14
0.13
0.12
0.17
0.15
0.18
50% Porosity
0.14
0.11
0.13
0.16
0.13
0.17
25% Porosity
0
0.05
0.1
0.15
0.2
0.25
0.3
0.35
0.4

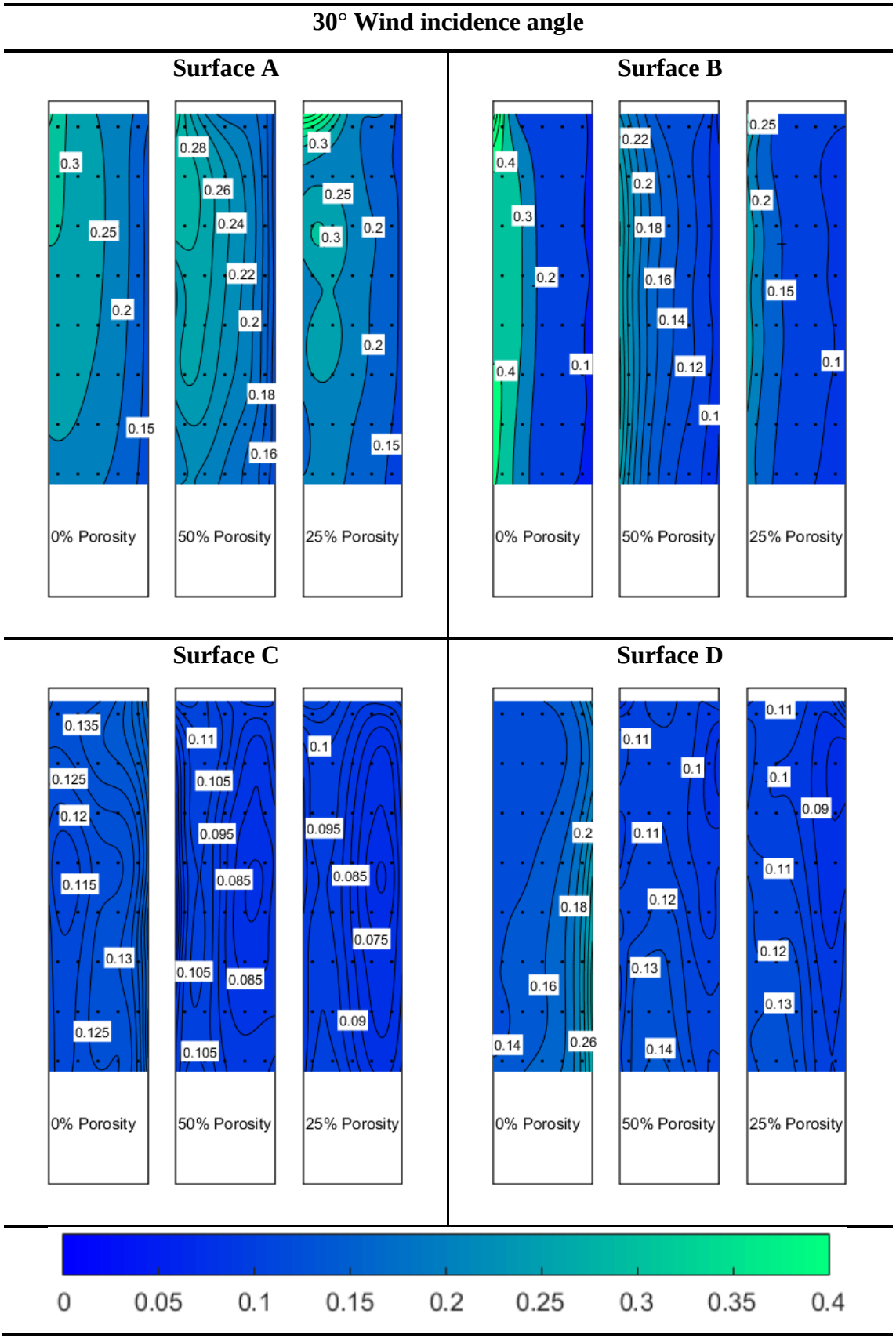
30° Wind incidence angle
Surface A
0.3
0.25
0.2
0.15
0% Porosity
0.28
0.26
0.24
0.22
0.2
0.18
0.16
50% Porosity
0.3
0.25
0.2
0.3
0.2
0.15
25% Porosity
Surface B
0.4
0.3
0.2
0.4
0.1
0% Porosity
0.22
0.2
0.18
0.16
0.14
0.12
0.1
50% Porosity
0.25
0.2
0.15
0.1
25% Porosity
Surface C
0.135
0.125
0.12
0.115
0.13
0.125
0% Porosity
0.11
0.105
0.095
0.085
0.105
0.085
0.105
50% Porosity
0.1
0.095
0.085
0.075
0.09
25% Porosity
Surface D
0.2
0.18
0.16
0.14
0.26
0% Porosity
0.11
0.1
0.11
0.12
0.13
0.14
50% Porosity
0.11
0.1
0.09
0.11
0.12
0.13
25% Porosity
0
0.05
0.1
0.15
0.2
0.25
0.3
0.35
0.4

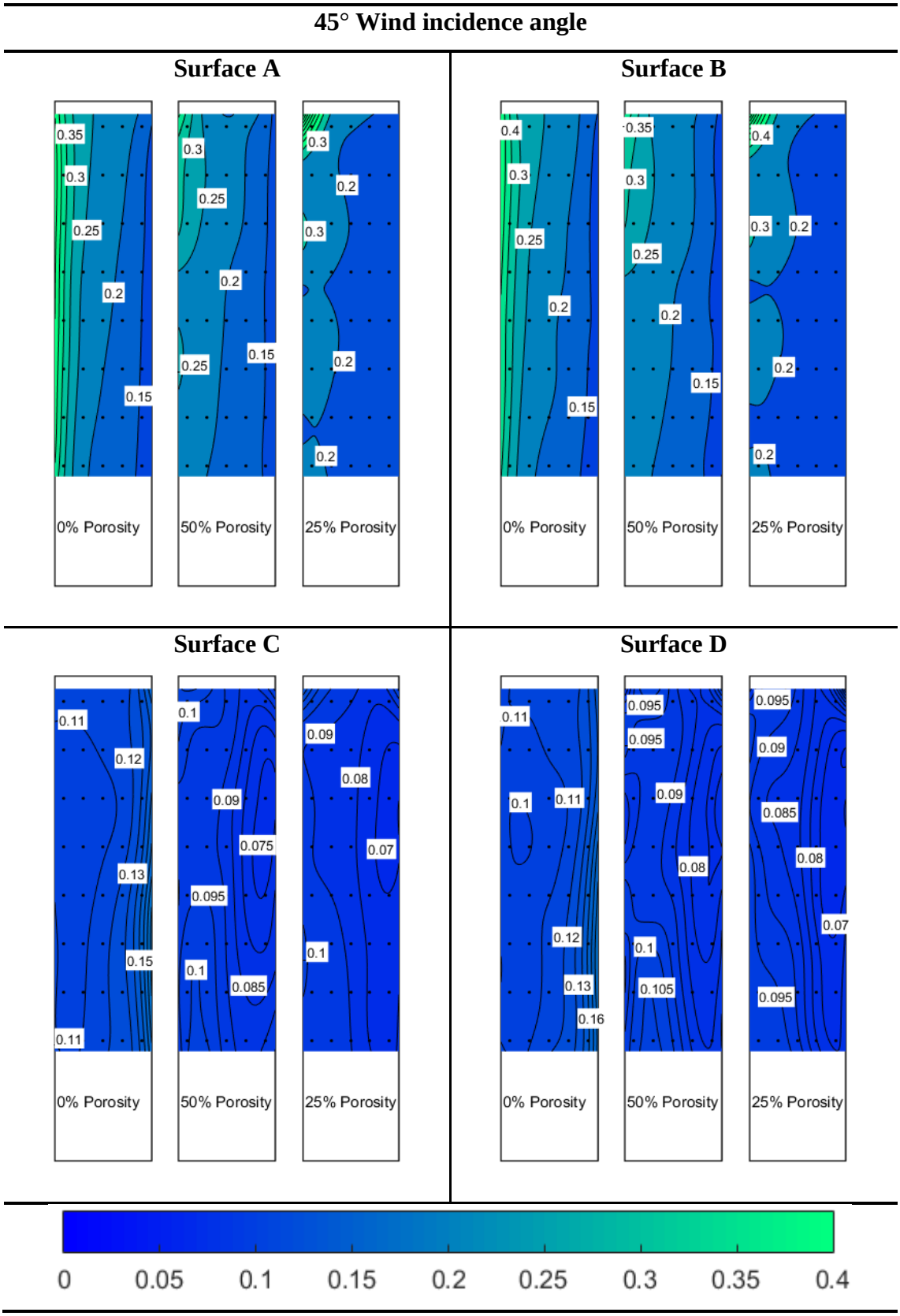

Figure 4.19 Standard deviation distribution of the pressure coefficient in the first set of experiments

Second set of experiments

Figure 4.20 and Figure 4.21 show the mean pressure coefficient distribution ($\overline{C_p}$) in the second set of experiments. The mean pressure coefficient distribution for small spacing between model buildings, when the studied model building surface is smooth, i.e., without a PDSF system, is shown in Figure 4.20, while the medium and large spacing configurations are shown in Figure 4.21.

The studied model building is in the wake of the windward dummy model building at the 0° wind incidence angle. At the 15° wind incidence angle, a narrow gap (passage) opens up, which causes flow channeling. As a result, a gust of accelerated airflow may be observed on the left-hand side of surface A at 15° and 30° wind incidence angles. At the 45° wind incidence angle, the dummy model building also entirely shelters the studied model building. However, at this wind incidence angle, the model buildings are in the most streamlined configuration, so the windward vertical edge between surfaces A and B is characterized by the positive values of the $\overline{C_p}$. In the case of small spacing between model buildings, all surfaces on the studied model building are sheltered at the entire range of wind incidence angles and are thus not analyzed at this point.

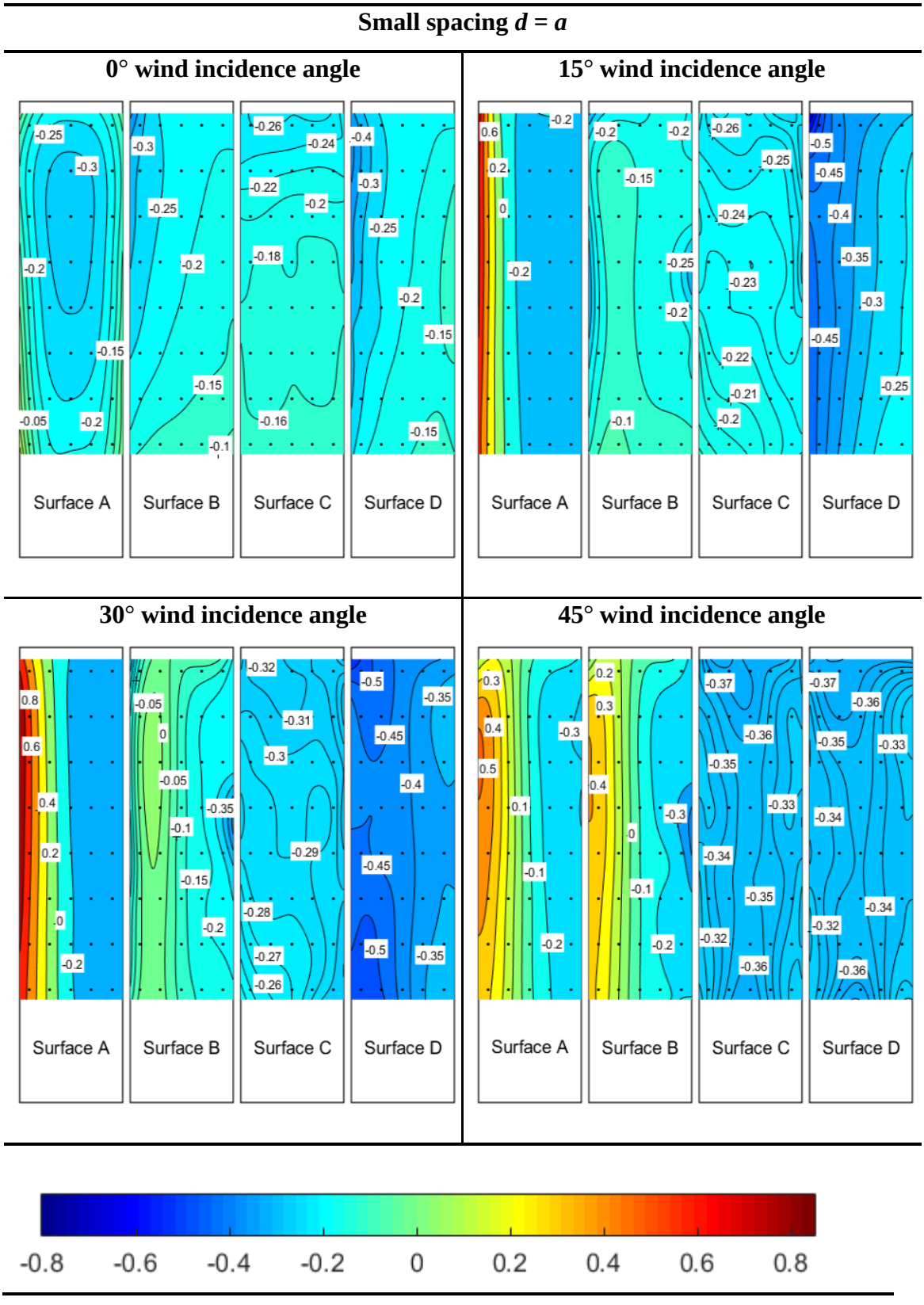

Figure 4.20 Mean pressure coefficient distribution ($\overline{C_p}$) at small spacing ($d = a$) between model buildings

By increasing the spacing between model buildings, there is more space for the flow between dummy model buildings, thus resulting in ~10% larger mean pressure coefficient magnitudes on the windward surface of the studied model building. This difference is less exhibited on other model building surfaces, i.e., the absolute peak values of the $\overline{C_p}$ at the large spacing between model buildings are 5% - 10% larger than at the medium spacing between model buildings. Implementation of the PDSF system yields a decrease in $\overline{C_p}$ of ~20% on the windward surface and on surfaces characterized by large suction (e.g., Surfaces B and D at 0°) for medium and large spacing between model buildings. On surfaces on which the mean pressure coefficient is low (e.g., Surface C at 0° and 15°), the PDSF system does not yield an obvious effect.

0° Wind incidence angle

Surface A

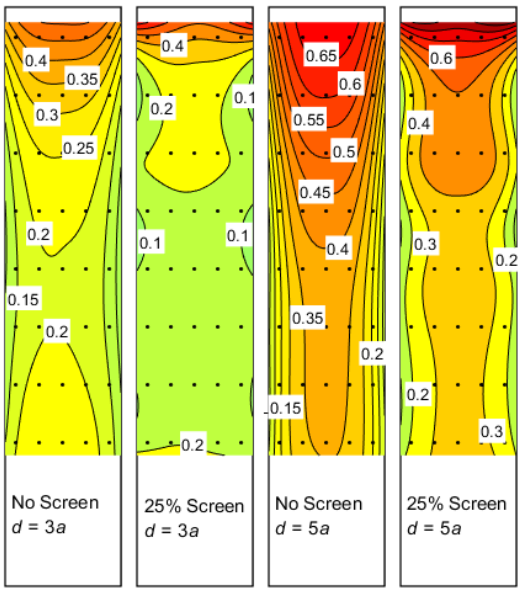

Surface B

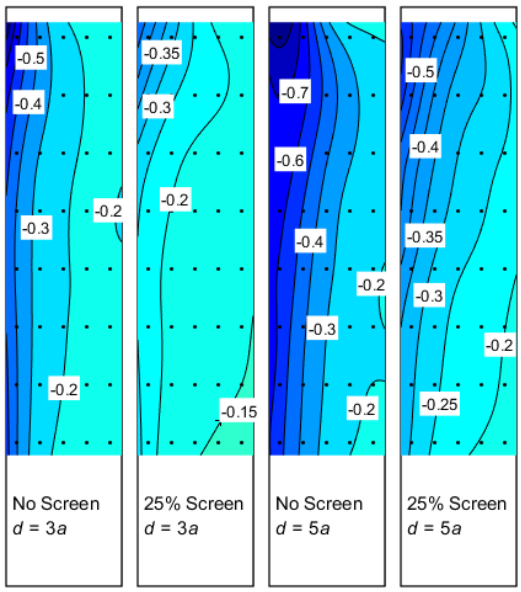

Surface C

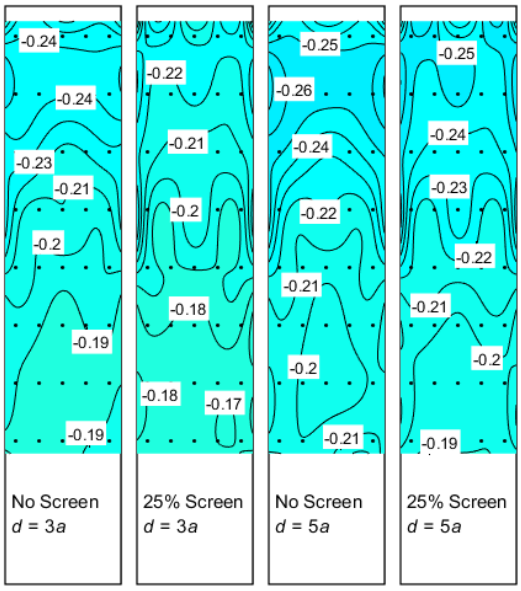

Surface D

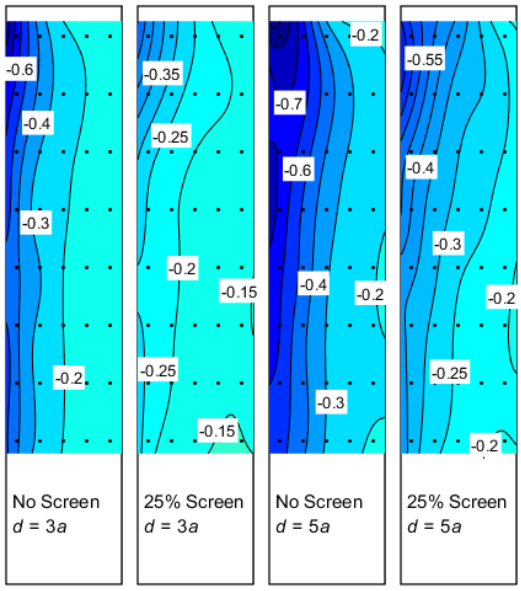

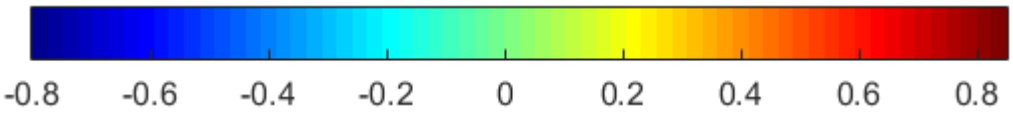

15° Wind incidence angle

Surface A

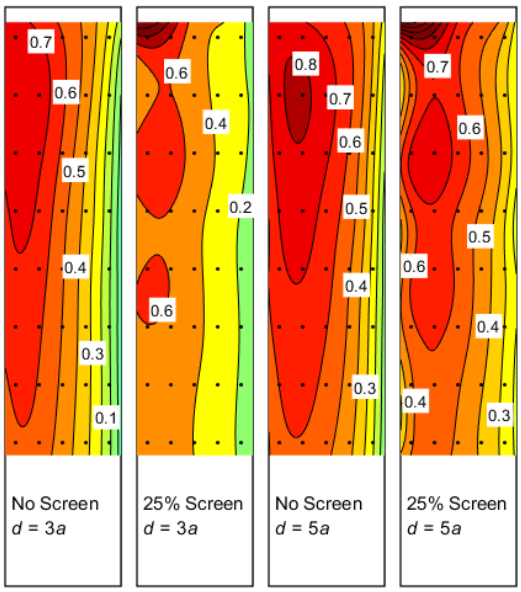

Surface B

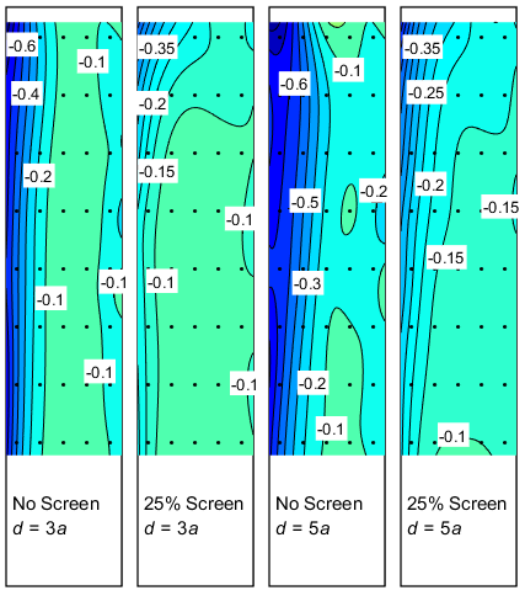

Surface C

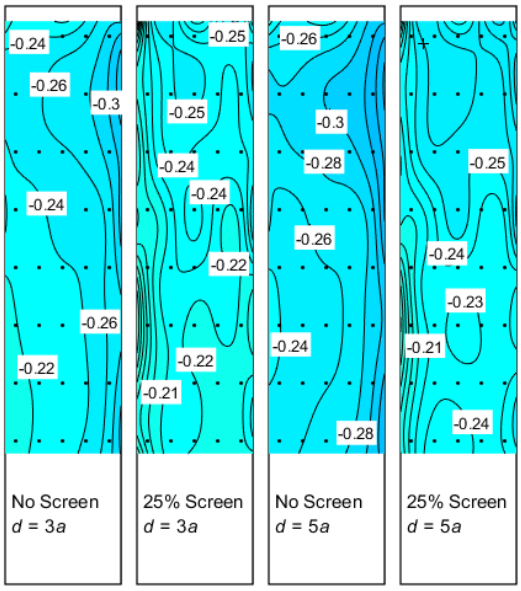

Surface D

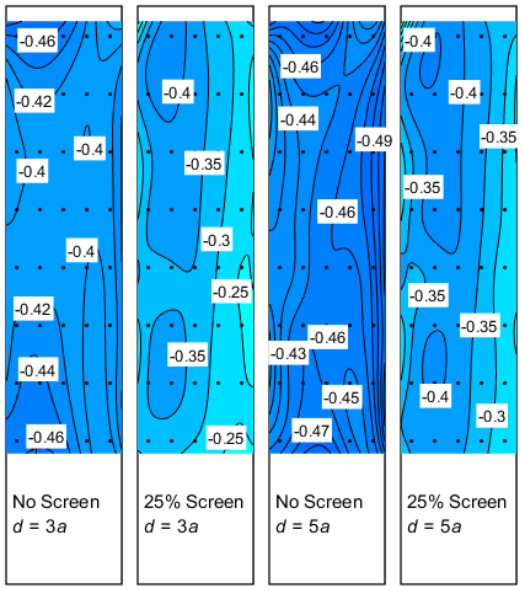

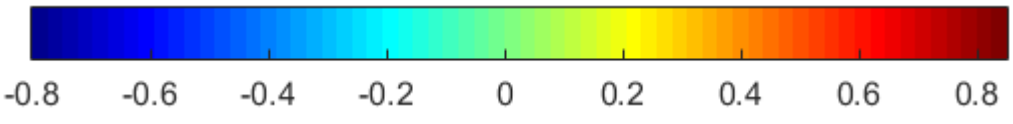

30° Wind incidence angle

Surface A

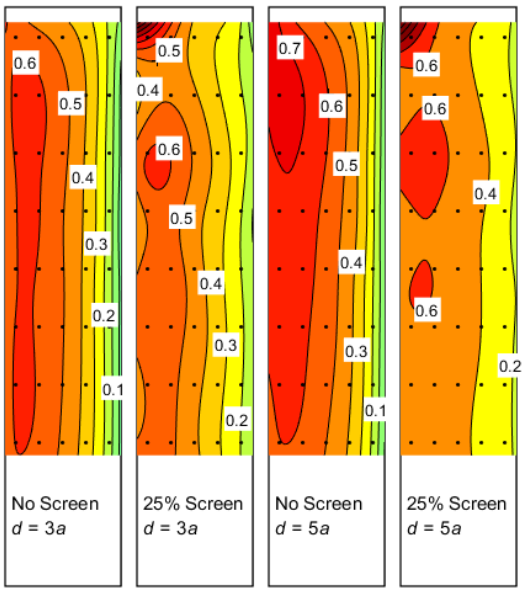

Surface B

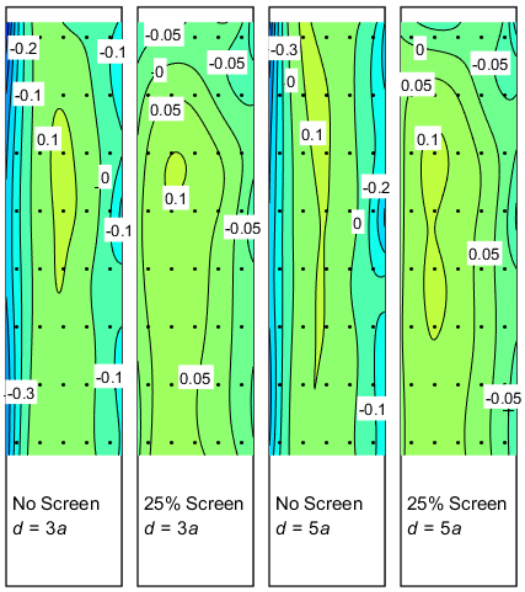

Surface C

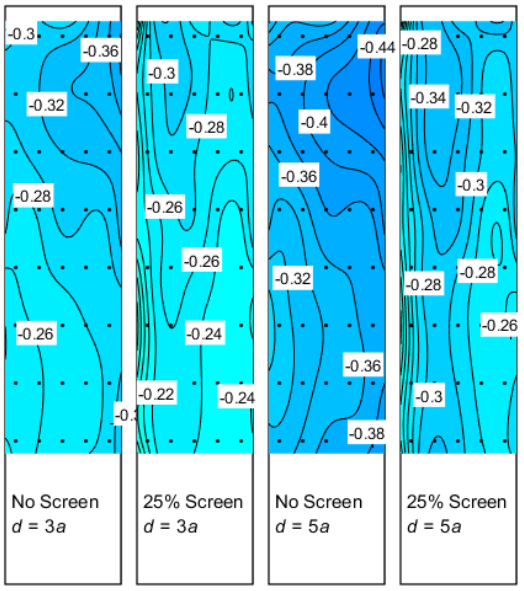

Surface D

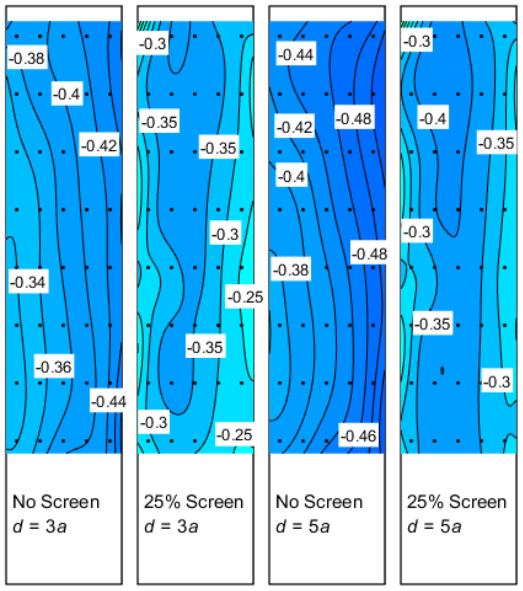

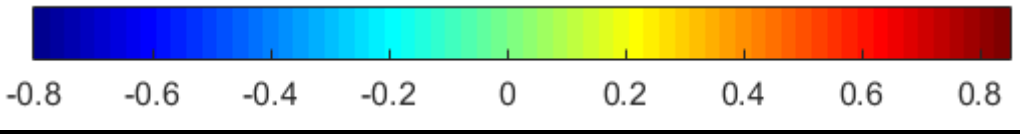

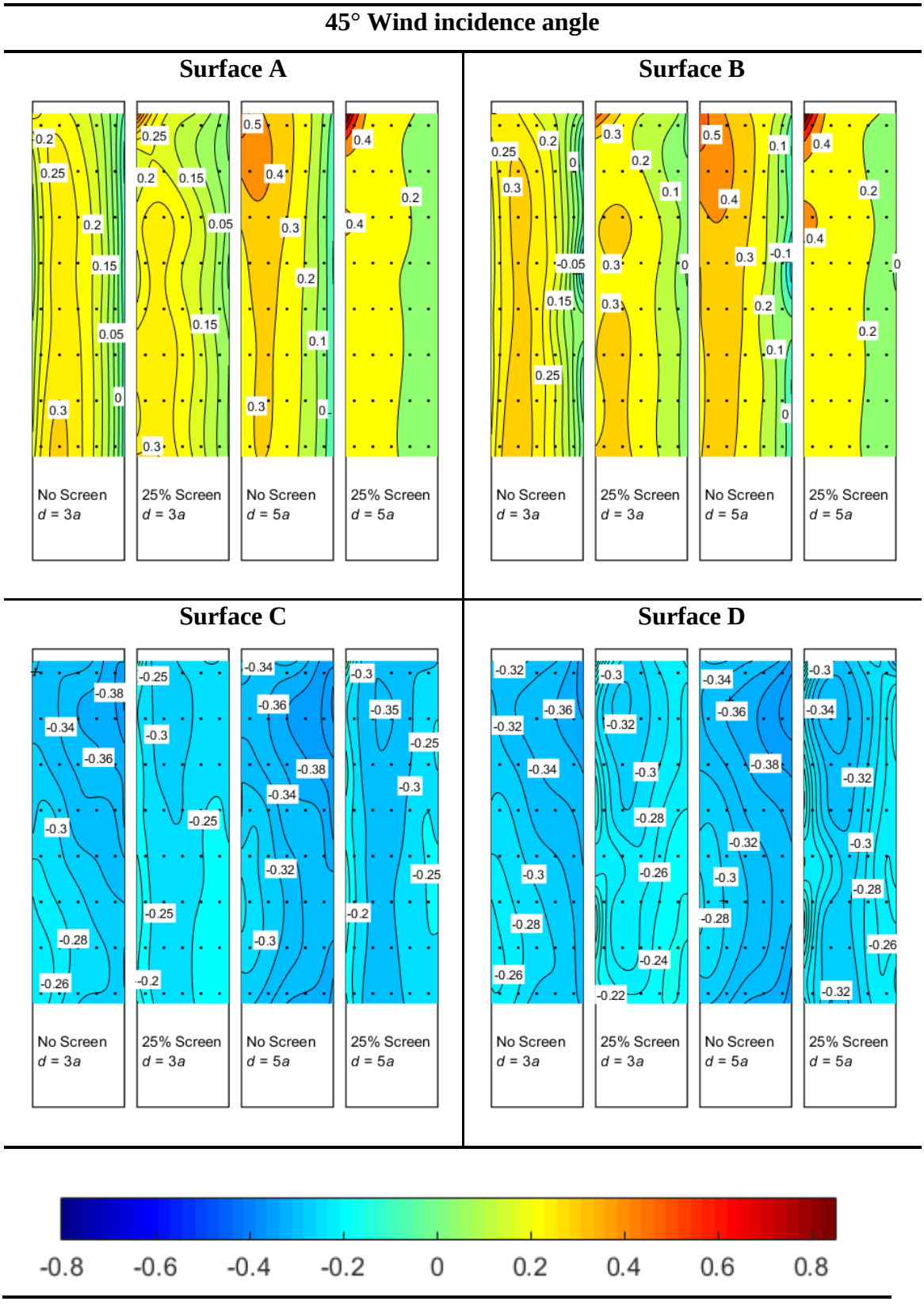

Figure 4.21 Mean pressure coefficient distribution ($\overline{C_p}$) at medium and large spacing ($d = 3a$, $d = 5a$) between model buildings

Distributions of σ of C_p in the second set of experiments are shown in Figure 4.22 and Figure 4.23. Single-skin façade configuration at the small spacing between model buildings is shown in Figure 4.22, while Figure 4.23 shows the results in medium and large spacing configurations with and without the PDSF systems.

By increasing the spacing between dummy model buildings, the area with high σ of C_p also increases in size. For example, on the surface B at 15° wind incidence angle, the area of high σ of C_p is much smaller at the small spacing between model buildings than is the case at the medium spacing density, and even larger at the large spacing between model buildings. The same phenomenon may also be observed at 0°, 30°, and 45° wind incidence angles. On the other hand, the effect of spacing between model buildings on the peak values of σ of C_p is negligible.

The PDSF system in the case of medium and large spacing proved to decrease σ of C_p. For example, on surfaces B and D at 0° and 15° wind incidence angles, that are in the separation zone (wake) where the values of the pressure coefficient standard deviation are high, the PDSF system may cause a decrease in the peak magnitude by $\sim 40\%$. On other surfaces with high values of the σ, the effectiveness of the PDSF system is slightly smaller but is still present.

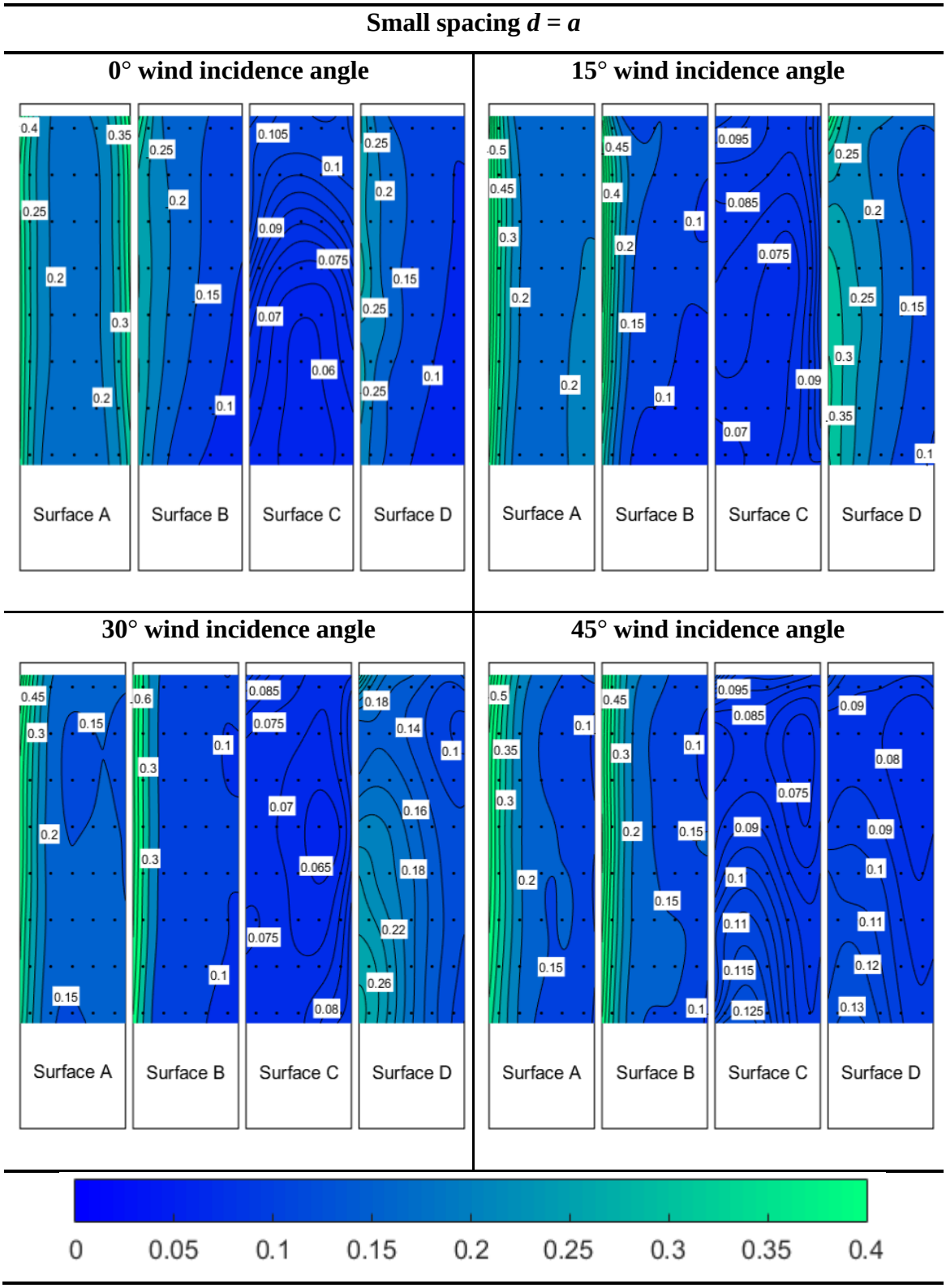

Figure 4.22 Standard deviation distribution of the pressure coefficient at the small spacing between model buildings

0° Wind incidence angle

Surface A

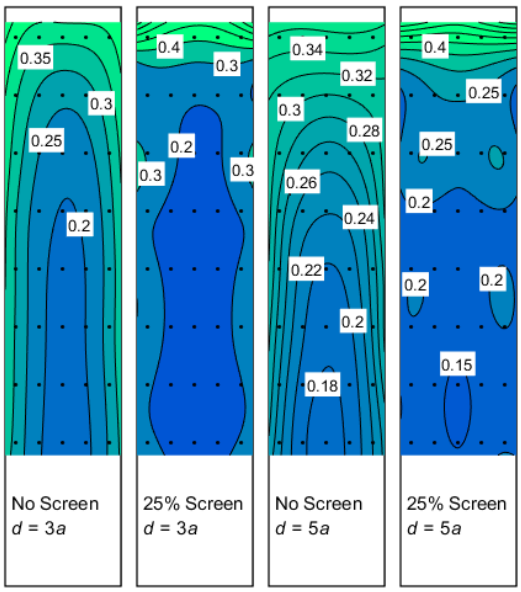

Surface B

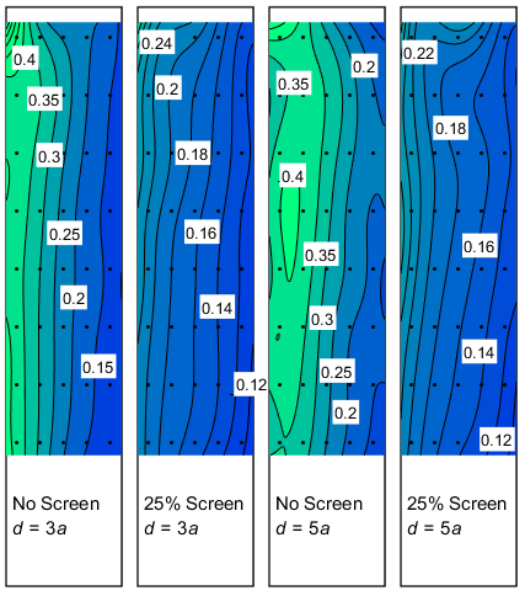

Surface C

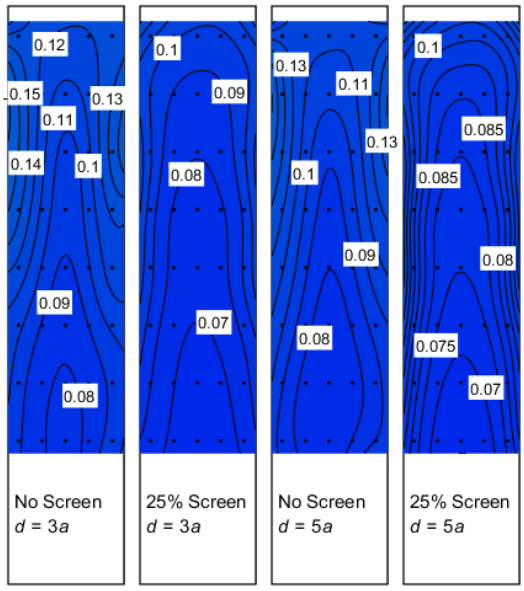

Surface D

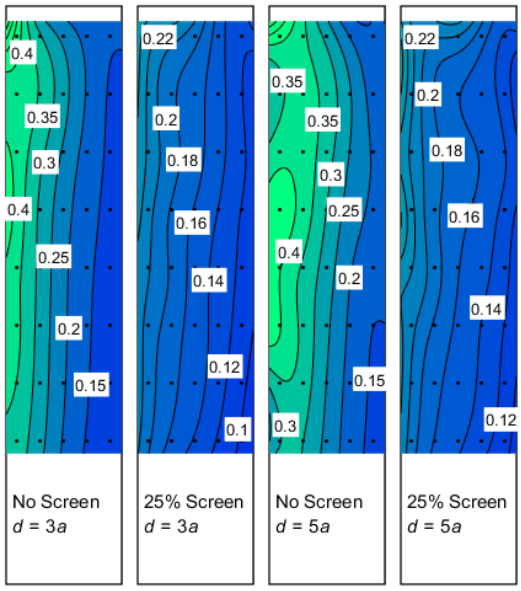

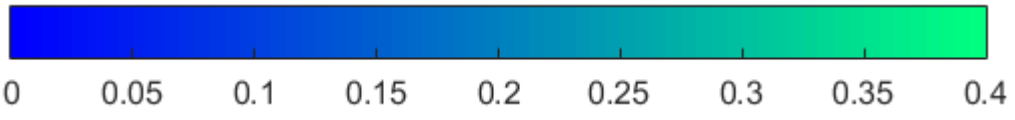

15° Wind incidence angle

Surface A

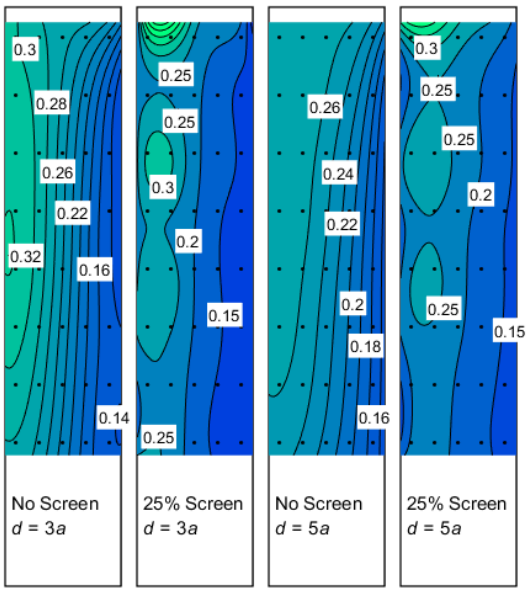

Surface B

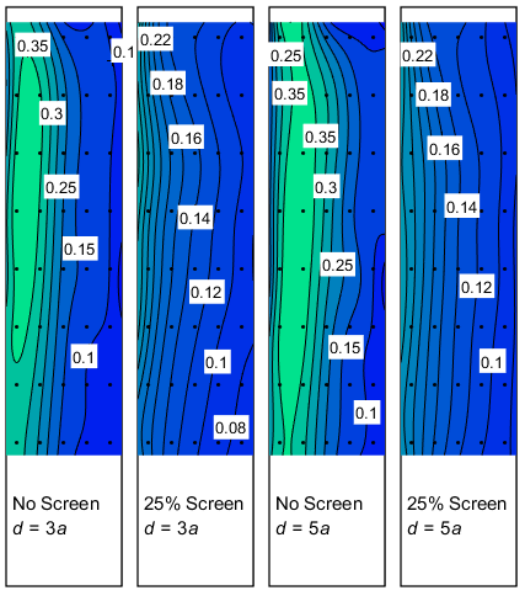

Surface C

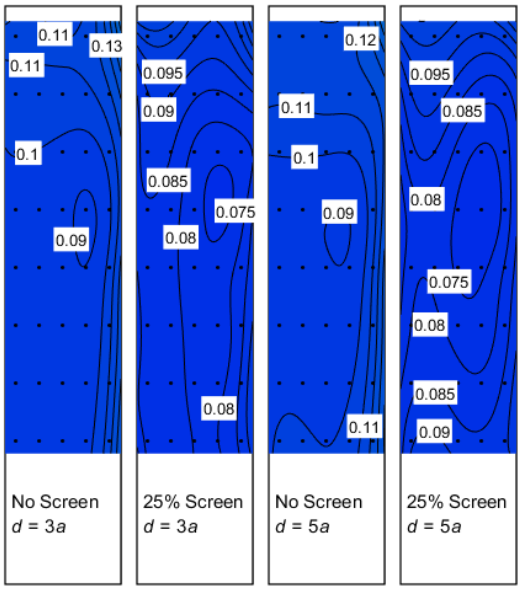

Surface D

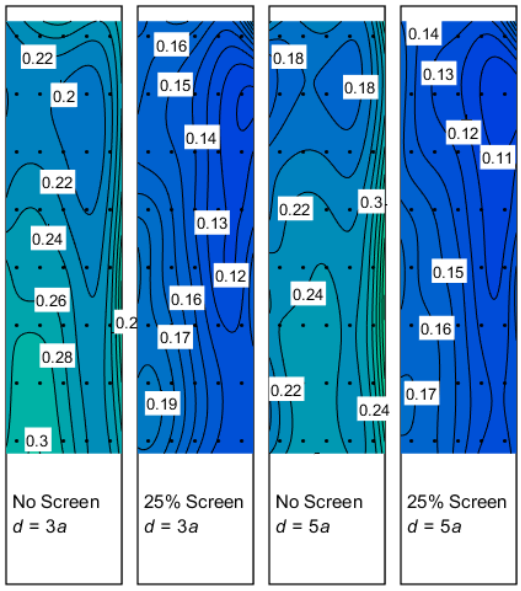

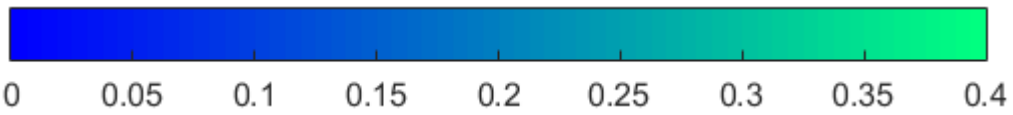

30° Wind incidence angle

Surface A

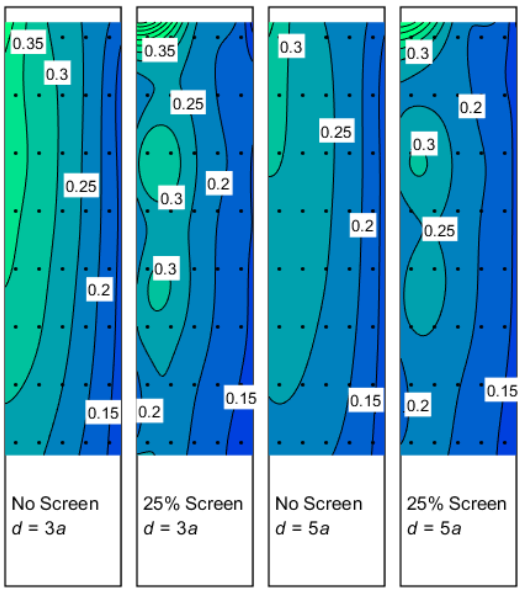

Surface B

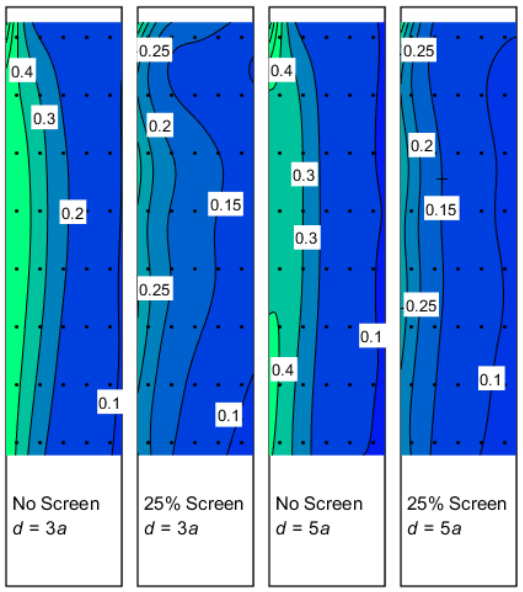

Surface C

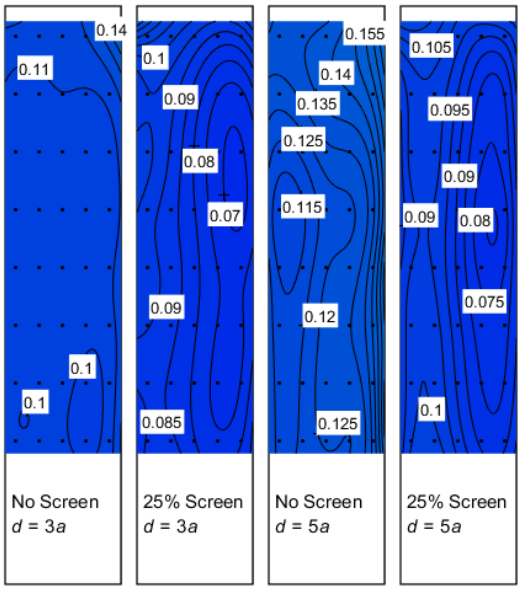

Surface D

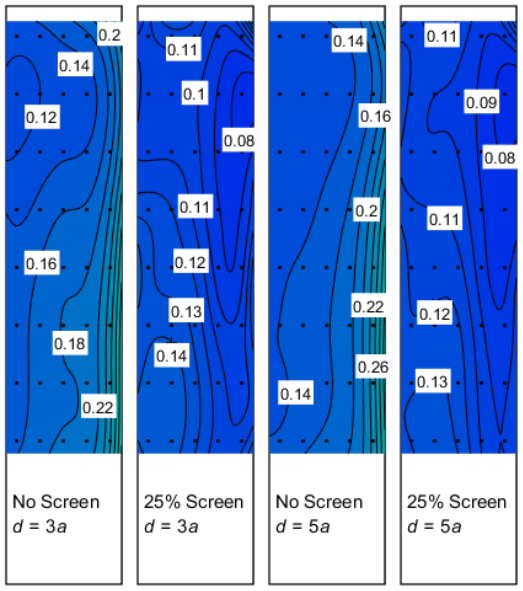

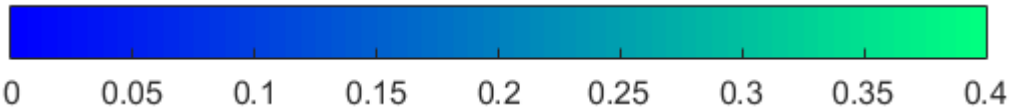

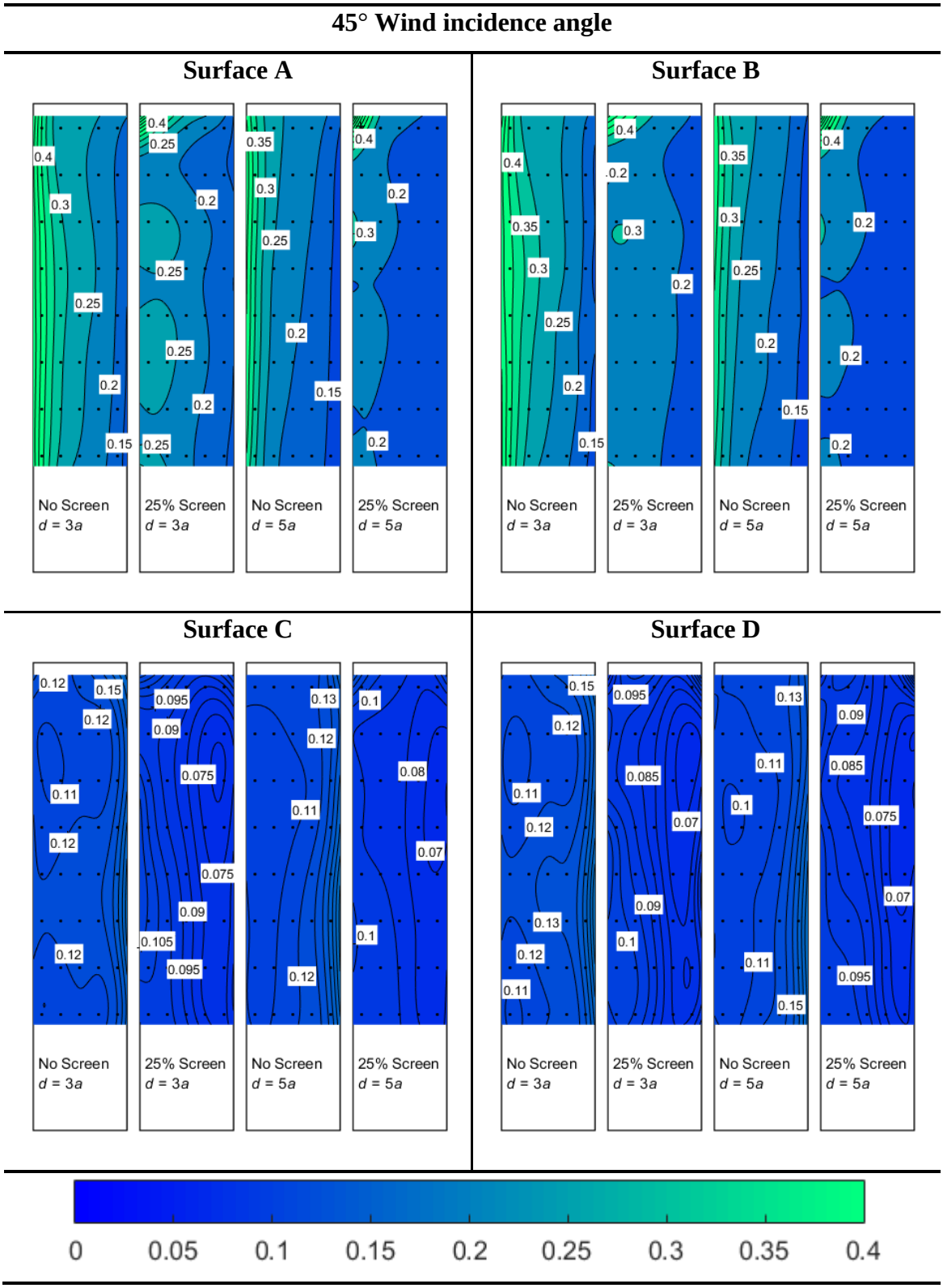

Figure 4.23 Standard deviation distribution of the pressure coefficient at the medium and large spacing ($d = 3a$, $d = 5a$) between model buildings

5 Conclusions

The effects of porous double-skin façade (PDSF) systems on buildings situated in urban environments were studied in a low-speed boundary layer wind tunnel of the Inter-University Research Centre on Building Aerodynamics and Wind Engineering (CRIACIV) at the University of Florence, Italy. The flow conditions in the wind-tunnel test section correspond well to the EN1991-1-4:2005 category III recommendations for the urban ABL. The experimental campaign consisted of two sets of experiments. The first set of experiments observed the effects of various porosities (25%, 50%) on the outer façade of the building model. The building model was situated in the urban environment model ($d = 5a$) that consisted of nine building models aligned in the 3x3 in-line patterns. The second set of experiments analyzed the effects of various spacing densities ($d = a$, $d = 3a$, $d = 5a$) between dummy building models in the urban environment model.

Flow characteristics were determined using Prandtl-Pitot tubes and a hot-wire anemometry system. Aerodynamic loads on the studied building model were measured using a high-frequency force balance (HFFB) FT-Delta SI-165-15 by ATI Industrial Automation. Surface pressure measurements were performed using the PSI-DTC Initium pressure measurement system together with four miniature 32 port DTC scanners. Experiments were performed in the range of 0° to 45° flow incidence angles with the step of 5° for the HFFB measurements and 15° for pressure measurements.

It is generally concluded that the PDSF systems on the studied building model situated in the urban environment model do not affect the across-wind and along-wind moment coefficients for any spacing density of model buildings and the single-skin façade arrangement of the studied building model. At higher spacing between building models, the along-wind moment coefficients increased, while the across-wind moment coefficient remained nearly the same. The PDSF system has a slightly negative effect on the across-wind moment power spectra exhibited in increased peak magnitudes, while the effect on the along-wind power spectra is negligible. There is no clear effect of the spacing between building models on the moment power spectra.

Regarding surface pressure measurements, the DSF system yields a decrease in the mean pressure coefficient peak and a decrease of 10% to 20% in $\overline{C_p}$ on the entire building model surface. As the spacing between building models increases, the studied building model is less sheltered by dummy building models, which causes an increase in the mean pressure coefficient. The standard deviation of the pressure coefficient was lower on the building model equipped with the PDSF system compared to the single-skin model building because the flow between two façades (inner flow) flow was sheltered from the free-stream flow by means of the outer porous façade. The DSF system proved to decrease the peak magnitudes of the standard deviation of the pressure coefficient by up to $\sim 40\%$. Spacing between building models did not affect the peak values of the pressure coefficient standard deviation but increasing the spacing between building models yielded larger areas of high standard deviations of the pressure coefficient.

Literature

[1] Zhu, J., He, G., "Heat transfer coefficients of double skin facade windows", Science and Technology for the Built Environment, 25(9), 1143–1151, 2019.

[2] Kosiński, P., Wójcik, R. and Semen, B. (2019), "Experimental study on the deterioration of thermal insulation performance due to wind washing of the cavity insulation in leaky walls", Science and Technology for the Built Environment, 25(9), 1164-1177, 2019.

[3] Gerhardt, H.J. and Janser, F., "Wind loads on wind permeable facades", Journal of Wind Engineering and Industrial Aerodynamics, 53(1-2), 37-48, 1994.

[4] Hu, G., Song, J., Hassanli, S., Ong, R., Kwok, K.C.S., "The effects of a double-skin façade on the cladding pressure around a tall building", Journal of Wind Engineering and Industrial Aerodynamics, 191, 239-251, 2019.

[5] Kaimal, J.C., Finnigan, J.J., "Atmospheric boundary layer flows: their structure and measurement", Oxford University Press, Oxford, UK, 1994.

[6] Dyrbye, C., Hansen, S.: "Wind loads on structures," John Wiley & Sons, Hoboken, NJ, USA, 1997.

[7] Kozmar, H., "Utjecaj mjerila na strukturu modeliranog atmosferskog graničnog sloja", PhD Thesis, University of Zagreb, Zagreb, Croatia, 2005.

[8] Holmes, J.D. "Wind Loading of Structures", 3rd edition, CRC Press, Taylor & Francis Group, Boca Raton, FL, USA., 2015.

[9] Pernpeintner, A., "Lecture notes from course Aerodynamik der Bauwerke," Lehrstuhl für Fluidmechanik, Fakultät für Maschinenwesen, TU-München, 1998.

[10] Counihan, J., "Adiabatic atmospheric boundary layers: A review and analysis of data from the period 1880-1972", Atmospheric Environment, 9(10), 871-905, 1975.

[11] Garratt, J.R., "The atmospheric boundary layer", Cambridge University Press, Cambridge, UK, 1994.

[12] Kozmar, H., "Characteristics of natural wind simulations in the TUM boundary layer wind tunnel", Theoretical and Applied Climatology, 106(1-2), 95-104, 2011.

[13] Škvorc, P., Kozmar, H., "Aerodynamic characteristics of tall buildings with porous double-skin façades: State of the art and future perspectives", Wind and Structures, 33(3), 233-249, 2021.

[14] Eurocodes standards: https://eurocodes.jrc.ec.europa.eu

[15] Dantec Dynamics, " Probes for Hot-wire Anemometry," 2015.

[16] Jorgensen F. E., "How to measure turbulence with hot-wire anemometers - a practical guide," Dantec Dynamics, 2002.

[17] ATI Industrial Automation: https://www.ati-ia.com/products/ft/ft_models.aspx?id=delta

[18] Aerodynamic Database of High-rise Buildings: http://www.wind.arch.t-kougei.ac.jp/info_center/windpressure/highrise/Homepage/homepageHDF.htm